

Electronic Correlations in Insulators, Metals and Superconductors



Dissertation

im Fach Physik

zur Erlangung der Doktorwürde

der Naturwissenschaften (Dr. rer. nat.)

von der Mathematisch-Naturwissenschaftlichen Fakultät
der Universität Augsburg genehmigt

vorgelegt von

Michael Andreas Sentef

Augsburg, 2010

Erstgutachter: Prof. Dr. Arno Kampf

Zweitgutachter: Prof. Dr. Thilo Kopp

Tag der mündlichen Prüfung: 3. Dezember 2010

Contents

1	Summary	1
2	Introduction	13
2.1	Introductory Remarks	13
2.2	Fermi-Liquid Theory and Quasiparticles	16
3	Models and Methods	19
3.1	The Hubbard Model	19
3.2	Dynamical Mean-Field Theory	22
3.3	Quantum Cluster Theories	28
3.3.1	Cluster DMFT	31
3.3.2	Superconducting States	33
3.3.3	DCA	35
3.3.4	Other Non-Local Generalizations of DMFT	35
3.4	The Mott Transition in Infinite and Two Dimensions	36
3.5	Superconductivity in the 2D Hubbard Model	42
3.5.1	BCS Theory	43
3.5.2	Non-Local Pairing Interactions	47
3.5.3	Superconductivity in the Repulsive Hubbard Model	48
3.6	Continuous-Time Quantum Monte Carlo	51
3.6.1	Hybridization Expansion	53

3.6.2	Generalization to Superconducting States	57
4	Correlations in a Band Insulator	59
4.1	Abstract	60
4.2	Introduction	61
4.3	Model and Methods	63
4.4	Results and Discussion	64
4.4.1	Phase diagram	64
4.4.2	Single-Particle Spectral Function	66
4.4.3	Gap Renormalization and Self-Energy	68
4.4.4	Spin Excitations in the Band Insulator	73
4.5	Conclusion	76
5	Superconductivity in a Non-Fermi Liquid	79
5.1	Abstract	80
5.2	Introduction	80
5.3	Model and Methods	82
5.4	Results and Discussion	85
5.5	Conclusion	95
6	Mott Criticality in a Two-Dimensional Conductor	99
6.1	Abstract	99
6.2	Introduction	99
6.3	Model and Methods	103
6.4	Results and Discussion	106
6.5	Summary	109
7	DC Conductivity of Disordered Graphene	111

7.1	Abstract	111
7.2	Introduction	112
7.3	Model and Method	115
7.4	Results	118
7.5	Summary and Discussion	125
8	Outlook	127
A	Analytic Continuation of QMC Data	133
B	Electrodynamics on the Honeycomb Lattice	139

List of Figures

3.1	DMFT self-consistency cycle	26
3.2	Momentum dependence of self-energy	31
3.3	Cluster division	32
3.4	Bandwidth-controlled Mott transition	37
3.5	Cluster-size scaling for superconductivity	49
4.1	T - U phase diagram	65
4.2	Interaction strength dependence of spectrum	66
4.3	Temperature dependence of spectrum	67
4.4	Self-energy within second-order perturbation theory	71
4.5	Self-energy on Matsubara axis	72
4.6	Spin susceptibility	74
4.7	Spin and charge gaps	75
5.1	U - t - t' Hubbard model in plaquette CDMFT	83
5.2	Phase diagram of 2D U - t - t' Hubbard model in plaquette CDMFT . .	86
5.3	Sequence of phases upon increasing U	88
5.4	Self-energy at $(\pi, 0)$ and quasiparticle weight	90
5.5	Breakdown of Fermi-liquid theory	92
5.6	Non-Fermi liquid to Fermi liquid crossover upon doping	94
5.7	Relation of weak- and strong-coupling phases	96

6.1	Phase diagram of organic conductors	101
6.2	NMR and conductance measurements	102
6.3	U - t - t_{diag} Hubbard model in plaquette CDMFT	104
6.4	Route through continuous Mott transition at fixed temperature . . .	105
6.5	Charge and spin criticality	107
6.6	Probability of plaquette singlet state	109
7.1	Transport in pristine graphene	113
7.2	DC conductivity for the Lloyd model	119
7.3	Density-dependent conductivity and resistivity	121
7.4	Density- and temperature-dependent resistivity	123
7.5	Temperature-dependent conductivity	124
A.1	Analytically continued spectrum	136
B.1	Unit cell of the honeycomb lattice	140
B.2	Dynamical conductivity on the honeycomb lattice	143

Chapter 1

Summary

In this Thesis dynamical mean-field methods in combination with a continuous-time quantum Monte Carlo impurity solver are used to study selected open problems of condensed matter theory. These problems comprise the effect of correlations and their quantification in covalent band insulators, non-local correlation effects and their intriguing consequences in frustrated two-dimensional systems, and a phenomenological approach to investigate temperature-dependent transport in graphene in the presence of disorder. While these problems seem to be quite diverse, at least in part, a recurrent theme in all of these studies is the quasiparticle concept as introduced by Landau in his famous Fermi-liquid theory. Apart from merely summarizing the results it will also be shown how the quasiparticle picture is found to appear in surprising contexts and to be invalidated in situations where it is usually expected to hold.

In Chapter 2 a brief introduction to the physics and theory of correlated electron systems is given and the quasiparticle concept is presented. In Chapter 3 the Hubbard model is introduced as the generic minimal model of correlated electronic systems, and methods to solve the Hubbard model with a focus on dynamical-mean field approximations are described. Especially the Mott metal-insulator transition is discussed and the effects of non-local correlations are illustrated by contrasting the case of infinite dimensions, where correlation effects are purely local, with the case

of two dimensions, where non-local correlations become important. Also instabilities of the two-dimensional Hubbard model towards unconventional superconductivity are discussed. Finally, the continuous-time quantum Monte Carlo impurity solver is briefly introduced.

Correlations in a covalent band insulator are the topic of Chapter 4. A covalent band insulator is a band insulator with partially filled identical local orbitals, a characteristic which is relevant for materials like FeSi or FeSb₂. These materials exhibit non-trivial temperature dependent magnetic and transport properties partly reminiscent of Kondo insulators, and they are also of interest for thermoelectric applications. In our model study we show that a discontinuous transition from a band insulator to a Mott insulator takes place upon increasing the local Coulomb repulsion between electrons at low temperature. Moreover unexpected behavior is induced by electronic correlations. The charge gap shrinks with increasing interaction strength, and the charge and spin gaps deviate from each other in the correlated band insulator. In the Mott insulator the more conventional behavior is observed, with a vanishing spin gap and a charge gap which increases with increasing Coulomb repulsion. The shrinking of the charge gap in the correlated band insulator is traced to a gain of correlation energy by adding a single electron to the half-filled system. This consequently leads to a stronger energetic lowering of the single-electron excited state compared to the lowering of the ground state, hence a gap reduction. Interestingly this effect explains why band structure calculations for FeSi and FeSb₂ overestimate the charge gap by underestimating correlations, while for Mott insulators the charge gap is usually underestimated. Surprisingly, further insight into the problem is provided by an analogy with Fermi-liquid theory: the charge gap renormalization is related to a renormalization factor extracted from the linear slope of the real part of the self-energy, similar to the effective mass renormalization known, for example, from heavy-fermion systems. Therefore correlations in a band insulator are quantified by a relation borrowed from

the quasiparticle concept in Fermi-liquid theory, which is quite a remarkable fact.

In Chapter 5 a cluster generalization of dynamical-mean field theory to a plaquette is used to investigate the two-dimensional Hubbard model on the square lattice with a next-nearest neighbor hopping. Here the quasiparticle picture is found to break down already at relatively weak coupling and half-filling in the antinodal directions in momentum space. Moreover a *d*-wave superconducting phase emerges from this non-Fermi liquid metallic phase upon cooling. Hence Cooper pairs are formed in a state in which the quasiparticle lifetime in the respective momentum space region is already very small and non-Fermi liquid behavior is observed. A crossover from the weak-coupling non-Fermi liquid to a more conventional Fermi liquid metal is obtained upon doping the system. It is a fascinating open problem whether the non-Fermi liquid and superconducting phases at weak coupling and half-filling are related to the respective phases known to exist at strong coupling and finite doping. These questions lie at the heart of understanding the two-dimensional Hubbard model in the presence of a next-nearest neighbor hopping, which is also relevant for the superconducting cuprates. Furthermore it would be intriguing to study the theoretically observed weak-coupling phases in experiments. We mention here recent progress in the synthesis and investigation of new materials from the cuprate family, which for example allowed to study the difference between hole and electron doping and to provide insight into the consequences of weak and strong coupling magnetic ordering mechanisms in the undoped mother compounds.

A direct experimental motivation gave rise to the investigation presented in Chapter 6. In quasi two-dimensional organic charge transfer salts the bandwidth-controlled Mott metal-insulator transition can be studied by the application of hydrostatic pressure. In a series of conductance and NMR measurements under pressure it was found that the critical behavior at the continuous finite-temperature Mott transition in κ -(ET)₂Cu[N(CN)₂]Cl is not compatible with the conventional Ising universality class,

which is known to apply to the three-dimensional Mott transition in $(V_{1-x}Cr_x)_2O_3$. A possible theoretical explanation of the deviation from Ising universality was guided by the insight that observables (like the conductance) may show different critical behavior than the order parameter of the transition, which is in fact not even precisely known for the Mott transition, and that Ising universality with modified critical exponents for the conductance therefore still applies. However, it was also proposed in a different theoretical approach that the real cause for unconventional Mott criticality in two dimensions lies in the fundamental importance of non-local correlations and the partial vanishing of the Fermi surface in the correlated metal. In essence, the idea behind this proposal is that the Mott transition in high dimensions may be described by a single number, namely the isotropic quasiparticle renormalization factor, which vanishes at the continuous transition and thus acts like a scalar (Ising-like) order parameter. This consequently leads to Ising criticality in high dimensions, and Ising universality is therefore also observed in three-dimensional systems if the quasiparticle picture holds in the correlated metal. In two dimensions, however, non-local correlation effects render the isotropic quasiparticle picture invalid and momentum-space differentiation with a partial depletion of the Fermi surface occurs, which is why Ising universality does not apply according to these arguments. Therefore the precise extent of validity of the quasiparticle concept and deviations from conventional Fermi-liquid physics play an important role also for this problem. While not elaborating on these fundamental issues, we still contribute to the discussion by modeling the experimental situation and following critical observables for the charge and spin degrees of freedom across the continuous transition. Remarkably, we find considerable agreement regarding the critical scaling laws with experimental data as well as theoretical predictions despite certain approximations involved. It is important to note here that the cluster dynamical-mean field method on the plaquette, which is used to calculate the observables, indeed captures a certain amount of non-local correlations. Hence

the consistency of our results with experiments suggests the importance of non-local correlations for unconventional Mott criticality in two dimensions.

The manufacture of single sheets of two-dimensional carbon, known as graphene, has recently attracted a lot of attention. A clean system of tight-binding electrons on a half-filled honeycomb lattice is a non-ideal conductor, which means that it has a finite dc conductivity at zero temperature even in the absence of impurities. This peculiar behavior is directly related to the linear quasiparticle dispersion at low energies in combination with the two-dimensionality, i.e., to the physics of massless two-dimensional Dirac fermions. In Chapter 7 we contribute to the investigation of the remarkable electronic properties of graphene by calculating its dc conductivity in the presence of local disorder. While disorder effects are particularly strong in non-suspended graphene on insulating substrates, recently fabricated suspended graphene samples show ultrahigh charge carrier mobilities. However, microscopic corrugations known as ripples, which are thermally induced intrinsic instabilities in two-dimensional sheets, and also impurity atoms or molecules adhering to the sheet still make the system “imperfect” with respect to a simple tight-binding model on a honeycomb lattice. In our work we use a phenomenological model for disorder by introducing a local random disorder distribution, which is treated in a coherent-potential approximation, the analogue to dynamical mean-field theory for disordered systems. By allowing the disorder strength to depend on temperature explicitly, our approach describes several features of the temperature dependent dc conductivity observed in experiments. In particular, a finite minimum conductivity at the charge neutrality point is found, which increases with temperature similar to the conductivity in a semiconductor. To be precise, the behavior is not entirely semiconducting, however, since the system has a finite minimum conductivity even at zero temperature. Away from the charge neutrality point, the temperature dependence changes, and at sufficiently large densities the conductivity becomes metallic. We show that a resis-

tivity which increases linearly with temperature and has a slope which decreases with increasing density, as measured for suspended graphene, is reproduced by assuming a temperature-dependent disorder strength. The corresponding scattering rate has a finite zero-temperature offset and increases linearly with temperature. This finding suggests the importance of at least two sources of scattering: a temperature-independent contribution, possibly related to adsorbed impurities, and a contribution from thermal excitations which may be related to ripples.

Zusammenfassung

In der vorliegenden Arbeit werden dynamische Molekularfeld-Näherungen auf ausgewählte offene Probleme der Theorie der kondensierten Materie angewandt. Zu diesen Problemen gehören Korrelationseffekte und deren Quantifizierung in kovalenten Band-Isolatoren, nichtlokale Korrelationen und deren Auswirkungen in frustrierten zweidimensionalen Systemen sowie ein phänomenologischer Zugang zu temperaturabhängigem Transport in Graphen mit Unordnung. Diese Probleme scheinen auf den ersten Blick sehr unterschiedlich zu sein. Neben der methodischen Verwandtschaft in deren Behandlung findet sich jedoch ein weiterer roter Faden, nämlich das Quasiteilchen-Konzept, das von Landau im Rahmen seiner Fermiflüssigkeitstheorie eingeführt wurde. In dieser Zusammenfassung sollen die vorgestellten Probleme auch unter dem Aspekt ihres Bezugs zum Konzept der Quasiteilchen betrachtet werden. Insbesondere soll gezeigt werden, wie das Quasiteilchen-Konzept in überraschenden Zusammenhängen auftaucht und dann wiederum in Situationen ungültig wird, in denen man es nicht unbedingt erwartet.

In Kapitel 2 wird die Physik korrelierter Elektronen vorgestellt und das Quasiteilchen-Konzept präsentiert. Kapitel 3 enthält eine Einführung in das Hubbard-Modell als ein minimales Modell für die Physik korrelierter Elektronen. Ferner wird die dynamische Molekularfeld-Theorie vorgestellt, die im Grenzfall unendlicher Dimensionalität eine exakte Lösung des Hubbard-Modells liefert. Der Phasenübergang von einem Metall zu einem Mott-Isolator wird diskutiert, und anhand dessen unterschiedlicher

Charakteristika in unendlichen und in zwei Dimensionen wird die Bedeutung nichtlokaler elektronischer Korrelationen in niedrigdimensionalen Systemen illustriert. Anschließend werden Instabilitäten des zweidimensionalen Hubbard-Modells gegenüber unkonventioneller Supraleitung besprochen. Schließlich wird kurz gezeigt, wie man eine numerische Lösung von Quanten-Störstellen-Problemen, die im Rahmen von dynamischen Molekularfeld-Näherungen auftauchen, mit einem Quanten-Monte-Carlo-Algorithmus in kontinuierlicher imaginärer Zeit erhält.

Korrelationen in einem Band-Isolator sind das Thema von Kapitel 4. Ein kovalenter Band-Isolator ist definiert als Band-Isolator mit teilweise gefüllten identischen lokalen Orbitalen. Solche Charakteristika tauchen zum Beispiel in Materialien wie FeSi oder FeSb₂ auf, die ähnlich wie Kondo-Isolatoren nichttriviale temperaturabhängige magnetische und Transport-Eigenschaften aufweisen und für thermoelektrische Anwendungen interessant sind. In unserer Modell-Studie zeigen wir, dass ein diskontinuierlicher Übergang zwischen einem Band-Isolator und einem Mott-Isolator durch die lokale Coulomb-Abstoßung zwischen Elektronen induziert wird. Die Energielücke für Ladungsanregungen wird ungewöhnlicherweise durch Korrelationen verkleinert. Zudem sind die Ladungs- und Spinanregungslücken im korrelierten Band-Isolator verschieden. Das Schrumpfen der Lücke im korrelierten Band-Isolator lässt sich darauf zurückführen, dass das System durch Einteilchen-Anregungen Korrelationsenergie gewinnt, dadurch der angeregte Zustand eine größere störungstheoretische Energieabsenkung erfährt als der Grundzustand und sich somit die Anregungslücke im Vergleich zum nichtwechselwirkenden System verkleinert. Interessanterweise werden ähnliche Effekte in der Tat in FeSi und FeSb₂ beobachtet. Dort überschätzen Bandstruktur-Rechnungen die Energielücke, wohingegen sie in Mott-Isolatoren die Lücke typischerweise unterschätzen. Dies lässt sich so interpretieren, dass Bandstruktur-Rechnungen tendenziell Korrelationseffekte unterschätzen. Wenn nun, wie im Fall des korrelierten kovalenten Isolators, Korrelationen die Lücke schrumpfen lassen,

wird die Lücke folglich überschätzt, wenn Korrelationseffekte unterschätzt werden. Im korrelierten Band-Isolator taucht auch überraschenderweise ein Konzept der Fermiflüssigkeitstheorie auf. Man kann nämlich zeigen, dass die Renormierung der Lücke sich durch einen Renormierungsfaktor quantifizieren lässt, der formal dem Quasiteilchen-Gewicht aus der Fermiflüssigkeitstheorie entspricht. Die Verkleinerung der Energielücke durch Korrelationen entspricht unter diesem Aspekt der Erhöhung der effektiven Bandmasse, die man beispielsweise aus Schwer-Fermionen-Systemen kennt — ein durchaus bemerkenswerter Zusammenhang.

Die Kapitel 5 und 6 befassen sich mit der Anwendung einer nicht-lokalen Erweiterung der dynamischen Molekularfeld-Theorie auf eine Plaketten-Geometrie für zweidimensionale Modelle (Plaketten-Näherung). In Kapitel 5 wird das zweidimensionale Hubbard-Modell mit einem Nächst-Nachbar-Hüpfen in der Plaketten-Näherung gelöst. Das Quasiteilchen-Bild bricht für dieses System bei halber Bandfüllung schon bei schwacher Wechselwirkung zusammen, und zwar in der Nähe des $(\pi, 0)$ -Punkts. Zudem entsteht aus diesem ungewöhnlichen Metall bei Abkühlung ein unkonventioneller Supraleiter mit d -Wellen-Symmetrie. Das bedeutet, dass die Cooperpaare in einem Zustand gebildet werden, in dem es in gewissen Impulsbereichen gar keine wohldefinierten Quasiteilchen gibt. Durch Dotierung wird der Nicht-Fermiflüssigkeitszustand wieder in eine Fermiflüssigkeit überführt. Die vorliegenden Ergebnisse bei halber Füllung und schwacher Kopplung erinnern in verschiedener Hinsicht an bekannte Resultate bei starker Kopplung und endlicher Dotierung. Beim Dotieren eines Mott-Isolators gibt es nämlich auch eine Tendenz zu d -Wellen-Supraleitung und eine Nicht-Fermiflüssigkeits-Phase mit einem sogenannten Pseudogap und einem Zusammenbruch des Quasiteilchen-Bilds entlang gewisser Impulsrichtungen. Wenngleich diese Stark-Kopplungs-Phasen schon bei höheren Temperaturen und in größeren Bereichen des Phasenraums auftreten, ist ein möglicher Zusammenhang mit den entsprechenden Phasen bei schwacher Kopplung sehr interessant und zum Beispiel auch für die

Kuprat-Supraleiter von Relevanz.

Experimentelle Befunde gaben Anlass zu der Studie in Kapitel 6. In quasi-zweidimensionalen organischen Ladungstransfersalzen wie κ -(ET)₂Cu[N(CN)₂]Cl (kurz κ -Cl) kann der bandbreiten-kontrollierte Mott-Übergang durch Anwendung von hydrostatischem Druck untersucht werden. In einer Reihe von Messungen der elektrischen Leitfähigkeit und der Spin-Gitter-Relaxationsrate, gemessen mit Kernspinresonanz (NMR), wurde gezeigt, dass das Verhalten von Ladungs- und Spin-Freiheitsgraden am kontinuierlichen Mott-Übergang bei der kritischen Temperatur in κ -Cl nicht mit dem kritischen Verhalten gemäß der zweidimensionalen Ising-Universalitätsklasse kompatibel ist. Diese Beobachtung steht im Kontrast zum dreidimensionalen Mott-Übergang zum Beispiel in (V_{1-x}Cr_x)₂O₃, wo man Ising-Universalität beobachtet. Das ungewöhnliche Verhalten in κ -Cl liegt möglicherweise darin begründet, dass Observablen wie die Leitfähigkeit ein vom Ordnungsparameter abweichendes kritisches Verhalten zeigen können und demnach die Ising-Universalitätsklasse dennoch gültig ist. Ein anderer theoretischer Ansatz erklärt das ungewöhnliche kritische Verhalten jedoch dadurch, dass der Ordnungsparameter für den Mott-Übergang in zwei Dimensionen nicht Ising-artig ist. Demnach ist der dreidimensionale Mott-Übergang durch eine einzige Zahl (einen Skalar) charakterisiert, nämlich das isotrope Quasiteilchen-Gewicht, das am kontinuierlichen Metall-Isolator-Übergang verschwindet. Wegen des so definierten skalaren Ordnungsparameters ist der dreidimensionale Mott-Übergang Ising-artig — im Gegensatz zum zweidimensionalen Fall, in dem nichtlokale Korrelationen das Quasiteilchen-Konzept impulsabhängig zusammenbrechen lassen und folglich der Mott-Übergang nicht mehr Ising-artig ist. Diese Argumentation unterstreicht die Bedeutung nichtlokaler Korrelationseffekte und insbesondere des präzisen Gültigkeitsbereichs des Quasiteilchen-Konzepts in niedrigdimensionalen Systemen. In unserer Studie gehen wir nicht im Detail auf diese zweifellos faszinierenden tieferliegenden Fragen ein, sondern beschränken uns vielmehr auf eine numerische Berech-

nung des Skalen-Verhaltens von Ladungs- und Spin-Freiheitsgraden in einem effektiven zweidimensionalen Hubbard-Modell für κ -Cl im Rahmen der Plaketten-Näherung. Trotz notwendiger Näherungen finden wir eine erstaunlich gute Übereinstimmung mit den experimentellen Daten wie auch mit den vorhandenen theoretischen Ansätzen. Da die Plaketten-Näherung in einem gewissen Maß auch nichtlokale Korrelationen berücksichtigt, legt die gute Übereinstimmung unserer Ergebnisse mit den Experimenten die Bedeutung nichtlokaler Korrelationen für das unkonventionelle kritische Verhalten am zweidimensionalen Mott-Übergang nahe.

Die Herstellung zweidimensionaler Schichten aus Graphit, die unter dem Namen Graphen bekannt sind, hat in letzter Zeit große Aufmerksamkeit erregt. Ein reines System von Tight-Binding-Elektronen auf einem Honigwabengitter ist ein nicht-idealer Leiter ohne Störstellen. Das bedeutet, dass das System eine endliche elektrische Gleichstrom-Leitfähigkeit am absoluten Temperatur-Nullpunkt besitzt. Dieses Verhalten hängt mit der linearen Dispersionsrelation bei niedrigen Energien in Kombination mit der Zweidimensionalität zusammen, also mit der Physik masseloser¹ zweidimensionaler Dirac-Fermionen. In Kapitel 7 wird eine phänomenologische Theorie zur Berechnung der elektrischen Leitfähigkeit von Graphen mit lokaler Unordnung vorgestellt. Während nicht-freischwebendes Graphen starke Unordnungseffekte zeigt, weisen freischwebende Graphen-Proben sehr hohe Ladungsträgermobilitäten auf, was auf einen verringerten Einfluss von Unordnung hindeutet. Bei freischwebendem Graphen treten jedoch sogenannte Ripples auf, also thermisch angeregte intrinsische Verzerrungen der zweidimensionalen Schicht. Zudem können sich auf der Schicht Störatome oder -moleküle befinden, die das System verunreinigen und im

¹Ich erlaube mir, an dieser Stelle aus der amerikanischen Comedy-Serie *The Big Bang Theory* zu zitieren: “Good lord! The interference pattern in the fracture, the motion of the wave through the molecular structure ... I’ve been looking at it all wrong! I can’t consider the electrons as particles. They move through the graphene as a wave! It’s a wave! The moment to applaud would be now! ... Troglodytes!” (Dr Sheldon Cooper, Staffel 3, Folge 14: *The Einstein Approximation*)

Vergleich zum perfekten Honigwaben-Gittermodell imperfekt machen. Wir beschreiben Unordnungseffekte durch ein phänomenologisches Modell zufällig verteilter Störstellen, das mit einer Molekularfeld-Methode näherungsweise gelöst wird. Mit einer Unordnungsstärke, die explizit von der Temperatur abhängt, beschreiben wir mit diesem Zugang mehrere beobachtete Transport-Effekte in freischwebendem Graphen. Insbesondere berechnen wir die Temperatur-Abhängigkeit der sogenannten minimalen Leitfähigkeit im ungeladenen System und verfolgen das Transportverhalten beim Anlegen einer Gate-Spannung, also bei endlichen Ladungsdichten. Dabei beobachten wir in Übereinstimmung mit dem Experiment einen Übergang von halbleiterartigem Verhalten bei kleinen Dichten zu metallischem Verhalten bei großen Dichten. Das lineare Verhalten des temperaturabhängigen Widerstand bei großen Dichten lässt sich konsistent mit einer temperaturabhängigen Unordnungsstärke modellieren, die aus einem konstanten Beitrag sowie einem linear mit der Temperatur wachsenden Beitrag besteht. Dieses Ergebnis legt die Bedeutung mindestens zweier Quellen für Streuung in freischwebendem Graphen nahe, von denen eine temperaturunabhängig ist und die andere mit thermischen Anregungen verknüpft ist.

Chapter 2

Introduction

2.1 Introductory Remarks

The understanding of the physical properties of electrons in a solid involves a highly complex quantum-mechanical many-body problem. Even if the ionic lattice is treated as a static potential for the electrons in the Born-Oppenheimer approximation, the Coulomb repulsion between the electrons renders exact solutions of the problem impossible in most cases. Nevertheless it is often a good approximation to reduce the many-electron problem to an effective single-particle description, as in density functional theory [1], which has been successfully applied to rather weakly interacting systems with conduction bands derived from s or p electrons. However, the single-particle picture fails when the Coulomb repulsion becomes too strong, which is typically the case in systems with open d or f shells.

A periodic lattice with an even number of electrons per unit cell is a band insulator because its energy bands are either filled or empty. In a class of materials called Mott insulators, in contrast, the Coulomb repulsion between electrons renders the system insulating even though the bands are partially filled. The single-band Hubbard model [2, 3, 4] (see Sec. 3.1) is a generic minimal model which contains the limiting cases of (i) non-interacting, delocalized electrons in a metallic band and (ii) localized electrons

in a Mott insulator.¹ Its main parameters are the bare bandwidth W , the strength of the local Coulomb repulsion U , the band filling n and the lattice dimensionality d . The phase transition which occurs in between the two limits (i) and (ii) is known as the Mott metal-insulator transition (MIT) [5]. The bandwidth-controlled MIT at zero temperature and half-filling occurs when the ratio U/W exceeds a critical value, which depends on the dimensionality and lattice structure of the system.

An important step forward in the understanding of the Mott transition was made when it was realized that the Hubbard model can be solved numerically exactly in the limit of infinite dimensions or, equivalently, infinite lattice coordination number [6]. In this limit the electronic self-energy becomes local, and the full lattice problem can be mapped to an auxiliary impurity problem [7] with a surrounding bath which has to be determined self-consistently. In the framework of the dynamical mean-field theory (DMFT, see Sec. 3.2) this mapping can also be used as a controlled approximation for treating electronic correlation effects in a solid [8]. In DMFT the local dynamical correlations are accounted for exactly, while non-local dynamical correlations are neglected. In conjunction with the local-density approximation (LDA) to the density functional theory, DMFT has thus become a very successful tool for the ab-initio study of strongly correlated electron systems, an approach which is commonly abbreviated as LDA+DMFT [9, 10].

Naturally, as it is formulated for the limit of infinite dimensions, the application of DMFT to model systems becomes problematic if the dimensionality is low, e.g., in two dimensions. However, there are fascinating examples of classes of effectively two-dimensional systems which one would like to understand and where correlations are strong, like the high-temperature cuprate superconductors or the organic charge transfer salts. In the latter, for example, the bandwidth-controlled MIT can be probed

¹The Hubbard model can indeed be formulated for any kind of band structure involving also band insulators, see Chapter 4.

by applying hydrostatic pressure. Moreover, in both of the mentioned material families unconventional superconducting phases are observed.

In fact, it is quite obvious why DMFT, in its single-site version, is insufficient to describe the physics of these two-dimensional systems. The description of unconventional superconducting pairing, e.g., d -wave pairing, in a model with repulsive bare interactions requires the inclusion of non-local dynamical pair field amplitudes, hence the inclusion of non-local dynamical correlations. Moreover, in two-dimensional correlated systems the phenomenon of momentum-space differentiation occurs. This means that even in the metallic state parts of the Fermi surface may vanish while other parts still survive, the proper description of which demands to take into account the momentum dependence (i.e., the non-locality) of the self-energy.

Several generalizations of DMFT have been proposed to deal with situations in which non-local correlations become important. Among them are quantum cluster theories (see Sec. 3.3), such as the cellular DMFT (CDMFT), the dynamical cluster approximation (DCA) or the variational cluster approximation (VCA), the dynamical vertex approximation (D Γ A) and the dual-fermion (DF) method. In contrast to DMFT, all of these methods allow for a momentum dependence of the self-energy. By these means, it became possible to study the Mott MIT also in the two-dimensional Hubbard model, where certain characteristics of the transition are different from the infinite-dimensional limit (see Sec. 3.4).

Both in DMFT and its cluster generalizations the lattice problem is mapped to an effective (single- or cluster-) impurity problem. The solution of the impurity problem requires the application of a so-called impurity solver. One possible choice is the continuous-time quantum Monte Carlo (CTQMC) method. Its flavor used throughout this work, the hybridization expansion, is based on the expansion of the effective impurity action in the hybridization between impurity and bath sites. A derivation of the basic formulas and a brief description of the underlying algorithm

is presented in Sec. 3.6.

2.2 Fermi-Liquid Theory and Quasiparticles

One of the most important advances in the theoretical understanding of condensed matter was the formulation of Landau's Fermi-liquid theory [11,12]. In essence, Fermi-liquid theory is a phenomenological theory which applies to normal Fermi systems, i.e., systems which can be adiabatically connected to the Fermi gas. Fermi-liquid theory was successfully applied to normal ^3He [13] and provided a basis for the understanding of heavy-fermion systems [14] and correlated metals in general.

By introducing the concept of quasiparticles, Fermi-liquid theory treats a system of interacting fermions (e.g., electrons in a solid) as a liquid of quasiparticles which also obey Fermi-Dirac statistics. The quasiparticles are characterized by an effective mass m^* which is larger than the bare fermionic mass m due to the interactions between the bare fermions. Landau's theory explains why thermodynamic properties (temperature dependence of the specific heat, spin susceptibility etc.) of interacting Fermi systems correspond to the properties of the free Fermi gas, but with renormalized parameters.

If more than one quasiparticle is excited there are also weak residual interactions between quasiparticles. However, scattering processes are sufficiently suppressed by Pauli's exclusion principle, at least for three-dimensional isotropic systems. Therefore the phase space volume available for scattering processes close to the Fermi surface is severely reduced and the residual interactions between quasiparticles are indeed weak. In fact, in a Fermi liquid the quasiparticles have an infinite lifetime at the Fermi surface and at zero temperature. Thus Fermi-liquid theory consistently guarantees the existence of well-behaved quasiparticles *provided* that the initial mapping between the Fermi gas and the Fermi liquid is possible. In other words, the gas-to-liquid mapping can be viewed as the main assumption of Fermi-liquid theory.

A relation of the phenomenological quasiparticle concept to the microscopically determined single-particle self-energy is formulated in Sec. 3.4. As mentioned above, the consistency of Fermi-liquid theory is based on the assumption of reduced scattering phase space. This assumption can be shown to hold for three-dimensional isotropic systems [15]. For two-dimensional systems, however, the phase space argument does not necessarily hold. Indeed the existence of van-Hove singularities in the density of states due to saddle points in the bare energy dispersion may further enhance low-energy scattering phase space and provide a basis for the breakdown of Fermi-liquid theory in the presence of electronic correlations. An example of non-Fermi liquid behavior in a two-dimensional system even for weak electronic interactions is shown in Chapter 5.

Chapter 3

Models and Methods

3.1 The Hubbard Model

The fermionic Hubbard model [2,3,4] is a conceptually simple model for the description of interacting electrons hopping on a lattice. However, its simplicity at first sight is misleading since the Hubbard model contains a rich variety of physical phenomena. Written in terms of creation ($c_{i\sigma}^\dagger$ creates an electron with spin $\sigma = \uparrow, \downarrow$ in an orbital on lattice site i) and annihilation operators ($c_{i\sigma}$), which anticommute according to fermionic statistics ($\{c_{i\sigma}, c_{j\sigma'}^\dagger\} = c_{i\sigma}c_{j\sigma'}^\dagger + c_{j\sigma'}^\dagger c_{i\sigma} = \delta_{ij}\delta_{\sigma\sigma'}$, $\{c_{i\sigma}, c_{j\sigma'}\} = \{c_{i\sigma}^\dagger, c_{j\sigma'}^\dagger\} = 0$), the single-band Hubbard model is given by

$$H = \sum_{ij\sigma} t_{ij} c_{i\sigma}^\dagger c_{j\sigma} + U \sum_i n_{i\uparrow} n_{i\downarrow}, \quad (3.1)$$

where $n_{i\sigma} = c_{i\sigma}^\dagger c_{i\sigma}$ is the local particle number operator, t_{ij} is the matrix element for hopping between sites i and j of the lattice ($t_{ji} = t_{ij}^*$), and U is the strength of the on-site Coulomb repulsion, i.e., an amount of energy U that is required for each doubly occupied site. The operator for double occupancy, $n_{i\uparrow} n_{i\downarrow}$, has eigenvalues 0 and 1, and the average double occupancy $D = L^{-1} \sum_i \langle n_{i\uparrow} n_{i\downarrow} \rangle$ (L is the number of lattice sites) is an indicator for the degree of localization of the electrons. Typically D is larger in the metal than in the Mott insulator. Here

$$\langle O \rangle = \frac{\text{Tr } O e^{-\beta H}}{\text{Tr } e^{-\beta H}} \quad (3.2)$$

denotes the quantum-statistical average¹ of the operator O , $\text{Tr} \dots = \sum_n \langle n | \dots | n \rangle$ is the trace (with a Hilbert space basis $\{|n\rangle\}$).

As mentioned above, the Hamiltonian (3.1) contains two important limiting cases. For $U = 0$ it describes non-interacting electrons in delocalized Bloch states moving in a band with dispersion $\epsilon_{\mathbf{k}} = \sum_{ij} e^{i\mathbf{k}(\mathbf{R}_i - \mathbf{R}_j)} t_{ij}$ and bandwidth W . For the following discussion we make a further simplification and consider simple lattices retaining only hopping matrix elements between nearest-neighboring sites. Writing $t_{ij} = -t$ if i and j are nearest neighbors (and $t_{ij} = 0$ else), the single-band Hubbard model takes the even simpler form

$$H = -t \sum_{\langle i,j \rangle_{nn\sigma}} \left(c_{i\sigma}^\dagger c_{j\sigma} + h.c. \right) + U \sum_i n_{i\uparrow} n_{i\downarrow}. \quad (3.3)$$

For very large $U/t \gg 1$ the Hubbard model can be mapped to the t - J model with exchange coupling $J \propto t^2/U$ [16], which contains as a limiting case at half-filling (one spin per site) the spin-1/2 Heisenberg model. The Heisenberg model is a non-trivial quantum spin model, and a discussion of its properties for various cases is beyond the scope of this work. Here we mention only that for bipartite lattices (i.e., lattices which can be divided into two sublattices such that each lattice site has only nearest neighbors of the opposite sublattice) the unfrustrated Heisenberg model exhibits long-range antiferromagnetic order with a finite critical temperature in dimensions $d > 2$ [17,18] and with a critical temperature $T_c = 0$ in $d = 2$ [19,20,21,22].

In between the limits of non-interacting electrons and localized quantum spins (at half-filling), the Hubbard model exhibits a bandwidth-controlled MIT with a critical interaction strength U_c of the order of the bandwidth. In a simplified picture, the MIT can be understood as a phase transition occurring due to the competition between a kinetic energy gain (parametrized by $W \propto t$) by the delocalization of electrons and a

¹We adapt the usual notation $\beta = (k_B T)^{-1}$ and set the Boltzmann constant $k_B = 1$ throughout this work.

potential energy gain (parametrized by U) avoiding the local Coulomb repulsion by localization. More details of the Mott transition with a focus on the limit of infinite dimensions and a contrasting perspective for the two-dimensional Hubbard model will be presented in Sec. 3.4.

In contrast to the strong coupling regime, where antiferromagnetism in the so-called Mott-Heisenberg insulator may appear as an ordered state of localized spins, antiferromagnetic order is also found as a weak-coupling instability, with an energy gain due to the opening of an energy gap by the doubling of the unit cell. The corresponding mechanism is also referred to as the Slater mechanism for antiferromagnetism, and it may be studied within a static mean-field (Hartree-Fock) approximation to the Hubbard model. In general, the tendency of the system to order antiferromagnetically is strongest on lattices with perfect nesting (where a single reciprocal nesting vector connects parts of the Fermi surface), for example on unfrustrated hypercubic lattices with only nearest-neighbor hopping.

Away from half-filling the homogeneous phase of the system may become unstable and the system may show a tendency to exhibit phase separation [23, 24, 25] and to form patterns in real space, e.g., stripes [26]. We note in passing that in contrast to antiferromagnetism, a weak-coupling approach to the Hubbard model does not allow for a ferromagnetic solution. However, one of the few rigorous statements about the Hubbard model is the Nagaoka theorem [27], which states that in the limit of infinite Coulomb repulsion U the ground state of the half-filled system plus a single hole is a fully polarized ferromagnet. The Nagaoka theorem holds for different lattice structures, among them the hypercubic lattice. Ferromagnetic solutions of the Hubbard model at strong but finite U and at finite doping have been studied, e.g., within DMFT [23]. Only recently the existence of a thermodynamic Nagaoka phase was established in the limit of infinite dimensions [28].

While in dimensions $d > 2$ many characteristics of the Hubbard model can be

studied, at least qualitatively, within dynamical or even static mean-field approximations, approximate schemes neglecting non-local quantum fluctuations become more unreliable in two dimensions. However, especially due to the importance of non-local fluctuations the two-dimensional Hubbard model shows rich physics, e.g., unconventional superconductivity [29, 30], the intriguing pseudogap phenomenon observed in the cuprates [31, 32] or the notion of a quantum spin-liquid state [33, 34]. A discussion of numerical studies of the two-dimensional Hubbard model with a focus on unconventional superconductivity will be given in Sec. 3.5.

3.2 Dynamical Mean-Field Theory

The Dynamical Mean-Field Theory (DMFT) is a non-perturbative, controlled and conserving approximation to the full many-body problem. The development of DMFT started with the demonstration of Metzner and Vollhardt [6] that the diagrammatics of fermionic quantum lattice models simplify in an appropriately chosen limit of infinite dimensions or, equivalently, infinite lattice coordination number Z . DMFT became a computational scheme by the insight that the lattice problem can be mapped to a quantum impurity model plus a self-consistency condition in this limit [7, 35]. DMFT thus is the *dynamical* analogue to static Weiss mean-field or Hartree-Fock approximations. The impurity problem is solved by either an approximate analytical scheme or a numerical impurity solver. The results of this work were obtained using a continuous-time quantum Monte Carlo solver, which will be introduced in Sec. 3.6.

In practice DMFT is a useful and successful computational scheme in various contexts. First of all, it allows for an exact solution of the Hubbard model with local interaction in the limit of infinite dimensions. Moreover, the DMFT is a good approximation for three-dimensional electron systems, especially if the number of nearest neighbor ions Z is relatively large, e.g., $Z = 12$ on the face-centered cubic

lattice as compared to $Z = 6$ on the body-centered cubic lattice. Combined with band structure calculations on the basis of density functional theory, DMFT enables material-specific investigations of electronically correlated materials with quantitative predictive power [36]. Finally, by generalizing the DMFT approximation to include non-local correlation effects even two-dimensional models can be studied using a cluster extension of dynamical mean-field theory.

A detailed derivation of the DMFT equations is given, e.g., in the DMFT review article, Ref. [8]. Here we illustrate the DMFT by applying it to the single-band Hubbard model as defined in Eq. (3.1). In this case the basic quantities of DMFT are the following:

- the electronic dispersion relation $\epsilon_{\mathbf{k}}$, which depends on the lattice geometry and the hopping matrix elements t_{ij}
- the local Coulomb interaction strength U
- the one-particle Green function $G(\mathbf{k}, i\omega_n) = (i\omega_n + \mu - \epsilon_{\mathbf{k}} - \Sigma(i\omega_n))^{-1}$
- the one-particle local Green function $G(i\omega_n) = \sum_{\mathbf{k}} G(\mathbf{k}, i\omega_n)$
- the dynamical mean field or “Weiss field” $\mathcal{G}_0(i\omega_n)$
- the local electronic self-energy $\Sigma(i\omega_n)$
- the desired electronic density or band filling n (for fixed filling)² or the chemical potential μ (for fixed chemical potential)

Here $\omega_n = (2n + 1)\pi T = (2n + 1)\pi/\beta$ is the n^{th} fermionic Matsubara frequency³,

²If the filling is fixed, one needs to adjust the chemical potential accordingly. This is typically done during each loop of the self-consistency cycle, see Fig. 3.1.

³The DMFT equations may be formulated equivalently on the real instead of the imaginary frequency axis. The choice depends on whether the impurity solver works on the real-frequency axis, as, e.g., the numerical renormalization group, or on the imaginary (Matsubara) frequency axis, like a solver based on quantum Monte Carlo methods. Since we are using one of the latter we formulate DMFT on the Matsubara axis.

and the relation between the Weiss field and the self-energy will be shown below. Note that we suppress the possible spin dependence of the Green function, the Weiss field and the self-energy for brevity, i.e., we show the equations for a paramagnetic state.

The DMFT is set up by selecting an arbitrary site coined “0” and by defining⁴ the local effective action:

$$S_{\text{eff}} = - \int_0^\beta d\tau \int_0^\beta d\tau' \sum_\sigma c_{0\sigma}^\dagger(\tau) \mathcal{G}_0(\tau - \tau')^{-1} c_{0\sigma}(\tau') + U \int_0^\beta d\tau n_{0\uparrow}(\tau) n_{0\downarrow}(\tau) \quad (3.4)$$

where τ is the imaginary time and the imaginary-time dependent operators in the Heisenberg picture⁵ are given by $c(\tau) = \exp(H_{\text{eff}}\tau)c\exp(-H_{\text{eff}}\tau)$. $\mathcal{G}_0(\tau)$ is the inverse Fourier transform of the Weiss field $\mathcal{G}_0(i\omega_n)$ according to the relations

$$g(\tau) = \beta^{-1} \sum_n \exp(-i\omega_n\tau) g(i\omega_n), \quad (3.5)$$

$$g(i\omega_n) = \int_0^\beta d\tau \exp(i\omega_n\tau) g(\tau), \quad (3.6)$$

where g stands for the Weiss field or the Green function.⁶

The local effective action defines a single-impurity problem which is equivalent to a conveniently chosen single-impurity Anderson model (SIAM) for a given Weiss field \mathcal{G}_0 . An impurity solver is an analytical or numerical method to determine, given the effective action, the local one-particle Green function

$$G(\tau) = -\langle \mathcal{T}_\tau c_0(\tau) c_0^\dagger(0) \rangle_{S_{\text{eff}}}, \quad (3.7)$$

⁴Its relation to the original lattice model can be derived, e.g., using the so-called cavity construction, as shown in Ref. [8].

⁵Note that this notation implies that one knows the effective Hamiltonian H_{eff} corresponding to the effective action S_{eff} . While this is the case for the single-impurity Anderson model, it is not the case in general. Then the imaginary-time dependence of the operators in (Eq. 3.4) should be viewed as a formal expression. In fact it is often more convenient to express the effective action using Grassmann variables and path integrals instead of fermionic operators, see Sec. 3.6.

⁶The Fourier transformation needs to be performed also for the Green function during the self-consistency cycle, which is why we show the relations for a general function g here.

where \mathcal{T}_τ is the imaginary-time ordering operator ensuring the required antiperiodicity of the fermionic Green function with respect to imaginary time shifts of β . Again we have dropped the spin dependence of the operators. The physics of the effective action given by Eq. (3.4) is that of a local impurity embedded in a bath of noninteracting electrons, where U is the energy associated with a double occupancy of the impurity site with a spin-up and a spin-down electron, and the Weiss field contains information about the bath itself and its connection to the impurity site, i.e., hopping processes between the impurity site and the bath.

The Weiss field is related to the lattice degrees of freedom of the original lattice model; it contains all the information about the lattice structure. The mean field needs to be determined self-consistently in an iterative process as detailed below. At this point it is important to note that the Weiss field \mathcal{G}_0 is not equivalent to the non-interacting Green function G_0 of the original lattice model; \mathcal{G}_0 and G_0 merely coincide in the limit $U = 0$.⁷ Therefore \mathcal{G}_0 contains information about the interacting system, while G_0 contains information about the non-interacting system only.

The single-particle self-energy $\Sigma(\omega)$ obtained by DMFT is local and fulfills the equations

$$G(i\omega_n) = \sum_{\mathbf{k}} (i\omega_n + \mu - \Sigma(i\omega_n) - \epsilon_{\mathbf{k}})^{-1}, \quad (3.8)$$

$$\mathcal{G}_0^{-1}(i\omega_n) = G^{-1}(i\omega_n) - \Sigma(i\omega_n), \quad (3.9)$$

the latter of which is the Dyson equation. The functional dependence of $\Sigma(i\omega_n)[\mathcal{G}_0, U]$, defined on the discrete set of Matsubara frequencies $\omega_n = (2n + 1)\pi T$, on \mathcal{G}_0 and U is determined by an auxiliary SIAM.

In practice one starts with some choice of the self-energy, computes the lattice Green function, computes the Weiss field, solves the impurity problem, extracts the

⁷Actually the choice $\mathcal{G}_0 = G_0$, i.e., the free solution, is a convenient starting point for the iterative procedure in practice. Other simple possibilities are the static mean-field (Hartree/Hartree-Fock) solution or the solution of the atomic problem.

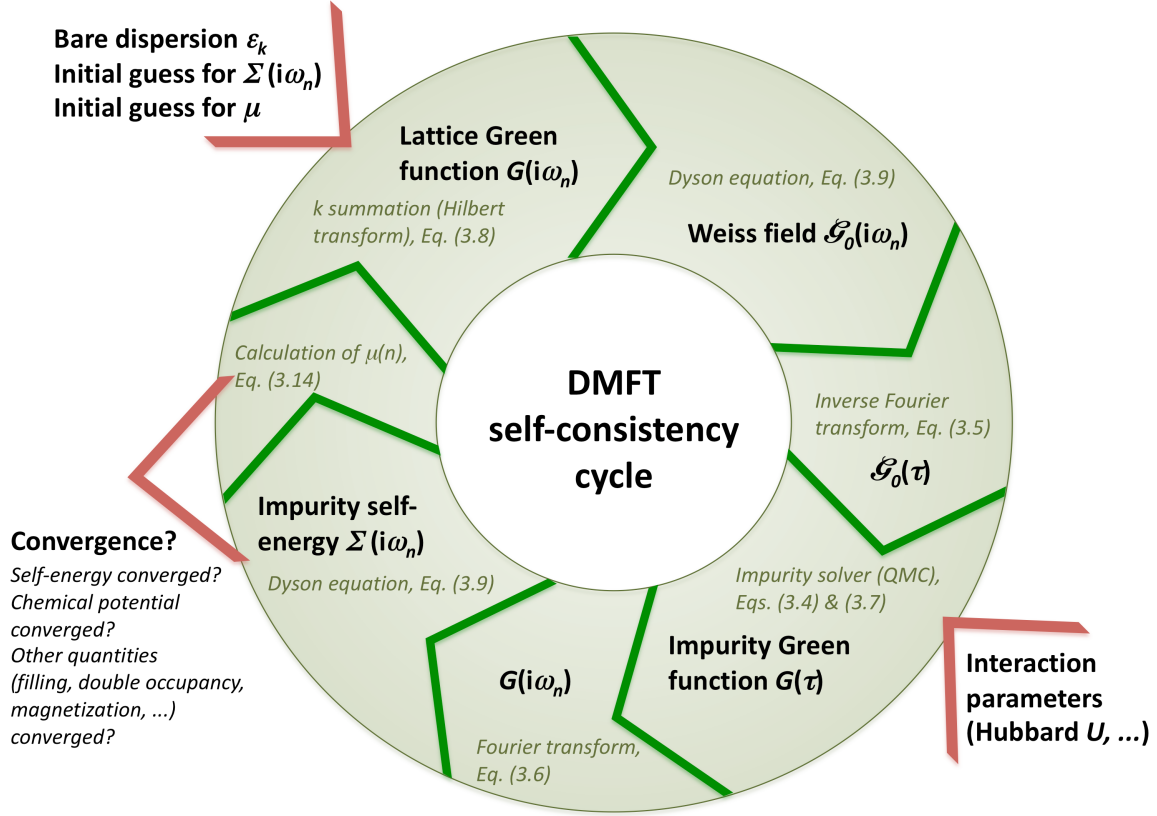


Figure 3.1: Illustration of the DMFT self-consistency cycle for fixed filling n and for an impurity solver which works on the Matsubara axis.

self-energy, and so forth until convergence is achieved. A schematic illustration of this self-consistency scheme is shown in Fig. 3.1.

As indicated in Fig. 3.1 it is necessary to Fourier transform the Green function measured in imaginary time to Matsubara frequencies according to Eq. (3.6) in order to extract the self-energy. Since the local Green function is discontinuous at $\tau = 0$ due to the fermionic anticommutation relations, one needs to take care of this jump in order to obtain the correct asymptotic high-frequency behavior of $G(i\omega_n)$. We

therefore write down the high-frequency expansion of G ,

$$G(i\omega_n) = \frac{c_1}{i\omega_n} + \frac{c_2}{(i\omega_n)^2} + \frac{c_3}{(i\omega_n)^3} + \mathcal{O}\left(\frac{1}{(i\omega_n)^4}\right), \quad (3.10)$$

where the first three coefficients (corresponding to the zeroth, first and second moments of the spectral density) are given by [37]

$$c_1 = -(G(0) + G(\beta)), \quad (3.11)$$

$$c_2 = G'(0) + G'(\beta), \quad (3.12)$$

$$c_3 = -(G''(0) + G''(\beta)). \quad (3.13)$$

For the example of the local Green function $c_1 = -1$.⁸ In principle it is possible to obtain the higher order coefficients from QMC measurements of certain correlations functions (see, e.g., Refs. [37] and [38]) and thus to enforce the correct high-frequency behavior not only of the Green function but also of the self-energy. Such a scheme according to Ref. [38] is used in Chapter 4 to compute also c_2 and c_3 using the average density and the density-density correlator measured in QMC.

As already mentioned, for a solution of the DMFT equations (3.8) and (3.9) at fixed filling the chemical potential needs to be adjusted accordingly. This is achieved by increasing or decreasing the chemical potential with respect to its value in the previous iteration, depending on whether the filling in the previous iteration is too large or too small. This has to be repeated until the filling reaches the desired value for the given self-energy in the present iteration according to

$$n = \sum_{\sigma} \left(1 - \beta^{-1} \sum_n \sum_{\mathbf{k}} (i\omega_n + \mu - \epsilon_{\mathbf{k}} - \Sigma(i\omega_n))^{-1} \right). \quad (3.14)$$

Given a converged solution of the DMFT equations, one can measure in a final QMC run the Green function and other imaginary-time correlation functions, e.g., the local

⁸In the cluster DMFT (see Sec. 3.3.1), for example, also off-diagonal components of the Green function matrix need to be Fourier transformed, where $c_1 = 0$ since the anticommutator of fermionic creation and annihilation operators for different cluster sites vanishes.

spin-spin correlation function, grouping measurements into bins (subsets of measurements). These binned measurements can be used for a statistical error analysis and a subsequent analytical continuation to the real-frequency axis by applying a maximum entropy method [39], which is described in more detail in Appendix A.

Important results obtained with DMFT, especially for the Mott MIT, will be discussed in Sec. 3.4.

3.3 Quantum Cluster Theories

Local correlations are in general the most important correlations in many-body systems. Non-local correlations, however, become essential in low-dimensional systems ($d \leq 2$) and especially at low temperatures. In essence, non-local quantum fluctuations are responsible for such intriguing phenomena as unconventional superconductivity, magnons or spin-liquid phases.

While systems in less than two dimensions, such as Hubbard chains or spin ladders, are successfully studied using techniques like the density-matrix renormalization group (DMRG), two-dimensional quantum many-body systems are especially difficult to approach from a theoretical physicist's point of view. Finite-size methods, such as determinantal or variational QMC, DMRG or exact diagonalization (ED) are limited in system size due to the exponential growth of the Hilbert space. The functional renormalization group (fRG) [40], on the other hand, is by construction restricted to rather weak couplings.

The success of DMFT in describing correlation effects in dimensions higher than two triggered a series of proposed generalized schemes inspired by dynamical mean-field theory:

- quantum cluster theories, such as cellular/cluster DMFT (CDMFT), the dynamical cluster approximation (DCA) and the variational cluster approximation

(VCA) [41],

- the dynamical vertex approximation D Γ A [42],
- the dual-fermion (DF) method [43, 44].

The D Γ A and DF approaches will be briefly discussed at the end of this section. First, we focus on quantum cluster theories and present the relevant schemes and properties.

The idea of finite-size simulations is to approximate the infinite system by an isolated finite part of the system and to extrapolate the results to the bulk thermodynamic limit using scaling arguments. Quantum cluster theories take a different route: The bulk lattice is replaced by an effective finite-sized cluster *embedded* in a self-consistently determined bath. Therefore quantum cluster theories give approximate results for the thermodynamic limit. The different flavors of quantum cluster theories share the properties that they reduce to the single-site DMFT for a cluster of size one and approach the bulk limit upon an increase in cluster size.

In single-site DMFT the electronic self-energy is purely local in real space and therefore constant in momentum space, $\Sigma(\mathbf{k}, i\omega_n) \rightarrow \Sigma(i\omega_n)$. In quantum cluster theories a part of the momentum structure of the self-energy is recovered. In the plaquette CDMFT used in Chapters 5 and 6 of this Thesis one computes, in addition to the local self-energy, also the real-space matrix elements $\Sigma_{ij}(i\omega_n)$ with i and j being sites of a 2×2 plaquette, i.e., nearest- and next-nearest neighbor matrix elements of the self-energy. This corresponds to a momentum-space resolution where $\Sigma(\mathbf{K}, i\omega_n)$ is obtained for $\mathbf{K} = (0, 0)$, $(\pi, 0)$, $(0, \pi)$ and (π, π) .

In all quantum cluster schemes, the self-energy is approximated by a linear combination of N_c basis functions $\Phi_n(\mathbf{k})$ for a cluster of N_c sites:

$$\Sigma(\mathbf{k}, i\omega_n) \rightarrow \Sigma_{\text{cluster}}(\mathbf{k}, i\omega_n) = \sum_{n=1}^{N_c} \Phi_n(\mathbf{k}) \Sigma_n(i\omega_n). \quad (3.15)$$

Single-site DMFT is recovered for $N_c = 1$ with a \mathbf{k} -independent basis function. It is the particular choice of the basis functions which determines the relation between the impurity model and the lattice model for $N_c > 1$. This choice is not unique and differs for example between CDMFT and DCA. In CDMFT, which is built from the real-space cluster perspective, the basis functions are the Fourier phase factors $N_c^{-1} \exp(i\mathbf{k}(\mathbf{R}_i - \mathbf{R}_j))$ and the coefficients are the corresponding cluster self-energies $\Sigma_{ij}(i\omega_n)$. For the example of the plaquette, the independent components are the local self-energy, the self-energy for nearest neighbor sites in x direction, the self-energy for nearest neighbor sites in y direction, and the self-energy for next-nearest neighbor sites along the diagonal. In contrast, in DCA the basis functions are chosen to be constants in certain patches that cover the Brillouin zone, e.g., patches of size $(\Delta k_x, \Delta k_y) = (\pi, \pi)$ around the \mathbf{K} vectors $(0, 0)$, $(\pi, 0)$, $(0, \pi)$ and (π, π) for a 4-site DCA on the square lattice.

The relevance of a momentum-resolved self-energy, even at moderate interaction strength, is illustrated in Fig. 3.2 taken from Ref. [45]. Here the self-energy from quantum cluster theories (in this instance the DCA) for several cluster sizes is compared with the self-energy from an algorithm called diagrammatic Monte Carlo (DiagMC), which directly evaluates diagrams of the lattice problem by Monte Carlo sampling. DiagMC is restricted to rather weak interaction strengths but does not suffer from momentum-space discretization errors. The figure shows the deviation of the self-energy from its constant DMFT value along selected paths in the Brillouin zone and also the convergence of DCA results to the bulk self-energy upon an increase in cluster size.

After these introductory remarks we will now outline the set-up of CDMFT. For most of the presentation we follow the review article on quantum cluster theories, Ref. [41], in which also detailed derivations and discussions of the various flavors of quantum cluster theories can be found.

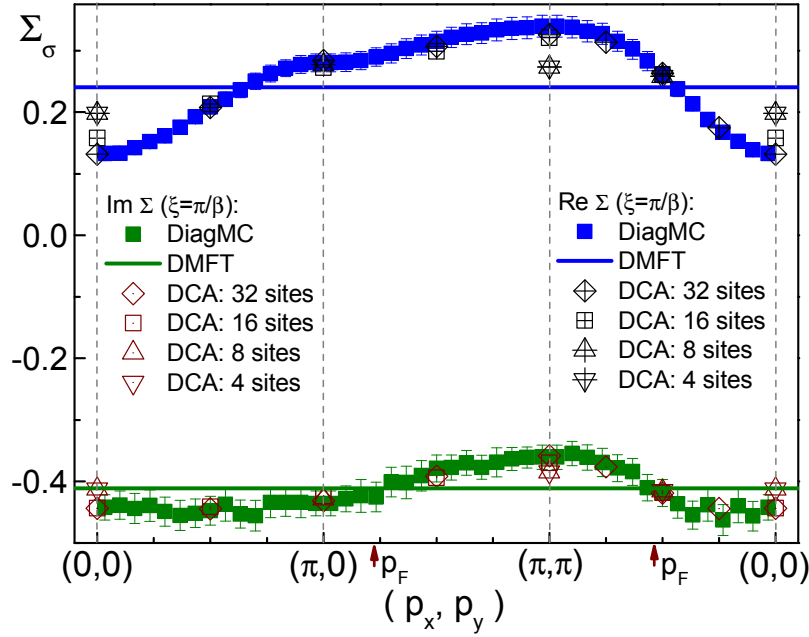


Figure 3.2: Momentum dependence of the self-energy at the lowest Matsubara frequency along the indicated paths in the first Brillouin zone for the two-dimensional square-lattice Hubbard model with parameters $U/t = 4$, $\mu/t = 3.1$ and $T/t = 0.4$. The results were obtained using a diagrammatic Monte Carlo method (DiagMC) and DCA calculations with a continuous-time auxiliary field (CT-AUX) quantum Monte Carlo solver for the indicated cluster sizes. From Ref. [45].

3.3.1 Cluster DMFT

The CDMFT algorithm is based on a division of the infinite lattice into real-space clusters of size N_c . The origins of the clusters form a superlattice with vectors $\tilde{\mathbf{x}}$, and the sites within a cluster are connected to the cluster origin by vectors \mathbf{X} . Thus the position of each site of the lattice can be written as $\mathbf{x} = \tilde{\mathbf{x}} + \mathbf{X}$. Analogously each reciprocal lattice vector in the Brillouin zone is written as $\mathbf{k} = \tilde{\mathbf{k}} + \mathbf{K}$, where \mathbf{K} labels the origin of a Brillouin zone patch and $\tilde{\mathbf{k}}$ are vectors from the patch origin to the momenta within a patch. The division of the lattice and the Brillouin zone is illustrated in Fig. 3.3 for the case of a plaquette cluster.

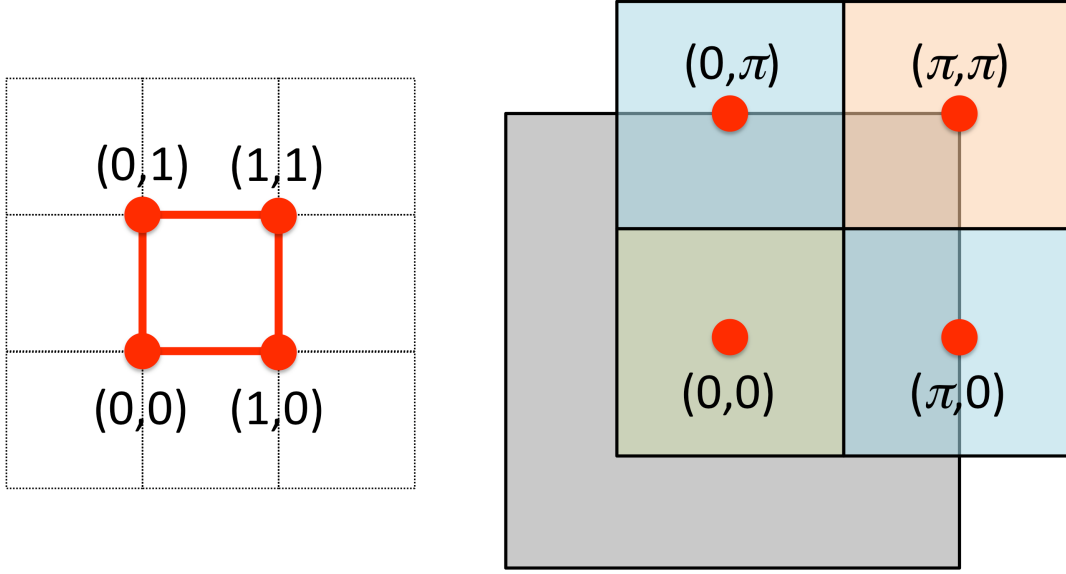


Figure 3.3: Real space and reciprocal space divisions into clusters and patches, respectively.

The CDMFT equations are analogous to the DMFT equations presented above. They read

$$\mathbf{G}(i\omega_n) = \sum_{\tilde{\mathbf{k}}} \left((i\omega_n + \mu)\mathbf{1} - \mathbf{\Sigma}(i\omega_n) - \mathbf{t}(\tilde{\mathbf{k}}) \right)^{-1}, \quad (3.16)$$

$$\mathcal{G}_0^{-1}(i\omega_n) = \mathbf{G}^{-1}(i\omega_n) - \mathbf{\Sigma}(i\omega_n). \quad (3.17)$$

Here the hopping matrix $\mathbf{t}(\tilde{\mathbf{k}})$ is defined via its matrix elements (i and j labeling cluster sites)

$$t_{ij}(\tilde{\mathbf{k}}) = N_c^{-1} \sum_{\mathbf{K}} e^{i(\mathbf{K}+\tilde{\mathbf{k}})(\mathbf{X}_i-\mathbf{X}_j)} \epsilon_{\mathbf{K}+\tilde{\mathbf{k}}}, \quad (3.18)$$

all the quantities (\mathbf{t} , the coarse-grained cluster Green function \mathbf{G} , the corresponding Weiss field \mathcal{G}_0 and the cluster self-energy $\mathbf{\Sigma}$) are $N_c \times N_c$ matrices and we have introduced the $N_c \times N_c$ unit matrix $\mathbf{1}$.

As in the single-site case the self-consistency cycle is closed by solving the impurity

problem, i.e., by calculating, for a given self-energy and the corresponding Weiss field, a new cluster Green function matrix with elements

$$\mathbf{G}_{ij}(\tau) = -\langle \mathcal{T}_\tau c_i(\tau) c_j^\dagger(0) \rangle_{S_{\text{eff}}}, \quad (3.19)$$

where the effective impurity problem is given by the action

$$S_{\text{eff}} = - \int_0^\beta d\tau \int_0^\beta d\tau' \sum_{ij\sigma} c_{i\sigma}^\dagger(\tau) (\mathcal{G}_0(\tau - \tau')^{-1})_{ij} c_{j\sigma}(\tau') + U \int_0^\beta d\tau \sum_i n_{i\uparrow}(\tau) n_{i\downarrow}(\tau). \quad (3.20)$$

The effective impurity problem is an $N_c \times N_c$ cluster problem, with off-diagonal elements of both the Green function matrix and the self-energy matrix.

3.3.2 Superconducting States

It is possible to generalize the cluster DMFT method to include also superconducting states with momentum-dependent order parameter as long as the cluster size is large enough to ensure the relevant momentum space resolution. This is discussed in detail, e.g., in Ref. [29]. We consider superconducting states where the electrons are paired in total spin $S_z = 0$ and total momentum $\mathbf{K} = 0$ states, which may be described by an order parameter $\Delta_{\mathbf{k}} = \langle c_{\mathbf{k}\uparrow} c_{-\mathbf{k}\downarrow} \rangle$. Here it is necessary to introduce the anomalous Green function $F(\mathbf{k}, \tau) = -\langle \mathcal{T}_\tau c_{\mathbf{k}\uparrow}(\tau) c_{-\mathbf{k}\downarrow} \rangle$ in addition to the normal Green function $G(\mathbf{k}, \tau)$. The allowed symmetry of the pairing state is restricted by the cluster geometry. For an order parameter with $d_{x^2-y^2}$ symmetry, which transforms according to $\cos k_x - \cos k_y$, it is necessary to introduce at least a 4-site cluster.

The CDMFT formalism is easily generalized to superconducting states by introducing the concept of Nambu spinors

$$\Psi_{\mathbf{k}}^\dagger = (c_{\mathbf{k}\uparrow}^\dagger, c_{-\mathbf{k}\downarrow}) , \quad \Psi_{\mathbf{k}} = (\Psi_{\mathbf{k}}^\dagger)^\dagger. \quad (3.21)$$

The corresponding 2×2 Nambu Green function matrix in momentum space reads

$$\begin{aligned} G(\mathbf{k}, \tau) &= \begin{pmatrix} -\langle \mathcal{T}_\tau c_{\mathbf{k}\uparrow}(\tau) c_{\mathbf{k}\uparrow}^\dagger \rangle & -\langle \mathcal{T}_\tau c_{\mathbf{k}\uparrow}(\tau) c_{-\mathbf{k}\downarrow} \rangle \\ -\langle \mathcal{T}_\tau c_{-\mathbf{k}\downarrow}^\dagger(\tau) c_{\mathbf{k}\uparrow}^\dagger \rangle & -\langle \mathcal{T}_\tau c_{-\mathbf{k}\downarrow}^\dagger(\tau) c_{-\mathbf{k}\downarrow} \rangle \end{pmatrix} \\ &= \begin{pmatrix} G_\uparrow(\mathbf{k}, \tau) & F(\mathbf{k}, \tau) \\ F^*(\mathbf{k}, \beta - \tau) & G_\downarrow(-\mathbf{k}, \beta - \tau) \end{pmatrix}. \end{aligned} \quad (3.22)$$

For the example of plaquette CDMFT the cluster Green function matrix is diagonal in cluster momentum space. The corresponding cluster momenta are $(0, 0)$, $(\pi, 0)$, $(0, \pi)$ and (π, π) , and the relevant anomalous Green functions for a d -wave order parameter are $F((\pi, 0), \tau) = -F((0, \pi), \tau)$, while the anomalous Green functions vanish at $(0, 0)$ and (π, π) due to the $d_{x^2-y^2}$ symmetry.

A superconducting solution to the CDMFT equations in the repulsive Hubbard model may be found for appropriately chosen parameter values, as shown in Chapter 5. If the CDMFT self-consistency cycle is initiated with a normal-conducting solution, where the anomalous Green functions are zero, one ends up with a normal-conducting solution even if the system has a pairing instability for the chosen parameter values. In order to study superconducting solutions one therefore needs to initialize the self-consistency cycle with a small order parameter, for example $F((\pi, 0), i\omega_n) = -F((0, \pi), i\omega_n) = \Delta$, and then iterate the equations. It is not necessary from our experience to include superconducting source fields in the impurity problem for the first few iterations and switch them off later, although such a procedure might lead to a faster convergence. In each cycle, the anomalous Green functions are measured together with the normal Green functions, and the convergence of all components is required to obtain a fully converged solution. In practice, the superconducting solutions therefore require more CPU time than the normal-conducting ones, and it is advantageous for numerical reasons to probe superconductivity by starting from a converged normal-conducting solution at the same parameter values. If convergence in the superconducting state is achieved, the order parameter is given by $\Delta_{\mathbf{k}} = F(\mathbf{k}, \tau = 0^+)$.

3.3.3 DCA

As discussed in Ref. [41] the CDMFT formalism lacks translational invariance within the cluster, which means that generically the cluster self-energy is not diagonal in momentum space although the lattice problem has translational symmetry.⁹ Therefore in the DCA one restores the translational invariance within the cluster by including a phase factor in the hopping matrix,

$$\mathbf{t}_{ij}^{(\text{DCA})}(\tilde{\mathbf{k}}) = \mathbf{t}_{ij}(\tilde{\mathbf{k}})e^{-i\tilde{\mathbf{k}}(\mathbf{X}_i - \mathbf{X}_j)}. \quad (3.23)$$

Since this hopping matrix is invariant under a translation by a vector \mathbf{X} connecting cluster sites in real space using periodic boundary conditions, its Fourier transform to cluster momentum space is diagonal in the corresponding cluster momenta \mathbf{K} . This means that also the cluster impurity problem has a diagonal kinetic energy part, and in addition the cluster Green function and the cluster self-energy become diagonal in momentum space, which simplifies the solution of the impurity problem in the self-consistency cycle of the DCA.

3.3.4 Other Non-Local Generalizations of DMFT

Apart from cluster generalizations of DMFT there are other approaches which include non-local quantum fluctuations. Rubtsov *et al.* introduced a dual fermion (DF) approach, which is based on a change of Grassmann variables in the path integrals occurring in the action of the many-body problem [43]. The new variables also describe fermionic degrees of freedom and correspond to weakly interacting quasiparticles in the case of strong local correlations in the Hubbard model. Thereby non-local

⁹For the plaquette geometry this problem does not occur, since the self-energy is diagonal in cluster momentum space. The lack of translational invariance becomes important for larger clusters, where also the computational demands grow and it is preferable to resort to the DCA scheme where the impurity problem is diagonal in momentum space. In practice, the CDMFT scheme is therefore typically preferred for smaller clusters, while the DCA is advantageous for larger clusters of size, say, $N_c = 8$ and more.

correlations are treated as perturbations to DMFT in the zeroth order DF approximation. Another generalization, the dynamical vertex approximation (D Γ A) [42], assumes the n -particle irreducible vertex to be local, i.e., D Γ A equals DMFT for $n = 1$ since the one-particle irreducible vertex is the self-energy. The n -particle irreducible vertices as the building blocks of D Γ A are then connected by non-local Green functions to yield, e.g., a non-local self-energy. A first review of results obtained with D Γ A is found in Ref. [46].

3.4 The Mott Transition in Infinite and Two Dimensions

The metal-insulator transition (MIT) in the limit of high dimensions has been intensely studied within DMFT. There are in principle two ways to study the MIT in DMFT: One possibility is to suppress antiferromagnetic order by restricting the DMFT equations to paramagnetic solutions ($\Sigma_{\uparrow} = \Sigma_{\downarrow}$), the other possibility (for a bipartite lattice) is to formulate coupled equations for the two sublattices A and B and to allow for commensurate magnetic ordering by setting $\Sigma_{A\uparrow} = \Sigma_{B\downarrow}$. In the former case the paramagnetic bandwidth-controlled Mott transition is a continuous transition at zero temperature and a discontinuous first-order transition with hysteretic behavior at finite temperatures $T < T_c$ ending in a second-order critical end point at T_c (see also Fig. 3.4). In the latter case it turns out that the Mott MIT is hidden by an antiferromagnetically ordered phase for the unfrustrated model [23].

In two dimensions, however, the situation is different. Here antiferromagnetic long-range order is suppressed at finite temperatures due to stronger quantum fluctuations as compared to higher dimensionality [19,20], although strong short-ranged antiferromagnetic correlations [50] are present. Several non-local generalizations of DMFT, as, e.g., plaquette CDMFT [48] and the variational cluster approximation

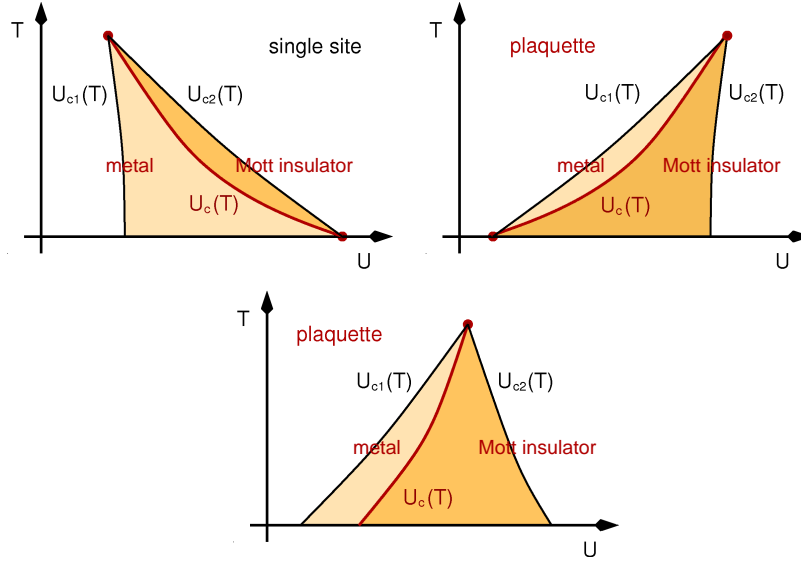


Figure 3.4: Top left: Sketch of the DMFT phase diagram as detailed, e.g., in Ref. [47]. In the shaded region coexistence of a metallic and a Mott insulating solution is found. A first-order Mott transition occurs at $U_c(T)$ (red line), which ends in second-order critical points at $T = T_c$ and $T = 0$. Top right: Phase diagram, as obtained in Ref. [48], within plaquette CDMFT. The first-order line ends in the lower critical interaction strength U_{c1} at $T = 0$. Bottom: Phase diagram supported by plaquette VCA calculations (performed here only at $T = 0$), where the first-order line does not end in a critical point at $T = 0$, but a first-order Mott transition is found even at zero temperature. From Ref. [49].

(VCA) on a plaquette [49] were used to study the Mott MIT and to compare it with the case of infinite dimensions. Apart from the fact that the two different studies of the two-dimensional Mott transition using CDMFT and VCA come to different results with regard to the nature of the zero-temperature limiting behavior, there are several notable differences between the infinite- and two-dimensional cases.

The first difference between the infinite-dimensional (upper left diagram in Fig. 3.4) and the two-dimensional MIT (upper right and bottom diagram) is the size of the critical interaction strength (not shown in the figure): While in DMFT for the infinite dimensional case (Bethe lattice) the critical value of the interaction strength

relative to the bandwidth is approximately $U_c/W = 1.46$ [47], this ratio is considerably smaller in two dimensions, namely approximately $U_c/W = 0.66$ for the plaquette [48]. This decrease in the critical interaction strength with reduced dimensionality may be interpreted as the effect of non-local correlations, which make the system “more strongly correlated” in low dimensions as compared to higher dimensions. At the same time T_c/W decreases from 0.018 to 0.01 from infinite to two dimensions within plaquette CDMFT.

The second difference is the slope of the first-order transition line: In infinite dimensions the critical U increases upon lowering the temperature and coincides with the upper critical interaction strength (indicated by the red dot at $U/W = 1.46$ and $T = 0$ in Fig. 3.4) at zero temperature. In two dimensions the critical U decreases with decreasing temperature. This behavior may be interpreted in physical terms as follows: In infinite dimensions the insulating state has a higher entropy than the metallic state, namely $\ln(2)$ per site, which corresponds to the two degenerate spin directions for each localized spin in the paramagnetic Mott insulator. Thus the insulating state is favored at higher temperatures, while the metallic state becomes more favorable at lower temperatures, where the contribution of the entropy S to the Gibbs free energy $F = E - TS$ is reduced as compared to the inner energy E . In contrast, in two dimensions the Mott insulating state is more complicated, and non-local correlation effects “freeze” the spins already at higher temperatures (although true long-range order is suppressed), thus lowering the entropy of the insulating state. This makes the Mott insulator more favorable at lower temperatures, but the metallic state more favorable at higher temperatures in turn. In fact it was shown in Ref. [50] as well as in Ref. [48] that the insulating phase at low temperature is characterized by a dominant occupation of the plaquette by a single state, namely a singlet configuration of the four electrons. This leads to the fact that the entropy of the insulating state indeed approaches zero at zero temperature, as expected. Since the entropy should

vanish at zero temperature both in the metallic and in the insulating states, the slope of the transition line should become infinite at zero temperature [51]. This is the reason why from a rigorous point of view the scenario shown in the bottom diagram of Fig. 3.4, as obtained in VCA, is more likely¹⁰ than the scenario presented in Ref. [48] (top right diagram). In VCA the MIT is a first-order transition even at $T = 0$, while in CDMFT the MIT at $T = 0$ is continuous. Of course plaquette CDMFT offers an improvement over the single-site DMFT for the two-dimensional Mott transition in the sense that it is a “step in the right direction”, although only a detailed study of the low-temperature Mott transition using larger clusters will provide insight into the “exact” Mott transition in two dimensions.

A third difference, less directly related to the MIT, is the nature of the metallic state below the critical interaction strength. In DMFT the effect of electronic correlations on the system is quantified by the effective mass renormalization $m^*/m = 1/Z$ (see Chapter 2) with the quasiparticle weight Z , which corresponds to a uniform jump in the momentum distribution $n(\mathbf{k}) = \langle c_{\mathbf{k}}^\dagger c_{\mathbf{k}} \rangle$ at the Fermi surface in all \mathbf{k} directions. The quasiparticle weight is calculated from the self-energy as

$$Z = \left(1 - \frac{\partial \text{Re } \Sigma(\omega)}{\partial \omega} \bigg|_{\omega \rightarrow 0} \right)^{-1}, \quad (3.24)$$

and, for the range of frequencies near $\omega = 0$ in which the real part of the self-energy is predominantly linear, the pole in the single-particle Green function is given by the equation

$$\omega - \epsilon_{\mathbf{k}} - \text{Re}\Sigma(\omega) \approx \omega - \epsilon_{\mathbf{k}} - (1 - Z^{-1})\omega = 0, \quad (3.25)$$

hence

$$\omega \approx Z\epsilon_{\mathbf{k}}. \quad (3.26)$$

¹⁰However, the expected infinite slope of the transition line may be visible only at very low temperatures.

This shows that within DMFT the effective dispersion near the Fermi energy is given by the bare dispersion renormalized by a single number, namely Z . DMFT calculations [52] further show that the Z factor is continuously reduced from $Z = 1$ at $U = 0$ to $Z = 0$ at the second-order MIT at zero temperature. Therefore a large Fermi surface is retained in the correlated metal within DMFT even at the verge of the MIT.

In two dimensions, however, the situation is qualitatively different. Here one can still define a \mathbf{k} -dependent renormalization factor $Z_{\mathbf{k}}$, but it might only be well-defined (i.e., take a value between 0 and 1) along certain directions in momentum space in the correlated two-dimensional metal. Imada *et al.* [53] suggested that the MIT in two dimensions is a topological transition, since it is governed by a topological change in the Fermi surface. A discussion is given in terms of the single-particle Green function

$$G(\mathbf{k}, \omega) = \frac{1}{\omega - \epsilon_{\mathbf{k}} - \Sigma(\mathbf{k}, \omega)}, \quad (3.27)$$

the poles and zeros of which have turned out to play an important role in understanding the metal-insulator transition in two dimensions [54, 55, 56, 57]. In the following we will outline the arguments leading to this conclusion: For $\omega \rightarrow -\infty$ the real part of G must be negative, while in the opposite limit $\omega \rightarrow +\infty$ it must be positive. Thus at least one sign change of $\text{Re } G$ must occur for an intermediate value of ω . In a metal such a sign change is provided by poles of $\text{Re } G$, which determine the Fermi surface by the implicit equation $\omega = \epsilon_{\mathbf{k}} + \text{Re} \Sigma(\mathbf{k}, \omega)$ at $\omega = 0$. This is the only possibility for a sign change in the metallic phase if the self-energy is local and thus \mathbf{k} -independent. If, however, the self-energy develops a pole at zero frequency along certain \mathbf{k} directions, then $\text{Re } G$ changes sign by passing through zero, which is also the mechanism of the sign change in insulators, in which no Fermi surface exists at all.

For the two-dimensional Hubbard model on the square lattice, for example, the

bare dispersion is negative at the Brillouin zone center $\mathbf{k} = (0, 0)$ and positive at the zone boundary $\mathbf{k} = (\pi, \pi)$. Hence a sign change of $\text{Re } G$ occurs at $\omega = 0$, e.g., at the Fermi surface for $U = 0$. For a continuous metal-insulator transition (e.g., at the critical end point of the Mott transition) the surface where $\text{Re } G$ changes sign is continuously connected between the non-interacting case and the Mott insulator. Therefore the poles of $\text{Re } G$ need to be continuously replaced by zeros of $\text{Re } G$ (poles of the self-energy) upon approaching the transition. While this takes place exactly at the continuous MIT at zero temperature within DMFT for all \mathbf{k} points, a \mathbf{k} -dependent self-energy allows for \mathbf{k} -space differentiation. In two dimensions a non-Fermi liquid state may thus emerge as a precursor of the MIT in the metallic phase, with a shrinking Fermi surface and the appearance of a “zero surface” (zeros of $\text{Re } G$) as its features.

It is argued, e.g. in Ref. [53], that a topological MIT may trigger non-Fermi liquid behavior in the metallic phase and also lead to unconventional critical behavior at the finite-temperature critical end point of the transition in two dimensions. A related study of unconventional superconductivity emerging from a non-Fermi liquid metal in the frustrated Hubbard model at half-filling will be presented in Chapter 5. Unconventional critical behavior at the critical end point of the Mott transition was observed experimentally [58, 59] in two-dimensional organic conductors. A theoretical investigation of critical exponents at the continuous Mott transition in a two-dimensional Hubbard model related to organic conductors is presented in Chapter 6.

3.5 Unconventional Superconductivity in the 2D Hubbard Model

Conventional superconductors are characterized by broken gauge symmetry, which leads to the notion of phase coherence and the existence of a macroscopic wave function. Provided that an arbitrarily weak attractive interaction exists for electrons with a given relative spin and momentum state, e.g., a singlet state with zero total spin and zero total momentum, the Fermi sea can be shown to become unstable against the formation of Cooper pairs. The superconducting state is then characterized by a non-zero anomalous expectation value (the superconducting order parameter) $\Delta_{\mathbf{k}} = \langle c_{\mathbf{k},\uparrow}^\dagger c_{-\mathbf{k},\downarrow}^\dagger \rangle$, which opens an energy gap in the density of states. In a conventional superconductor the symmetry of the order parameter $\Delta_{\mathbf{k}}$ in momentum space is compatible with the symmetry of the lattice. In other words, a conventional superconductor is defined as a superconductor in which only gauge symmetry is broken. This criterion is fulfilled for an *s*-wave superconductor with a spatially isotropic gap function.

In unconventional superconductors additional symmetries are broken. In a $d_{x^2-y^2}$ -wave superconductor on a square lattice, for example, the order parameter is of the form $\cos k_x - \cos k_y$, i.e., it shows a sign change under rotation by an angle of $\pi/2$, breaking the discrete rotational symmetry of the lattice. In fact, phase sensitive experiments, which can be used to determine the relative sign of the macroscopic wave function at superconductor-superconductor interfaces, provided evidence for such an unconventional state of matter in the superconducting cuprate materials [60].

In the following we will briefly discuss the BCS mean-field approach [61, 62] to superconductivity, show how unconventional order parameter symmetries can occur for momentum-dependent (non-local) pairing interactions and summarize previous results providing evidence for superconducting instabilities in the repulsive two-

dimensional Hubbard model.

3.5.1 BCS Theory

Let us start from a one-band model consisting of the kinetic energy part H_{kin} and the two-body interaction part H_{int} as follows,

$$H = H_{kin} + H_{int}, \quad (3.28)$$

where

$$H_{kin} = \sum_{\mathbf{k}\sigma} \epsilon_{\mathbf{k}} n_{\mathbf{k},\sigma}, \quad (3.29)$$

$$H_{int} = \sum_{\mathbf{k}\mathbf{k}'} V_{\mathbf{k}'\mathbf{k}} b_{\mathbf{k}'}^\dagger b_{\mathbf{k}}. \quad (3.30)$$

The interaction potential is given by the matrix element

$$V_{\mathbf{k}'\mathbf{k}} = \langle \mathbf{k}', -\mathbf{k}' | V | \mathbf{k}, -\mathbf{k} \rangle \quad (3.31)$$

and describes scattering of a pair of electrons from the initial momentum states (\mathbf{k}, \uparrow) and $(-\mathbf{k}, \downarrow)$ to the final momentum states (\mathbf{k}', \uparrow) and $(-\mathbf{k}', \downarrow)$. The electron pairs are represented by the operators

$$b_{\mathbf{k}}^\dagger = c_{\mathbf{k}\uparrow}^\dagger c_{-\mathbf{k}\downarrow}^\dagger, \quad (3.32)$$

$$b_{\mathbf{k}} = c_{-\mathbf{k}\downarrow} c_{\mathbf{k}\uparrow}. \quad (3.33)$$

In their original theory of superconductivity Bardeen, Cooper and Schrieffer used a potential which is attractive when the single-particle energies of the two electrons are both close to the Fermi surface, namely closer than a cutoff energy ω_c . The cutoff energy is the characteristic energy scale of the processes responsible for the superconducting pairing, e.g., the Debye energy in conventional superconductors with phonon-mediated pairing.

In the BCS mean-field approximation the interaction part of the Hamiltonian is simplified using the decomposition

$$\begin{aligned} b_{\mathbf{k}'}^\dagger b_{\mathbf{k}} &= \langle b_{\mathbf{k}'}^\dagger \rangle b_{\mathbf{k}} + b_{\mathbf{k}'}^\dagger \langle b_{\mathbf{k}} \rangle + \left(b_{\mathbf{k}'}^\dagger - \langle b_{\mathbf{k}'}^\dagger \rangle \right) (b_{\mathbf{k}} - \langle b_{\mathbf{k}} \rangle) - \langle b_{\mathbf{k}'}^\dagger \rangle \langle b_{\mathbf{k}} \rangle \\ &\approx \langle b_{\mathbf{k}'}^\dagger \rangle b_{\mathbf{k}} + b_{\mathbf{k}'}^\dagger \langle b_{\mathbf{k}} \rangle + \text{const.} \end{aligned}$$

Using this mean-field approximation, neglecting other possible contractions and ignoring the constant term we obtain the mean-field Hamiltonian

$$H_{mf} = H_{kin} + \sum_{\mathbf{k}\mathbf{k}'} V_{\mathbf{k}'\mathbf{k}} \left(\langle b_{\mathbf{k}'}^\dagger \rangle b_{\mathbf{k}} + b_{\mathbf{k}'}^\dagger \langle b_{\mathbf{k}} \rangle \right). \quad (3.34)$$

Defining the mean field as

$$\Delta_{\mathbf{k}} = \sum_{\mathbf{k}'} V_{\mathbf{k}'\mathbf{k}} \langle b_{\mathbf{k}'}^\dagger \rangle, \quad \Delta_{\mathbf{k}}^* = \sum_{\mathbf{k}'} V_{\mathbf{k}\mathbf{k}'} \langle b_{\mathbf{k}'} \rangle \quad (3.35)$$

we rewrite the mean-field Hamiltonian as

$$H_{mf} = H_{kin} + \sum_{\mathbf{k}} \left(\Delta_{\mathbf{k}} b_{\mathbf{k}} + \Delta_{\mathbf{k}}^* b_{\mathbf{k}}^\dagger \right). \quad (3.36)$$

In order to simplify the notation we introduce Nambu spinors,

$$\Psi_{\mathbf{k}} = \begin{pmatrix} c_{\mathbf{k}\uparrow} \\ c_{-\mathbf{k}\downarrow}^\dagger \end{pmatrix}, \quad \Psi_{\mathbf{k}}^\dagger = \begin{pmatrix} c_{\mathbf{k}\uparrow}^\dagger & c_{-\mathbf{k}\downarrow} \end{pmatrix}. \quad (3.37)$$

Note that these spinors obey the fermionic commutation relations

$$\left\{ \Psi_{\mathbf{k}}, \Psi_{\mathbf{k}'}^\dagger \right\} = \delta_{\mathbf{k}\mathbf{k}'} \mathbf{1}, \quad \left\{ \Psi_{\mathbf{k}}, \Psi_{\mathbf{k}'} \right\} = 0.$$

The Hamiltonian is rewritten as follows:

$$H_{mf} = \sum_{\mathbf{k}} \Psi_{\mathbf{k}}^\dagger \begin{pmatrix} \epsilon_{\mathbf{k}} & \Delta_{\mathbf{k}}^* \\ \Delta_{\mathbf{k}} & -\epsilon_{\mathbf{k}} \end{pmatrix} \Psi_{\mathbf{k}}. \quad (3.38)$$

Here we have dropped a constant term resulting from the reordering of the spin- \downarrow operators. One advantage of the Nambu formalism is that the Hamiltonian (3.38) is readily diagonalized. Its eigenvalues are

$$\lambda_{\pm} = \pm E_{\mathbf{k}} = \pm \sqrt{\epsilon_{\mathbf{k}}^2 + |\Delta_{\mathbf{k}}|^2}. \quad (3.39)$$

The unitary transformation diagonalizing H_{mf} is introduced as follows:

$$H_{mf} = \sum_{\mathbf{k}} \Psi_{\mathbf{k}}^\dagger U^\dagger U \begin{pmatrix} \epsilon_{\mathbf{k}} & \Delta_{\mathbf{k}}^* \\ \Delta_{\mathbf{k}} & -\epsilon_{\mathbf{k}} \end{pmatrix} U^\dagger U \Psi_{\mathbf{k}}, \quad (3.40)$$

where

$$U = \begin{pmatrix} u_{\mathbf{k}} & v_{\mathbf{k}} \\ -v_{\mathbf{k}}^* & u_{\mathbf{k}} \end{pmatrix}, \quad U^\dagger = U^{-1} = \begin{pmatrix} u_{\mathbf{k}} & -v_{\mathbf{k}} \\ v_{\mathbf{k}}^* & u_{\mathbf{k}} \end{pmatrix}, \quad (3.41)$$

so that

$$U \begin{pmatrix} \epsilon_{\mathbf{k}} & \Delta_{\mathbf{k}}^* \\ \Delta_{\mathbf{k}} & -\epsilon_{\mathbf{k}} \end{pmatrix} U^\dagger = \begin{pmatrix} E_{\mathbf{k}} & 0 \\ 0 & -E_{\mathbf{k}} \end{pmatrix}. \quad (3.42)$$

This diagonalization requires that the coefficients of the unitary transformation fulfill the conditions

$$|u_{\mathbf{k}}|^2 = \frac{1}{2} \left(1 + \frac{\epsilon_{\mathbf{k}}}{E_{\mathbf{k}}} \right), \quad |v_{\mathbf{k}}|^2 = \frac{1}{2} \left(1 - \frac{\epsilon_{\mathbf{k}}}{E_{\mathbf{k}}} \right). \quad (3.43)$$

The eigenoperators of H_{mf} are found to be

$$\gamma_{\mathbf{k}} = U \Psi_{\mathbf{k}} = \begin{pmatrix} u_{\mathbf{k}} c_{\mathbf{k}\uparrow} + v_{\mathbf{k}} c_{-\mathbf{k}\downarrow}^\dagger \\ -v_{\mathbf{k}}^* c_{\mathbf{k}\uparrow} + u_{\mathbf{k}} c_{-\mathbf{k}\downarrow}^\dagger \end{pmatrix}. \quad (3.44)$$

Using this we can write

$$H_{mf} = \sum_{\mathbf{k}} \gamma_{\mathbf{k}}^\dagger \begin{pmatrix} E_{\mathbf{k}} & 0 \\ 0 & -E_{\mathbf{k}} \end{pmatrix} \gamma_{\mathbf{k}}. \quad (3.45)$$

In the BCS theory the mean field has to be determined self-consistently, i.e. one has to calculate the expectation values in (3.35) using the mean-field Hamiltonian itself.

The expectation value in (3.35) is evaluated as follows:

$$\begin{aligned} \langle b_{\mathbf{k}'}^\dagger \rangle &= \langle u_{\mathbf{k}'} v_{\mathbf{k}'}^* \gamma_{\mathbf{k}'1}^\dagger \gamma_{\mathbf{k}'1} - u_{\mathbf{k}'} v_{\mathbf{k}'}^* \gamma_{\mathbf{k}'2}^\dagger \gamma_{\mathbf{k}'2} \rangle \\ &= u_{\mathbf{k}'} v_{\mathbf{k}'}^* (f(E_{\mathbf{k}'}) - f(-E_{\mathbf{k}'})), \end{aligned} \quad (3.46)$$

where in the first line we have dropped off-diagonal terms like $\langle \gamma_{\mathbf{k}'1}^\dagger \gamma_{\mathbf{k}'2} \rangle$ and we have introduced the Fermi-Dirac distribution function

$$f(x) = \frac{1}{1 + e^{\beta x}}. \quad (3.47)$$

We proceed employing the equalities

$$u_{\mathbf{k}} v_{\mathbf{k}}^* = \frac{\Delta_{\mathbf{k}}}{2E_{\mathbf{k}}}, \quad (3.48)$$

$$f(E_{\mathbf{k}}) - f(-E_{\mathbf{k}}) = -\tanh\left(\frac{\beta E_{\mathbf{k}}}{2}\right), \quad (3.49)$$

and obtain

$$\langle b_{\mathbf{k}'}^\dagger \rangle = -\frac{\Delta_{\mathbf{k}'}}{2E_{\mathbf{k}'}} \tanh\left(\frac{\beta E_{\mathbf{k}'}}{2}\right). \quad (3.50)$$

Inserting this into (3.35) the self-consistency condition or gap equation is derived as

$$\Delta_{\mathbf{k}} = -\sum_{\mathbf{k}'} V_{\mathbf{k}'\mathbf{k}} \frac{\Delta_{\mathbf{k}'}}{2E_{\mathbf{k}'}} \tanh\left(\frac{\beta E_{\mathbf{k}'}}{2}\right). \quad (3.51)$$

The gap equation is the central equation of BCS theory. From this equation the \mathbf{k} -dependence of the order parameter $\Delta_{\mathbf{k}}$ for a given (effective) electron-electron interaction $V_{\mathbf{k}'\mathbf{k}}$ is determined. If the interaction is attractive near the Fermi surface, i.e. $V_{\mathbf{k}'\mathbf{k}} = -V$ for $\epsilon_{\mathbf{k}'}$ and $\epsilon_{\mathbf{k}}$ (measured from the Fermi energy) within a certain energy range $|\epsilon| < \hbar\omega_c$, the order parameter has the same sign all around the Fermi surface and s -wave superconductivity results:

$$\Delta \propto \omega_c \exp\left(-\frac{1}{N_0 V}\right). \quad (3.52)$$

Here N_0 is the density of states at the Fermi energy.¹¹

Unconventional superconductivity with a more complicated momentum structure of the order parameter may also be described in the framework of an extended BCS theory. Consider for example a repulsive interaction which is enhanced for $\mathbf{k}' - \mathbf{k} = (\pi, \pi)$. One can directly see from Eq. (3.51) that a solution to the gap equation with

¹¹Note that superconductivity emerges from a metallic state with $N_0 > 0$ and is exponentially suppressed for both $V \rightarrow 0$ (weak attraction) or $N_0 \rightarrow 0$ (e.g., in a band insulator) within BCS theory. In fact the same is true for non- s -wave pairing symmetries. In Chapter 5 we will see an example of unconventional superconductivity emerging from a non-Fermi liquid metallic state with a partially depleted Fermi surface. The understanding of the pairing process in such a situation certainly demands concepts going beyond standard BCS theory.

non-zero order parameter may be found if, say, $\Delta_{(\pi,0)} > 0$ and $\Delta_{(0,\pi)} < 0$. This is the reason why repulsive interactions may support d -wave superconductivity with a momentum-dependent order parameter. The pairing interaction can for example be mediated by spin fluctuations with predominant wave-vector $Q = (\pi, \pi)$ leading to an order parameter of the form $\Delta_{\mathbf{k}} = \Delta (\cos k_x - \cos k_y)$. An example of a non-local pairing interaction and the derivation of its momentum structure is presented in the following paragraph.

3.5.2 Non-Local Pairing Interactions

In order to understand how a momentum structure of the interaction vertex supporting unconventional superconductivity may arise from electronic interactions in real space [63], it is instructive to Fourier transform a simple Hamiltonian describing nearest-neighbor attraction on a square lattice,

$$H_{int} = \frac{V}{2} \sum_{\langle ij \rangle \sigma} c_{i\sigma}^\dagger c_{j\sigma}^\dagger c_{j\bar{\sigma}} c_{i\bar{\sigma}}. \quad (3.53)$$

Fourier transformation to momentum space yields

$$\begin{aligned} H_{int} &= \frac{V}{4} \sum_{i\delta\sigma} c_{i\sigma}^\dagger c_{i+\delta\bar{\sigma}}^\dagger c_{i+\delta\bar{\sigma}} c_{i\sigma} \\ &= \frac{V}{4} \sum_{\sigma} \sum_{\mathbf{k}_1 \mathbf{k}_2 \mathbf{k}_3 \mathbf{k}_4} \sum_i e^{i(\mathbf{k}_1 + \mathbf{k}_2 - \mathbf{k}_3 - \mathbf{k}_4)R_i} \sum_{\delta} e^{i(\mathbf{k}_2 - \mathbf{k}_3)R_{\delta}} c_{\mathbf{k}_1\sigma}^\dagger c_{\mathbf{k}_2\bar{\sigma}}^\dagger c_{\mathbf{k}_3\bar{\sigma}} c_{\mathbf{k}_4\sigma} \\ &= \frac{V}{4} \sum_{\sigma} \sum_{\mathbf{k}_1 \mathbf{k}_2 \mathbf{k}_3} \sum_{\delta} e^{i(\mathbf{k}_2 - \mathbf{k}_3)R_{\delta}} c_{\mathbf{k}_1\sigma}^\dagger c_{\mathbf{k}_2\bar{\sigma}}^\dagger c_{\mathbf{k}_3\bar{\sigma}} c_{\mathbf{k}_1 + \mathbf{k}_2 - \mathbf{k}_3\sigma} \\ &= \frac{V}{2} \sum_{\sigma} \sum_{\mathbf{k} \mathbf{k}' Q} (\cos(k_x - k'_x) + \cos(k_y - k'_y)) c_{\mathbf{k}\sigma}^\dagger c_{-\mathbf{k}+Q\bar{\sigma}}^\dagger c_{-\mathbf{k}'+Q\bar{\sigma}} c_{\mathbf{k}'\sigma} \\ &= \sum_{\mathbf{k} \mathbf{k}' Q} \mathcal{V}_{\mathbf{k} \mathbf{k}'} c_{\mathbf{k}\uparrow}^\dagger c_{-\mathbf{k}+Q\downarrow}^\dagger c_{-\mathbf{k}'+Q\downarrow} c_{\mathbf{k}'\uparrow}, \\ \mathcal{V}_{\mathbf{k} \mathbf{k}'} &= V (\cos(k_x - k'_x) + \cos(k_y - k'_y)). \end{aligned} \quad (3.54)$$

In the special case of an attractive interaction $V < 0$ Cooper pairing can occur. With a restriction to singlet pairing we rewrite the pairing interaction,

$$\begin{aligned}
\mathcal{V}_{\mathbf{k}\mathbf{k}'} &= V (\cos k_x \cos k'_x + \cos k_y \cos k'_y + \sin k_x \sin k'_x + \sin k_y \sin k'_y) \\
&\rightarrow V (\cos k_x \cos k'_x + \cos k_y \cos k'_y) \\
&= V ((\cos k_x - \cos k_y) (\cos k'_x - \cos k'_y) + (\cos k_x + \cos k_y) (\cos k'_x + \cos k'_y)) \\
&= \mathcal{V}_{\mathbf{k}\mathbf{k}'}^d + \mathcal{V}_{\mathbf{k}\mathbf{k}'}^s,
\end{aligned} \tag{3.55}$$

where the restriction to singlet pairing requires the pairing interaction to be even in \mathbf{k} and \mathbf{k}' , which is why the sine terms are dropped in the second line, and the d and s contributions to the pairing interaction refer to $d_{x^2-y^2}$ and $s_{\pm} = s_{x^2+y^2}$ pairing symmetry, respectively. Obviously a nearest-neighbor attractive interaction can lead to a variety of possible pairing instabilities. The precise realization of an ordered state therefore does not only depend on the effective pairing interaction but also on the underlying electronic structure. An example for such an interplay between pairing interaction and Fermi surface structure will be briefly discussed in the Outlook. Here we note that an effective attraction between electrons does not necessarily arise due to additional degrees of freedom, like phonons, but it may also occur in purely electronic models with repulsive bare interactions. As an example, the emergence of superconductivity in the repulsive Hubbard model is presented in the following.

3.5.3 Superconductivity in the Repulsive Hubbard Model

The idea that the cuprates bear resemblance in their physical properties to the two-dimensional Hubbard model or the related t - J model was put forward by Anderson already in 1987 [33]. Numerical studies of these models provide evidence for their relationship to the cuprates [64]. In the following we will briefly summarize some basic results in this context.

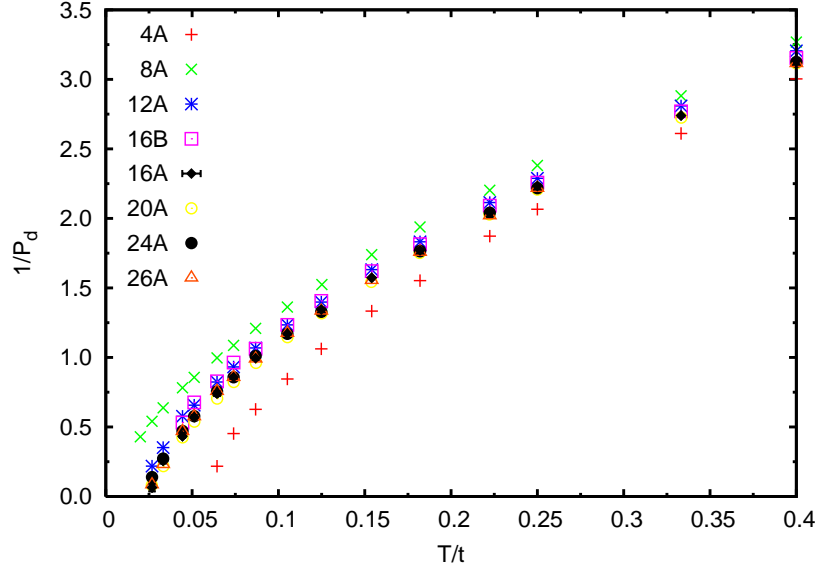


Figure 3.5: Inverse of the d -wave pair-field susceptibility as a function of temperature in units of the hopping, T/t , for various cluster sizes and geometries (the clusters are shown in Ref. [30]) within DCA for interaction strength $U/t = 4$ and filling $n = 0.9$. From Ref. [30].

The undoped cuprates are antiferromagnetic insulators, which corresponds to the ground state of the unfrustrated Hubbard model at half-filling, albeit a finite coupling in the z direction (i.e., some weak three-dimensionality) is required in theory to obtain a finite Néel temperature. Upon doping the cuprates become superconducting with $d_{x^2-y^2}$ order parameter symmetry, and a superconducting pairing instability with d -wave character was also found in theoretical studies using variational Monte Carlo for the doped t - J model [65] and quantum cluster theories for the doped Hubbard model [29, 30, 66, 67, 68]. The results of Maier *et al.* (Ref. [30]) are shown as an example in Fig. 3.5, where the divergence of the d -wave pair-field susceptibility and the convergence of the corresponding superconducting critical temperature with cluster size is seen in DCA calculations.

Similarly, the normal state pseudogap below a characteristic temperature T^* in

the underdoped cuprates, which manifests itself in a suppression of the magnetic susceptibility (seen as a decrease of the Knight shift) [31] or in a suppression in the tunneling density of states [32], is also found in numerical investigations of the Hubbard model [30, 69, 70, 71, 72, 66, 67, 68]. Moreover evidence for stripe correlations from studies of n -leg t - J ladders is interpreted as related to striped states seen in the cuprates [26].

Naturally, due to the above mentioned direct relevance to the cuprates, many studies focus on unconventional superconductivity emerging at finite doping in the strongly coupled Hubbard model. There is, however, a different route to obtain a superconducting ground state in the Hubbard model. Instead of going to strong coupling and choosing the relevant doping regime, we may also ask whether the weakly coupled Hubbard model at half-filling has a superconducting instability as well. One obvious obstacle to such a realization is the perfect nesting condition favoring an antiferromagnetic ground state in the unfrustrated model, which is why one needs to introduce a finite next-nearest neighbor hopping t' to find a superconducting phase at half-filling.

QMC investigations of finite-sized lattices of the U - t - t' Hubbard model at half-filling [73, 74] could not provide conclusive evidence that there might be a second critical U in the problem, apart from the critical U of the Mott transition. A study of the weakly coupled Hubbard model using the functional renormalization group in combination with a mean-field theory with the renormalized effective interactions as input parameters [75] showed that for small values of U a finite t' was required to find d -wave superconductivity. Similar results were obtained using CDMFT with Lanczos exact diagonalization extended to study superconducting and antiferromagnetic states at zero temperature [67] and a variational Monte Carlo approach [76]. In Chapter 5 we present results for the U - t - t' Hubbard model at half-filling, showing evidence from CDMFT calculations that there are indeed two critical U values, one for the transition

from a superconducting state at weak coupling to a non-Fermi liquid metallic state, and a second one for the transition to the Mott insulator.

3.6 Continuous-Time Quantum Monte Carlo

The impurity problem in DMFT algorithms, while conceptually much simpler than the full lattice problem, remains a complicated dynamical many-body problem, and its solution still is a formidable task. Therefore the role of an efficient impurity solver in the practical application of DMFT cannot be overestimated.

DMFT is a controlled and conserving approximation to the many-body problem. Its only approximation is the local approximation, which consists of effectively replacing the non-local electron dynamics by an effective medium, the dynamical mean field. In principle, the local approximation remains the only approximation – provided that one can solve the impurity problem exactly! With the exception of rare limiting cases, however, this is not possible with the methods available today. In all other cases one is forced to resort to a properly chosen impurity solver, which typically entails more approximations beyond the local approximation of the DMFT scheme.

Impurity solvers in general can be classified in two categories: perturbative (diagrammatic) and non-perturbative ones. Among the perturbative solvers are second order perturbation theory, fluctuation-exchange (FLEX) [77,78] approximations and the non-crossing approximation (NCA) [79,80,81,82]. Non-perturbative solvers comprise Quantum Monte Carlo (QMC) [83,84,85], exact diagonalization (ED) [86], Wilson’s numerical renormalization group (NRG) [87,88,89,47] and, yet less widely used in the context of DMFT, the density matrix renormalization group (DMRG) [90]. The main advantage of non-perturbative solvers is that they allow for an accurate treatment of weakly, intermediately and strongly interacting systems. They are reli-

able solvers to study solutions to the DMFT equations across interaction-driven phase transitions.

In this work we exclusively use a certain flavor of QMC, the continuous-time QMC as introduced by Werner and Millis [85]. QMC methods allow to solve impurity problems numerically exactly in the sense that the accuracy is limited only by the invested computer time. In reality QMC is an efficient impurity solver, especially at comparatively high temperatures and for more involved impurity problems such as cluster or multiorbital impurities. Among the non-perturbative impurity solvers the QMC can be viewed as a complementary method to NRG, which is most effective at low or even zero temperature, and for impurities comprising rather few orbitals. In practice, NRG is mostly used at zero temperature, as is the exact diagonalization (ED) technique. The main disadvantage of QMC lies in the fact that it provides information about correlation functions solely on the imaginary time or imaginary frequency axes. Therefore one needs to analytically continue the resulting functions to real frequencies in order to obtain information on dynamical correlation functions, such as the single-particle spectral function, the dynamical spin susceptibility or the optical conductivity.

The basic idea of continuous-time QMC (CTQMC) [91] is to partition the Hamiltonian H into a sum of two parts $H_a + H_b$ and to expand the partition function $Z = e^{-\beta H}$, written in the interaction representation with respect to H_a , in powers of H_b :

$$\begin{aligned}
 Z &= \text{Tr} T_\tau e^{-\beta H_a} \exp \left(- \int_0^\beta d\tau H_b(\tau) \right) \\
 &= \sum_k (-1)^k \int_0^\beta d\tau_1 \dots \int_{\tau_{k-1}}^\beta d\tau_k \\
 &\quad \times \text{Tr} \left(e^{-\beta H_a} H_b(\tau_{k-1}) \dots H_b(\tau_1) \right).
 \end{aligned} \tag{3.56}$$

The trace Tr is performed by contracting the operators appearing in H_b using propagators of the form $e^{-(\tau_i - \tau_j)H_a}$ involving H_a and to use Monte Carlo importance

sampling to obtain numerical estimates of both the sum over perturbation orders k and the integral over imaginary times τ_i . A particular advantage of this technique over time-discretized versions of QMC, like the Hirsch-Fye algorithm [83], is that CTQMC is formulated in continuous imaginary time from the outset. Therefore time discretization error issues (which may be controlled by using multigrid extensions of Hirsch-Fye [92]) do not occur. Moreover, CTQMC does not rely on partitioning the Hamiltonian into non-interacting and interacting parts; rather one is free to choose H_a and H_b to most conveniently solve the problem at hand.

For fermionic impurity problems several flavors of CTQMC have been proposed, among them the interaction-expansion solver (CT-INT), the auxiliary-field solver (CT-AUX) and the hybridization-expansion solver (CT-HYB) [91]. The various flavors differ in the choice of the partitioning of the Hamiltonian, i.e., in the choice of H_b .

The hybridization expansion algorithm CT-HYB [85] is based on the expansion of the impurity partition function Z in the impurity-bath hybridization around the local or atomic limit. One advantage of the hybridization algorithm is that the average expansion order at the Mott transition is smaller than in an interaction expansion method, and therefore lower temperatures are accessible [93].

3.6.1 Hybridization Expansion

Here we will give a derivation of the basic formulas of the hybridization expansion. One may perform this diagrammatic expansion either in terms of the effective impurity action or in terms of the impurity Hamiltonian, respectively. In the following we use the effective action representation. An alternative derivation based on the Hamiltonian can be found in Refs. [85, 93, 37, 91].

One starts from the impurity partition function

$$Z = \int d\Psi^\dagger d\Psi e^{-S}, \quad (3.57)$$

where Ψ^\dagger and Ψ denote a set of anticommuting Grassmann variables and

$$S = S_0 + S_1 \quad (3.58)$$

is the effective impurity action partitioned into the local action S_0 and the impurity-bath hybridization action

$$S_1 = \int_0^\beta d\tau \int_0^\beta d\tau' \sum_a \psi_a^\dagger(\tau) \Delta_a(\tau, \tau') \psi_a(\tau'). \quad (3.59)$$

The sum is over flavors a which label spins and orbitals. Note that we first consider the simplified case where the hybridization matrix $\Delta_a(\tau, \tau')$ is diagonal in the flavors. A generalization to full matrices is straightforward, and a specific example for Nambu matrices used to simulate superconducting states will be considered in the next subsection.

The physical interpretation of the terms in S_1 is the following: At imaginary time τ an electron with flavor a hops from the bath onto the impurity site, stays there from τ to τ' and then hops back into the bath. The hybridization matrix $\Delta_{aa'}(\tau, \tau') = \Delta_{aa'}(\tau - \tau')$ ($= \delta_{aa'} \Delta_a(\tau - \tau')$ for the flavor diagonal-case considered in this subsection) and the Weiss field (cf. Eq. (3.20)) are related through their Fourier transforms to imaginary frequencies,

$$\Delta_{aa'}(i\omega_n) = (i\omega_n + \mu) \delta_{aa'} - (\mathcal{G}_0(i\omega_n)^{-1})_{aa'}. \quad (3.60)$$

The partition function is then expanded in powers of S_1 ,

$$Z = Z_0 \int d\Psi^\dagger d\Psi \frac{e^{-S_0}}{Z_0} \prod_a \sum_{k_a} \tilde{Z}_{k_a}, \quad (3.61)$$

where the k_a -th order coefficient is given by

$$\begin{aligned} \tilde{Z}_{k_a} = & \frac{1}{k_a!} \int_0^\beta d\tau_1 \dots \int_0^\beta d\tau_{k_a} \int_0^\beta d\tau'_1 \dots \int_0^\beta d\tau'_{k_a} \psi_a(\tau'_1) \psi_a^\dagger(\tau_1) \dots \psi_a(\tau'_{k_a}) \psi_a^\dagger(\tau_{k_a}) \\ & \times \Delta_a(\tau_1, \tau'_1) \dots \Delta_a(\tau_{k_a}, \tau'_{k_a}). \end{aligned}$$

We consider the second order contribution for one specific flavor whose index is suppressed in the following,

$$\tilde{Z}_2 = \frac{1}{2} \int_0^\beta d\tau_1 \int_0^\beta d\tau_2 \int_0^\beta d\tau'_1 \int_0^\beta d\tau'_2 \psi(\tau'_1) \psi^\dagger(\tau_1) \psi(\tau'_2) \psi^\dagger(\tau_2) \Delta(\tau_1, \tau'_1) \Delta(\tau_2, \tau'_2).$$

The τ_1 and τ_2 integrations are time ordered such that $\tau_2 > \tau_1$,

$$\begin{aligned} \tilde{Z}_2 = & \frac{1}{2} \int_0^\beta d\tau_1 \int_{\tau_1}^\beta d\tau_2 \int_0^\beta d\tau'_1 \int_0^\beta d\tau'_2 \psi(\tau'_2) \psi^\dagger(\tau_2) \psi(\tau'_1) \psi^\dagger(\tau_1) \\ & \times (\Delta(\tau_1, \tau'_1) \Delta(\tau_2, \tau'_2) - \Delta(\tau_2, \tau'_1) \Delta(\tau_1, \tau'_2)), \end{aligned}$$

where the lower integration limit of the τ_2 integral has been adjusted and the integration variables τ_1 and τ_2 have been renamed accordingly. The minus sign in the brackets stems from the reordering of the Grassmann variables $\psi^\dagger(\tau_1)$ and $\psi^\dagger(\tau_2)$.

The time ordering is applied analogously to the primed integration variables,

$$\begin{aligned} \tilde{Z}_2 = & \frac{1}{2} \int_0^\beta d\tau_1 \int_{\tau_1}^\beta d\tau_2 \int_0^\beta d\tau'_1 \int_{\tau'_1}^\beta d\tau'_2 \\ & \times \left(\psi(\tau'_2) \psi^\dagger(\tau_2) \psi(\tau'_1) \psi^\dagger(\tau_1) (\Delta(\tau_1, \tau'_1) \Delta(\tau_2, \tau'_2) - \Delta(\tau_2, \tau'_1) \Delta(\tau_1, \tau'_2)) \right. \\ & \left. - \psi(\tau'_2) \psi^\dagger(\tau_2) \psi(\tau'_1) \psi^\dagger(\tau_1) (\Delta(\tau_1, \tau'_2) \Delta(\tau_2, \tau'_1) - \Delta(\tau_1, \tau'_1) \Delta(\tau_2, \tau'_2)) \right) \\ = & \int_0^\beta d\tau_1 \int_{\tau_1}^\beta d\tau_2 \int_0^\beta d\tau'_1 \int_{\tau'_1}^\beta d\tau'_2 \psi(\tau'_2) \psi^\dagger(\tau_2) \psi(\tau'_1) \psi^\dagger(\tau_1) \text{Det} \underline{\Delta}. \end{aligned}$$

Here we have collected all the second-order diagrams in a single determinant of a matrix of hybridization functions,

$$\underline{\Delta} = \begin{pmatrix} \Delta(\tau_1, \tau'_1) & \Delta(\tau_1, \tau'_2) \\ \Delta(\tau_2, \tau'_1) & \Delta(\tau_2, \tau'_2) \end{pmatrix}.$$

The same procedure is applied to the integrals appearing in each order k of the expansion:

1. Sort all unprimed times τ_i , $i = 1, \dots, k$ and permute the corresponding Grassmann variables $\psi^\dagger(\tau_i)$. Rename the integration variables accordingly. Every permutation of two Grassmann variables yields a minus sign.
2. Sort all primed times τ'_i , $i = 1, \dots, k$ and permute the Grassmann variables $\psi(\tau_i)$, again rename the variables to compactify the notation.
3. The total number of permutations for the k fermion creation and annihilation processes described by pairs $\psi^\dagger(\tau_i)$, $\psi(\tau_i)$ is given by $k!$, which exactly cancels the prefactor $1/k!$ stemming from the Taylor expansion of the exponential function.
4. The $k!$ terms in the sum and the corresponding minus signs from the reordering of Grassmann variables are absorbed in a single determinant.

Applying this procedure the k -th order coefficient for flavor a is rewritten as

$$\tilde{Z}_{k_a} = \int_0^\beta d\tau_1 \dots \int_{\tau_{k_a-1}}^\beta d\tau_{k_a} \int_0^\beta d\tau'_1 \dots \int_{\tau'_{k_a-1}}^\beta d\tau'_{k_a} \psi_a(\tau'_{k_a}) \psi_a^\dagger(\tau_{k_a}) \dots \psi_a(\tau'_1) \psi_a^\dagger(\tau_1) \text{Det} \underline{\Delta}_a, \quad (3.62)$$

with the determinant defined as

$$\text{Det} \underline{\Delta}_a = \text{Det} \begin{pmatrix} \Delta_a(\tau_1, \tau'_1) & \dots & \Delta_a(\tau_1, \tau'_{k_a}) \\ \vdots & & \vdots \\ \Delta_a(\tau_{k_a}, \tau'_1) & \dots & \Delta_a(\tau_{k_a}, \tau'_{k_a}) \end{pmatrix}. \quad (3.63)$$

This is the basic result for the Monte Carlo sampling of diagrams in the hybridization expansion.

The important point is that one does not need to compute all kinds of products of hybridizations $\Delta(\tau_i, \tau'_j)$, but it is sufficient to compute a single determinant of the hybridization matrix for a given configuration. Thus all the different diagrams for a certain number of annihilation and creation processes are efficiently sampled in a Monte Carlo program. The Monte Carlo sampling and details of the implementation are described in Refs. [85, 93, 37]. For the implementation the ALPS libraries were used [94, 95].

3.6.2 Generalization to Superconducting States

So far we have assumed that the impurity-bath hybridization $\Delta_a(\tau, \tau')$ is flavor-diagonal. A more general formulation of the hybridization expansion renders the simulation of superconducting states possible [96]. The generalized version starts from the impurity-bath hybridization action

$$S_1 = \int_0^\beta d\tau \int_0^\beta d\tau' \sum_{aa'} \sum_{ij} \gamma_{ia}^\dagger(\tau) \Delta_{ij,aa'}(\tau, \tau') \gamma_{ja'}(\tau'). \quad (3.64)$$

The Nambu spinors $\gamma_a^\dagger = (\psi_{\uparrow a}^\dagger, \psi_{\downarrow a})$ with components $i = 1, 2$ corresponding to the two spin species (e.g., $\gamma_{1a}^\dagger = \psi_{\uparrow a}^\dagger$) obey Grassmann spinor anticommutation rules

$$\{\gamma_a, \gamma_{a'}^\dagger\} = \{\gamma_a^\dagger, \gamma_{a'}^\dagger\} = \{\gamma_a, \gamma_{a'}\} = \begin{pmatrix} 0 & 0 \\ 0 & 0 \end{pmatrix}. \quad (3.65)$$

The expansion of the partition function now reads

$$Z = Z_0 \int d\Psi^\dagger d\Psi \frac{e^{-S_0}}{Z_0} \prod_{aa'} \sum_{k_{aa'}} \tilde{Z}_{k_{aa'}}, \quad (3.66)$$

with the expansion coefficients, derived by the same line of arguments as before,

$$\begin{aligned} \tilde{Z}_{k_{aa'}} = & \sum_{i_1 \dots i_{k_{aa'}}} \sum_{j_1 \dots j_{k_{aa'}}} \int_0^\beta d\tau_1 \dots \int_{\tau_{k_{aa'}}-1}^\beta d\tau_{k_{aa'}} \int_0^\beta d\tau'_1 \dots \int_{\tau'_{k_{aa'}}-1}^\beta d\tau'_{k_{aa'}} \\ & \times \gamma_{j_{k_{aa'}}, a'}(\tau'_{k_{aa'}}) \gamma_{i_{k_{aa'}}, a}^\dagger(\tau_{k_{aa'}}) \dots \gamma_{j_1, a'}(\tau'_1) \psi_{i_1, a}^\dagger(\tau_1) \text{Det} \underline{\Delta}_{aa'}, \end{aligned} \quad (3.67)$$

with the determinant defined as

$$\text{Det} \underline{\Delta}_{aa'} = \text{Det} \begin{pmatrix} \Delta_{i_1 j_1, aa'}(\tau_1, \tau'_1) & \dots & \Delta_{i_1 j_{k_{aa'}}, aa'}(\tau_1, \tau'_{k_{aa'}}) \\ \vdots & & \vdots \\ \Delta_{i_{k_{aa'}} j_1, aa'}(\tau_{k_{aa'}}, \tau'_1) & \dots & \Delta_{i_{k_{aa'}} j_{k_{aa'}}, aa'}(\tau_{k_{aa'}}, \tau'_{k_{aa'}}) \end{pmatrix}. \quad (3.68)$$

The implementation of the generalized hybridization algorithm to include superconducting states is straightforward in the Monte Carlo program. It basically requires to interchange the annihilation and creation operators for the down spins and to measure not only the spin-diagonal Green functions but also the anomalous off-diagonal components. It should be noted that a non-zero anomalous Green function for the flavors a and a' is only measured if the corresponding off-diagonal component of the hybridization function, $\Delta_{12, aa'}$, is non-zero. This means that a superconducting bath needs to be introduced by hand as an initial step in the DMFT, which is then determined self-consistently and found to converge to a non-zero solution if the system indeed becomes superconducting.

Chapter 4

Correlations in a Band Insulator

The results of this Chapter have been published in Refs. [97,98].

While the Hubbard model has become a paradigm for the description of electronic correlations in metals and the metal-insulator transition [5], much less attention has so far been paid to electronic correlations in band insulators. E.g., modeling of Kondo insulators is far from trivial, and the only recently achieved progress in the topological classification of band insulators [99] demonstrates that our understanding of the insulating state is still incomplete.

Motivated by several investigations of the ionic Hubbard model [100,101,102,103,104,105,106,107] we have analyzed a covalent insulator as a complementary example of a band insulator. As a covalent insulator we denote a band insulator with partially filled local orbitals. This definition implies that the band gap is a hybridization gap arising from a particular pattern of hopping integrals. It has been proposed that similar characteristics apply to materials such as FeSi, FeSb₂ or CoTiSb [108], some of which exhibit temperature dependent magnetic and transport properties reminiscent of Kondo insulators.

In our model study we use a simple particle-hole symmetric model at half-filling with two semi-circular electronic bands crossing at their respective Fermi levels. Introducing a \mathbf{k} -independent hybridization a band gap is induced in the system since

the hybridization leads to a bonding-antibonding splitting of energy levels. We then introduce a local electron-electron interaction which allows us to study correlation effects on the band insulator.

We use DMFT in conjunction with the recently developed continuous-time QMC [85] to study the evolution from the band insulator at small to the Mott insulator at large Coulomb interaction strength. The insulator-insulator transition is discontinuous at finite but low temperatures, with a region of interaction strengths where hysteretic behavior with two solutions of the DMFT equations is observed. Surprisingly we find that both charge and spin gaps shrink with increasing Coulomb repulsion. This behavior is in contrast to the correlation-induced Mott insulator where the charge gap increases with increasing interaction strength. Furthermore, in the correlated insulator charge and spin gaps deviate from each other, and the spin gap is smaller than the charge gap. From the self-energy we extract a renormalization factor Z defined in the same way as the quasiparticle weight in a Fermi liquid. In the band insulator the Z factor describes the renormalization of the charge gap at moderate interaction strengths (see Fig. 4.7). Thus we obtain the remarkable finding that a concept from Fermi liquid theory can be applied to quantify correlation effects in a band insulator!

4.1 Abstract

We study a model of a covalent band insulator with on-site Coulomb repulsion at half-filling using dynamical mean-field theory. Upon increasing the interaction strength the system undergoes a discontinuous transition from a correlated band insulator to a Mott insulator with hysteretic behavior at low temperatures. Increasing the temperature in the band insulator close to the insulator-insulator transition we find a crossover to a Mott insulator at elevated temperatures. Remarkably, correlations

decrease the energy gap in the correlated band insulator. The gap renormalization can be traced to the low-frequency behavior of the self-energy, analogously to the quasiparticle renormalization in a Fermi liquid. While the uncorrelated band insulator is characterized by a single gap for both charge and spin excitations, the spin gap is smaller than the charge gap in the correlated system.

4.2 Introduction

The role of electron-electron (e-e) interactions in solids is one of the central problems of condensed matter physics. The Hubbard model with local e-e interaction has become a paradigm for the description of electronic correlations in narrow-band materials. It has been used to investigate electronic correlations in metals and to study the correlation-driven metal-insulator transition [5]. Much less attention has been paid to electronic correlations in band insulators (BI), since the lack of low-energy excitations rendered them less interesting.

However, the discoveries of the quantum Hall effect and Kondo insulators showed that BIs are far from trivial, and recent progress in the topological classification of BIs [99] demonstrates that our understanding of the insulating state is indeed incomplete. The quest for materials with topologically non-trivial electronic structures suggests to explore heavier elements with strong spin-orbit coupling involving d or f electrons [109] and raises the question about the role of electronic correlations. The common feature of these materials is that the constituting atoms have partially filled shells and the gap – a hybridization gap – opens due to a particular pattern of inter-atomic hopping integrals. It has been proposed that similar characteristics apply to materials such as FeSi, FeSb₂ or CoTiSb [108], some of which exhibit strongly temperature dependent magnetic and transport properties reminiscent of Kondo insulators. We call this class of BIs covalent insulators (CI).

Recently the evolution of a band insulator (BI) into a Mott insulator upon increasing the interaction strength has been studied in the context of the ionic Hubbard model [100, 101, 102, 103, 104, 105, 106, 107], a two-band Hubbard model with crystal-field splitting [110], and a bilayer model with two identical Hubbard planes coupled by single-particle hopping [111, 112, 113, 114, 115]. Different scenarios have emerged with the possibility of an intervening phase and continuous or discontinuous transitions at critical interaction strengths.

In order to study the properties of CIs with local e-e interaction we employ the dynamical mean-field theory (DMFT) [6, 116, 35, 7, 8]. In particular we are interested in the nature of the interaction-driven transition from a covalent to a Mott insulator, the possible existence of an intervening metallic phase, the evolution of charge and spin gaps and the single-particle self-energy as a function of the interaction strength U .

This paper is organized as follows: In Sec. 4.3 we define the model and the methods chosen to study correlations in the covalent band insulator. The subsequent investigation is guided by the following questions: (i) How does the band insulator at weak coupling evolve into the Mott insulator at strong coupling (Sec. 4.4.1)? (ii) What is the effect of correlations on the spectral function, and what happens when the temperature is increased in the correlated system (Sec. 4.4.2)? (iii) Can we quantify correlation effects in a band insulator by means of concepts analogous to Fermi liquid theory (Sec. 4.4.3)? (iv) Regarding the characterization of a simple band insulator as an insulator with identical charge and spin excitation gaps: Is this picture modified by correlations (Sec. 4.4.4)? Our results are summarized and conclusions are drawn in Sec. 4.5.

4.3 Model and Methods

As a covalent insulator we denote a band insulator with partially filled identical local orbitals. This definition implies that the band gap is a hybridization gap arising from a particular pattern of hopping integrals. Realizations of the covalent insulator include dimerized or bilayer lattices [111, 112, 113, 114, 115], quantum Hall systems with filled Landau levels or Haldane's model [117] and the related model of Kane and Mele [99] describing electrons on a honeycomb lattice with broken time-reversal invariance.

We use a simple particle-hole symmetric model at half-filling described by the Hamiltonian

$$H = \sum_{\mathbf{k}\sigma} \begin{pmatrix} a_{\mathbf{k}\sigma}^\dagger & b_{\mathbf{k}\sigma}^\dagger \end{pmatrix} \mathbf{H}(\mathbf{k}) \begin{pmatrix} a_{\mathbf{k}\sigma} \\ b_{\mathbf{k}\sigma} \end{pmatrix} + U \sum_{i\alpha} n_{i\uparrow\alpha} n_{i\downarrow\alpha}, \quad (4.1)$$

$$\mathbf{H}(\mathbf{k}) = \begin{pmatrix} \epsilon_{\mathbf{k}} & V \\ V & -\epsilon_{\mathbf{k}} \end{pmatrix}, \quad (4.2)$$

with two semi-circular electronic bands of widths $4t$ ($t = 1$ in the following) and dispersions $\epsilon_{\mathbf{k}}$ and $-\epsilon_{\mathbf{k}}$, respectively, corresponding to two sublattices coupled by the \mathbf{k} -independent hybridization V and a local e-e interaction of strength U . Here $n_{i\sigma\alpha} = \alpha_{i\sigma}^\dagger \alpha_{i\sigma}$ measures the number of electrons with spin $\sigma = \uparrow, \downarrow$ on site i of sublattice $\alpha = a, b$. We use the DMFT approximation to calculate the local single-particle propagator and the local spin susceptibility, quantities which within DMFT depend on the lattice only through the non-interacting density of states and thus are independent of a particular realization of the CI. The single-particle self-energy $\Sigma(\omega)$ obtained by DMFT is local and fulfils the equations

$$G(i\omega_n) \mathbf{I} = \sum_{\mathbf{k}} ((i\omega_n + \mu - \Sigma(i\omega_n)) \mathbf{I} - \mathbf{H}(\mathbf{k}))^{-1},$$

$$G_0^{-1}(i\omega_n) = G^{-1}(i\omega_n) - \Sigma(i\omega_n), \quad (4.3)$$

where \mathbf{I} denotes a 2×2 unit matrix. The functional dependence of $\Sigma(i\omega_n)[G_0, U]$, defined on the discrete set of Matsubara frequencies $\omega_n = (2n + 1)\pi T$, on G_0 and U is determined by an auxiliary Anderson impurity problem, for a solution of which we employ the continuous-time quantum Monte-Carlo (CT-QMC) algorithm [85]. For quantities obtained in the imaginary time domain, i.e. the spectral function and the dynamical susceptibility, the analytic continuation to the real-frequency axis is performed using the maximum-entropy method [118].

4.4 Results and Discussion

4.4.1 Phase diagram

The non-interacting ground state ($U=0$) of our model is characterized by a gap in the spectral function of size $\Delta = 2V$ at any $V > 0$. In the $V = 0$ limit we have two decoupled copies of a single-band Hubbard model with semi-circular density of states, a problem which has been extensively studied within DMFT [52, 8]. It is well known that upon increasing the interaction strength U at finite, low temperature the paramagnetic phase undergoes a discontinuous transition from a metal to a MI with a hysteresis in the interval $U_{c1} < U < U_{c2}$ [52]. At high temperatures the hysteretic behavior is replaced by a continuous crossover.

In Fig. 4.1 we show the phase diagram in the T - U plane obtained for $V = 0.5$. At low temperatures two distinct phases exist separated by a discontinuous transition. The phase boundaries were obtained by calculating the double occupancy $D = \langle n_\uparrow n_\downarrow \rangle$, shown in the inset for two selected temperatures. In a finite range of U values we find two stable self-consistent solutions of the DMFT equations.¹ The two phases, adiabatically connected to the band insulator ($U = 0$) and the Mott insulator ($U \rightarrow \infty$), respectively, both exhibit a gap in the single-particle spectral function as discussed

¹For the determination of the critical interaction strength of the BI-MI transition it is necessary to determine and compare the free energy of both coexisting solutions.

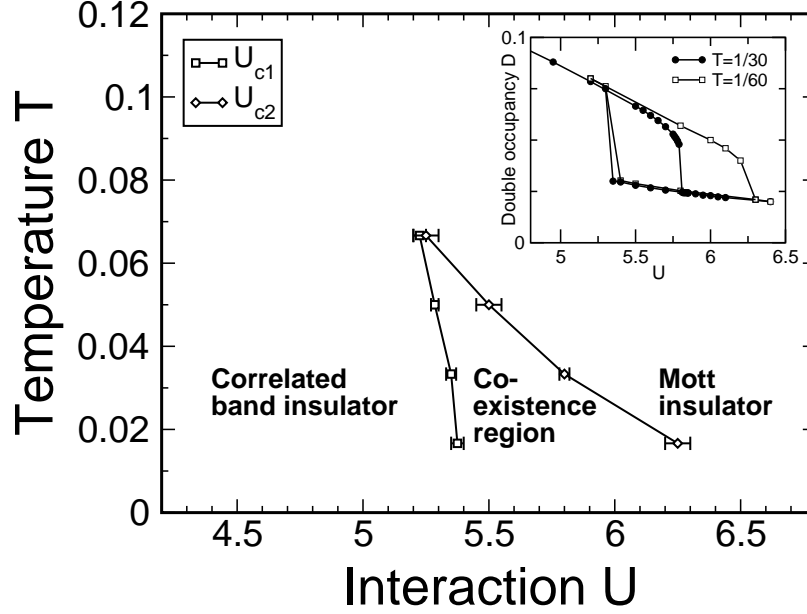


Figure 4.1: T - U phase diagram at fixed $V = 0.5$. The critical values of the interaction strength U are determined from the double occupancy (see inset). Below a critical temperature both band and Mott insulating solutions of the DMFT equations are found depending on the initial guess for the self-energy. For temperatures above the critical end point of the coexistence region, there is a regime where the spectral function has a single peak at the Fermi energy accompanied by broad Hubbard bands (see Fig. 4.3). Inset: The double occupancy $D = \langle n_{\uparrow} n_{\downarrow} \rangle$ as a function of U for $T = 1/30$ (circles) and $T = 1/60$ (squares) indicates the phase transition from the correlated BI (larger D) to the MI (smaller D). Both values of the double occupancy are shown in the region where two solutions are found in the DMFT self-consistency cycle. Note that all energies are given in units of the hopping integral $t = 1$.

below. No signature of an intermittent metallic phase is found. The calculated phase diagram resembles that of a single band Hubbard model including the existence of a critical end point of the discontinuous phase transition, a weak T -dependence of U_{c1} and a considerable increase of U_{c2} upon lowering the temperature [52].

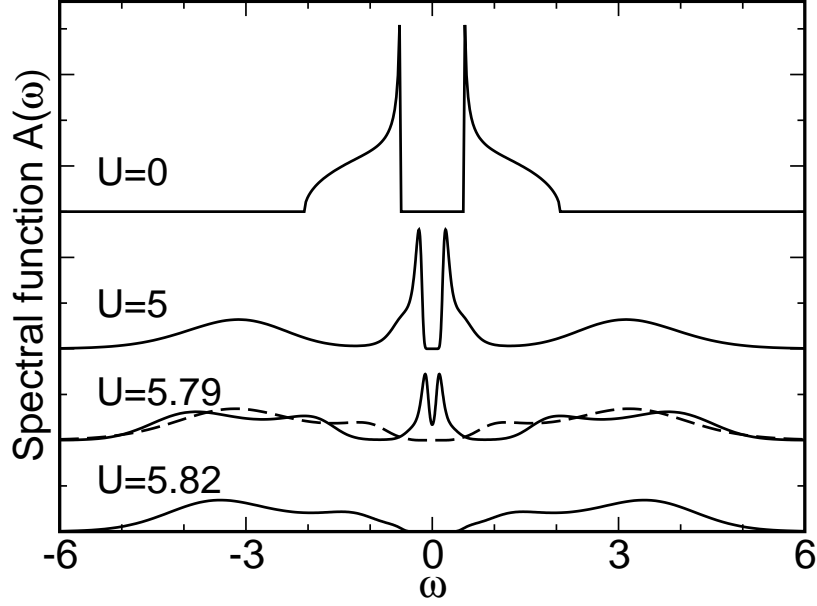


Figure 4.2: Local spectral function $A(\omega)$ at fixed interlayer coupling $V = 0.5$ and temperature $T = 1/30$ for various values of the interaction strength U . The non-interacting density of states ($U = 0$) has a charge gap $\Delta_c = 2V = 1$. The gap in the correlated band insulator shrinks with increasing U until a discontinuous transition to a Mott insulator occurs with a hysteresis region $5.35 < U < 5.82$. For $U = 5.79$ both the band (solid line) and Mott insulating (dashed line) solutions are displayed. All energies are given in units of the hopping integral $t = 1$.

4.4.2 Single-Particle Spectral Function

The evolutions of the spectral function $A(\omega) = -\text{Im } G(\omega + i0^+)/\pi$ along a horizontal $T = 1/30$ and a vertical $U = 5$ line in the phase diagram of Fig. 4.1 are shown in Figs. 4.2 and 4.3, respectively. Remarkably, starting from $U = 0$ the gap in the spectral function shrinks with increasing interaction strength U . At the same time the incoherent Hubbard bands evolve and spectral weight is transferred to them. The gap is well distinguishable throughout the entire interaction range except for a small region in the vicinity of U_{c2} where thermal broadening smears the strongly

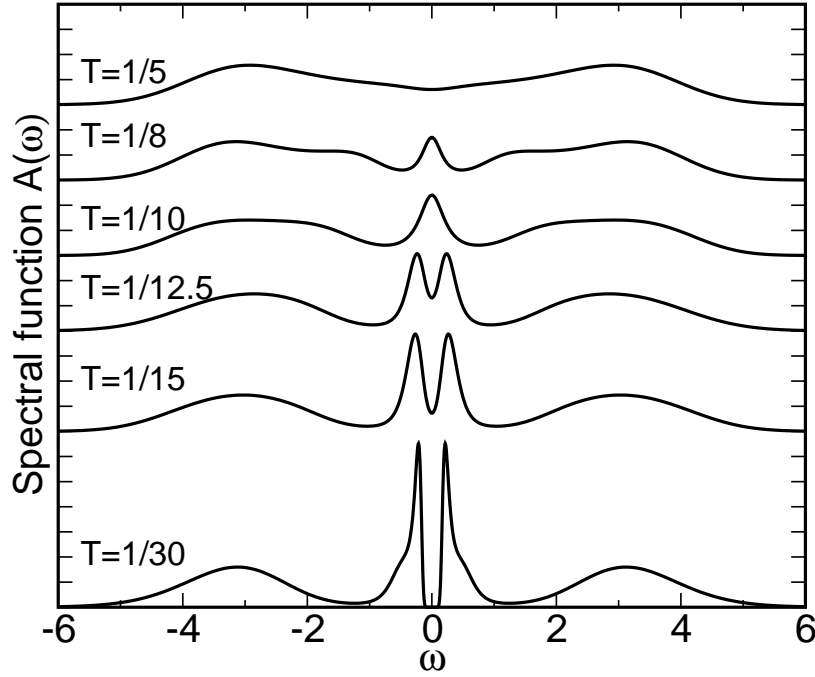


Figure 4.3: Local spectral function $A(\omega)$ at fixed hybridization $V = 0.5$ and interaction strength $U = 5$ for various values of the temperature T . Upon increasing T the correlated band insulator (split peak around $\omega = 0$ plus Hubbard bands) shows a crossover to a Mott insulator (broad Hubbard bands and reduced spectral weight near $\omega = 0$ at $T = 1/5$). At intermediate temperatures ($T = 1/8$ and $T = 1/10$) there is a single peak at the Fermi energy accompanied by broad Hubbard bands. Note that the curves are shifted by a vertical offset for clarity.

renormalized spectral features.

At low T the spectral function in the band insulator phase close to the transition region consists of well distinguishable low-energy quasiparticle bands, separated by the hybridization gap, and incoherent Hubbard bands similar to the single-band Hubbard model. Increasing the temperature the spectral gap is filled in while the quasiparticle bands lose their spectral weight. At $T = 1/10$ the dip at chemical potential has vanished completely and a single peak remains. This peak smoothly disappears upon further increasing the temperature and at $T = 1/5$ only two broad Hubbard bands remain in the spectrum reminiscent of the Mott insulator above the

critical temperature of the metal-insulator transition [52]. In Ref. [108] it was shown that this insulator-to-bad-metal crossover is reflected also in the *dc* and *ac* conductivity and is accompanied by a substantial increase of the spin susceptibility which follows the Curie-Weiss law at high T .

4.4.3 Gap Renormalization and Self-Energy

The spectral densities of Fig. 4.2 reveal a reduction of the charge gap in the CI phase with increasing U . In this section we analyze this behavior which is quantified in Fig. 4.7 showing the charge gap $\Delta_c(U)$ deduced from the spectral densities. In the following we derive the gap renormalization in two different ways from second order perturbation theory. Our derivation closely follows the approach of Ref. [119].

Renormalization of the Charge Gap Deduced from the Total Energy

The charge gap Δ_c in the state with N particles is defined as

$$\Delta_c = (E(N+1) - E(N)) + (E(N-1) - E(N)), \quad (4.4)$$

where $E(N)$ is the ground-state energy of the system with N particles. The first correction to (4.4) from a perturbative expansion in U comes from the 2nd order diagram. Using the factorization of the joint density of states in the limit of infinite dimensions the second order correction to the ground-state energy can be written as

$$E^{(2)} = -\frac{U^2}{L^3} \sum_{p_1, p_2, p_3, p_4} \frac{(1 - n_{p_1\uparrow})n_{p_2\uparrow}(1 - n_{p_3\downarrow})n_{p_4\downarrow}}{\epsilon_{p_1} - \epsilon_{p_2} + \epsilon_{p_3} - \epsilon_{p_4}}, \quad (4.5)$$

where n_{p_i} is the occupation number and ϵ_{p_i} is the energy of the single-particle state with index p_i . The non-interacting N -particle ground state is a band insulator with all states with energies $\epsilon < -V$ filled. The non-interacting $(N+1)$ -particle ground state is obtained by filling the lowest energy state of the empty conduction band $\epsilon_{p_0} = V$ (we choose spin \downarrow from the two possibilities). Keeping only the terms that

do not vanish in the thermodynamic limit and using particle-hole symmetry, which requires that $\Delta_c = 2(E(N+1) - E(N))$, we obtain the second order correction to the charge gap

$$\begin{aligned} \Delta_c^{(2)} = & -2 \frac{U^2}{L^3} \sum_{p_1, p_2, p} (1 - n_{p_1 \uparrow}) n_{p_2 \uparrow} \\ & \times \left[\frac{1 - n_{p \downarrow}}{\epsilon_{p_1} - \epsilon_{p_2} + \epsilon_p - V} - \frac{n_{p \downarrow}}{\epsilon_{p_1} - \epsilon_{p_2} + V - \epsilon_p} \right]. \end{aligned} \quad (4.6)$$

Note that while $E^{(2)}$ is an extensive quantity, the difference in (4.6) remains finite when $L \rightarrow \infty$. Introducing the single-particle density of states D and its Laplace transform F

$$D(\epsilon) = \frac{1}{L} \sum_p \delta(\epsilon - \epsilon_p), \quad F(\lambda) = \int_0^\infty d\epsilon e^{-\lambda\epsilon} D(\epsilon), \quad (4.7)$$

(4.6) can be rewritten as [119]

$$\begin{aligned} \Delta_c^{(2)} = & -2U^2 \int d\epsilon_1 d\epsilon_2 d\epsilon_3 D(\epsilon_1) D(\epsilon_2) D(\epsilon_3) \\ & \times (1 - n_1) n_2 \left[\frac{1 - n_3}{\epsilon_1 - \epsilon_2 + \epsilon_3 - V} - \frac{n_3}{\epsilon_1 - \epsilon_2 + V - \epsilon_3} \right] \\ = & -4U^2 \int_0^\infty d\lambda \sinh(\lambda V) F^3(\lambda), \end{aligned} \quad (4.8)$$

where the fixed spin index has been dropped for simplicity. Introducing the bare gap $\Delta_c^0 = 2V$ we can write the renormalized charge gap as

$$\Delta_c = \Delta_c^0 - 4U^2 \int_0^\infty d\lambda \sinh\left(\lambda \frac{\Delta_c^0}{2}\right) F^3(\lambda). \quad (4.9)$$

This expression shows that the reduction of the charge gap does not depend on the details of $D(\epsilon)$, but rather on its overall characteristics such as the total bandwidth. If Δ_c^0 is small compared to the total bandwidth we can linearize the expression (4.9) to obtain

$$\Delta_c = \Delta_c^0 \left(1 - 2U^2 \int_0^\infty d\lambda F^3(\lambda) \lambda \right). \quad (4.10)$$

In this limit the gap acquires a simple multiplicative renormalization, which is closely related to the quasiparticle mass renormalization as shown below. The perturbative results are compared with the numerical data in Fig. 4.7.

We close this section with two remarks. First, equation (4.5) relies on the equality of the local and the total density of states, which is where the concept of a covalent insulator enters the algebra. Second, the physical origin of the reduction of the gap is best seen in (4.6). Adding a single electron to the insulating states blocks scattering processes with a contribution of the order $-1/4V$ but adds the same number of processes contributing $-1/2V$ and therefore leads to an overall gain in the correlation energy in the $(N + 1)$ -particle state and thus a reduction of the charge gap from its non-interacting value.

Renormalization of the Charge Gap Deduced from the Self-Energy

An alternative derivation of the gap renormalization can be obtained from the perturbative calculation of the self-energy in the insulating ground state. Using the factorization of the joint density of states as in the previous section, the second order contribution to the self-energy is written as

$$\begin{aligned} \Sigma(\omega) = & U^2 \int d\epsilon_1 d\epsilon_2 d\epsilon_3 D(\epsilon_1)D(\epsilon_2)D(\epsilon_3) \\ & \times \frac{(1 - n_1)n_2n_3 + n_1(1 - n_2)(1 - n_3)}{\epsilon_1 - \epsilon_2 + \omega - \epsilon_3}, \end{aligned} \quad (4.11)$$

where the spin indices were dropped as in the previous section. For $-3V < \omega < 3V$ the denominator of the integrand remains negative throughout the entire integration range, the self-energy is therefore real and can be expressed using the Laplace transform (4.7) of the non-interacting density of states

$$\Sigma(\omega) = -2U^2 \int_0^\infty d\lambda \sinh(\lambda\omega) F^3(\lambda). \quad (4.12)$$

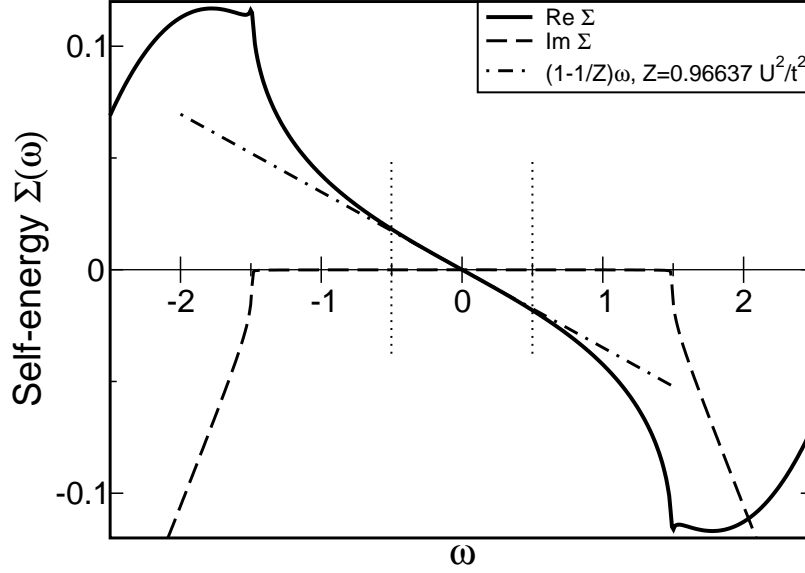


Figure 4.4: The self-energy within second-order weak-coupling perturbation theory at zero temperature (see Eq. (4.11)) for $V = 0.5$. The real part (solid line) is linear around $\omega = 0$; the slope (indicated by the dot-dashed line) determines the Z factor. The imaginary part (dashed line) is gapped for $|\omega| < 3V$. The dotted vertical lines indicate the bare gap $\Delta_c^0 = 1$. The scale of the vertical axis is U^2/t .

The renormalization of the band gap is obtained by searching for the pole Ω of the renormalized propagator of the lowest unoccupied state $\epsilon_{p0} = V$:

$$\Omega - V - \Sigma(\Omega) = 0. \quad (4.13)$$

In the small U limit we can replace $\Sigma(\Omega)$ by $\Sigma(V)$ and with $\Delta_c = 2\Omega$ we recover equation (4.9). As in the previous section we can linearize (4.12) for small V in the interval $|\omega| \lesssim V$, which leads to

$$\Delta_c = Z\Delta_c^0, \quad \text{where } Z = \left(1 - \left.\frac{\partial \text{Re } \Sigma(\omega)}{\partial \omega}\right|_{\omega=0}\right)^{-1}. \quad (4.14)$$

For $|\omega| > 3V$ the second order self-energy acquires a finite imaginary part and expression (4.12) is not applicable. The second order self-energy obtained by numerical integration of (4.11) is shown in Fig. 4.4.

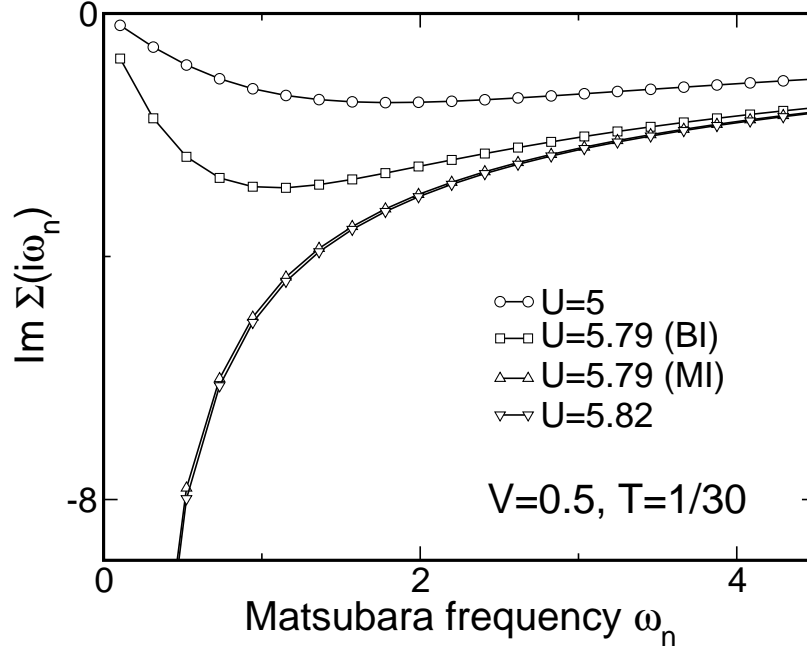


Figure 4.5: Imaginary part of the self-energy as a function of Matsubara frequencies ω_n for three values of the interaction strength U . In the correlated BI the self-energy has a negative slope at small ω_n . In the coexistence region ($U = 5.79$) both solutions are displayed.

The linear behavior of $\text{Re } \Sigma(\omega)$ around the chemical potential is reminiscent of a Fermi liquid. It is not limited to second order perturbation theory, but is a general consequence of a sufficiently fast vanishing of $\text{Im } \Sigma(\omega)$ in the vicinity of the chemical potential and the Kramers-Kronig relations. While in Fermi liquids $\text{Im } \Sigma(\omega) \sim \omega^2$, the existence of a gap in the spectral function of the covalent insulator, as found in the numerical simulations, and the absence of a pole in $\Sigma(\omega)$ inside the gap, imply $\text{Im } \Sigma(\omega) = 0$ throughout the entire gap. As a result, $\text{Re } \Sigma(\omega)$ of the CI phase closely resembles the self-energy of a Fermi liquid. This similarity is made evident in Fig. 4.5 where we show the self-energy on the discrete set of Matsubara frequencies: It is barely distinguishable from the analogous plot obtained for the single-band Hubbard model with comparable parameters [52].

4.4.4 Spin Excitations in the Band Insulator

Typically a band insulator is characterized by identical gaps for charge and spin excitations. So far we have identified the insulator below the critical interaction strength as a “correlated band insulator” due to the fact that it is adiabatically connected to the band insulator at $U = 0$. Naturally the question arises whether spin and charge gaps remain indeed equal in the presence of correlations. To answer this question and to characterize more precisely the correlated band insulator we evaluate the dynamical spin susceptibility and compare spin and charge gaps.

While the spectral function $A(\omega)$ is gapped in both band and Mott insulators (see Fig. 4.2), the spin gap is finite in the BI and zero in the MI. The spin excitation spectrum is reflected in the local dynamical spin susceptibility $\chi_s(\omega)$, which is calculated by a QMC measurement of the imaginary time correlation function $\chi_s(\tau) = \langle S_z(\tau)S_z(0) \rangle$ and the analytic continuation of its Matsubara transform to real frequencies. Here we use the maximum entropy method [118] for the bosonic kernel according to

$$\chi_s(\tau) = \frac{1}{\pi} \int d\omega \frac{e^{-\tau\omega}}{1 - e^{-\beta\omega}} \text{Im } \chi_s(\omega). \quad (4.15)$$

In Fig. 4.6 the imaginary part of the spin susceptibility is shown on the real-frequency axis for $V = 0.5$, $T = 1/30$, and $U \in \{2, 3, 3.5\}$. Similar to the charge gap, the spin gap also shrinks with increasing interaction strength. For a quantitative comparison of correlation effects on spin and charge excitations in the correlated band insulator Fig. 4.6 also shows the bubble diagram calculated from the convolution of the fully dressed local Green functions,

$$\text{Im } \chi_B(\omega) = \pi \int d\epsilon \frac{A(\epsilon)A(\omega - \epsilon) (1 - e^{-\beta\omega})}{(1 + e^{-\beta\epsilon})(1 + e^{-\beta(\omega - \epsilon)})}. \quad (4.16)$$

In the non-interacting limit (not shown) $\text{Im } \chi_B(\omega)$ and $\text{Im } \chi_s(\omega)$ coincide and exhibit an energy gap of size $2V = 1$. In contrast at finite U the curves differ considerably

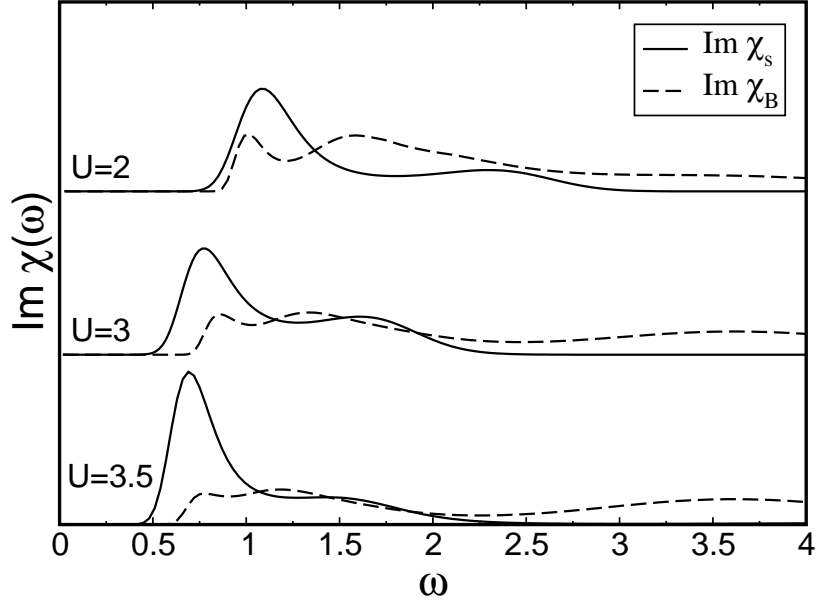


Figure 4.6: Local dynamical susceptibilities in the correlated BI. At $V = 0.5$ and temperature $T = 1/30$ the imaginary parts of the spin susceptibility χ_s (solid lines) and the bubble diagram χ_B (dashed lines) are shown for $U \in \{2, 3, 3.5\}$. The susceptibilities are obtained from the QMC data by analytic continuation. The bubble diagram is calculated from the convolution of the fully-dressed Green functions (see Eq. (4.16)). Thus the gap in $\text{Im } \chi_B(\omega)$ corresponds to the single-particle energy gap in $A(\omega)$, which is apparently larger than the spin gap observed in $\text{Im } \chi_s(\omega)$ in the correlated insulator.

from each other. In the spin susceptibility a prominent peak develops at energies lower than the charge gap. Furthermore spectral weight is suppressed at higher energies which correspond to excitations from the split central peak to the Hubbard bands. The spin susceptibility is thus both qualitatively and quantitatively more strongly influenced by correlations in comparison to the bubble diagram, which contains correlation effects via the renormalized propagator only. The effect of correlations on the band insulator therefore goes beyond the energy gap renormalization discussed in Sec. 4.4.3.

The comparison of the spin susceptibility and the bubble diagram in Fig. 4.6 shows

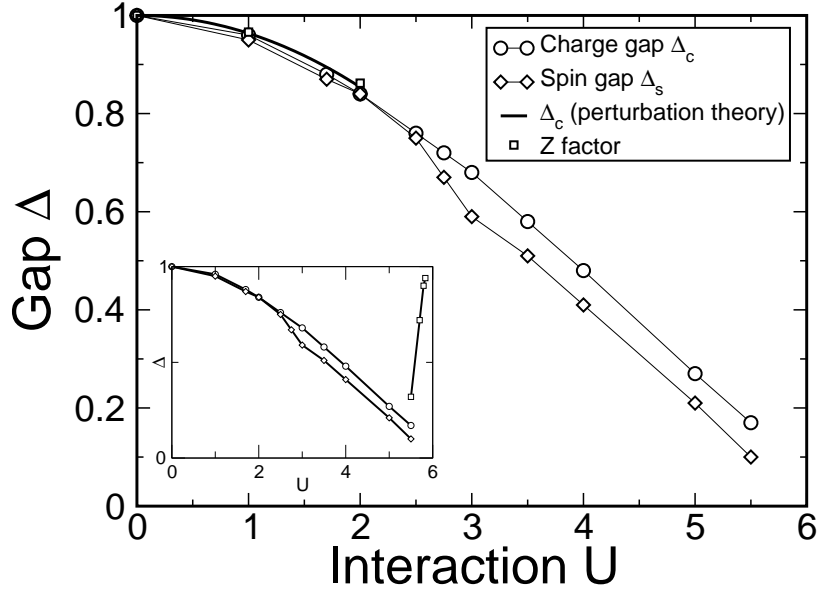


Figure 4.7: Spin and charge gaps in the correlated BI as a function of U for $V = 0.5$ as determined from the spectral function and the spin susceptibility at $T = 1/30$, respectively. The thick solid line shows the charge gap obtained from second order perturbation theory (Eq. (4.9)). The squares represent the Z factor (Eq. (4.14)). Inset: Discontinuous change of spin and charge gaps at the BI to MI transition. In the Mott insulator $\Delta_s = 0$.

that charge and spin gap do not coincide in the correlated BI. For a quantitative analysis we extract the gap values by a linear extrapolation to the frequency axis using the slope at the inflexion point of the spectral function and the imaginary part of the spin susceptibility for the charge and the spin gap, respectively. Fig. 4.7 shows the evolution of charge and spin gaps² with increasing interaction strength in the correlated band insulator. As discussed in Sec. 4.4.3 the energy gap renormalization at moderate coupling strengths is well described by the Z factor (Eq. (4.14)) extracted from the slope of the self-energy at low frequencies. For $U \gtrsim 2.5$ the spin gap is

²Note that spin and charge gaps appear identical for $U = 2$. In Fig. 4.6, however, the gaps in the spin susceptibility and the bubble diagram already differ from each other at $U = 2$. This seeming quantitative discrepancy is due to the fact that we determine the charge gap directly from the spectral function and not from the bubble diagram. In fact the charge gap is obtained slightly larger if it is extracted from the bubble diagram.

smaller than the charge gap, and $\Delta_c - \Delta_s$ remains almost constant with increasing the interaction strength further. Therefore, in contrast to the non-interacting limit, the description of the band insulator as an insulator with identical energy gaps for both charge and spin excitations no longer holds once the interaction is strong enough.

It is worthwhile to point out that different spin and charge gaps were also obtained in the half-filled one-dimensional ionic Hubbard model in the weakly correlated regime, when the ionic potential is smaller than the onsite interaction U [100, 101]. As in the covalent insulator, Δ_c and Δ_s decrease with increasing U . However, the transition to the Mott insulator proceeds via an intermediate insulating phase with bond order and a staggered modulation of the kinetic energy on neighboring bonds.

Hints for a possible difference of spin and charge gaps as obtained in the above discussed correlated band insulator phase exist also from experiments on selected insulating materials. In their study of FeSi Schlesinger *et al.* [120] pointed out the possible difference between spin and charge gaps in correlated insulators based on evidence for a larger charge gap in the Kondo insulator $\text{Ce}_3\text{Bi}_4\text{Pt}_3$ [121, 122]. While the single-particle charge gap can be measured with meV accuracy using photoemission spectroscopy, the determination of the spin gap requires accurate susceptibility measurements to temperatures much lower than the gap energy. The relative gap difference for FeSi, e.g., is expected to be less than 30 % and could so far not be resolved from existing measurements [120].

4.5 Conclusion

We have studied correlation effects in a covalent band insulator using dynamical mean-field theory. In the absence of correlations a band insulator is characterized by its band gap. A local Coulomb repulsion renormalizes the energy gap, which surprisingly shrinks when the interaction strength is increased. In second-order perturbation

theory the gap shrinking can be traced to enhanced low-energy scattering phase space in the conduction band. By analogy to the quasiparticle weight in Fermi-liquid theory a renormalization factor Z can also be introduced in interacting insulators based on the low-frequency behavior of the self-energy. The Z factor in the insulator determines the energy gap renormalization. The simple one-gap picture of the band insulator breaks down for sufficiently large interaction strengths. In the correlated band insulator the spin gap is smaller than the charge gap. A discontinuous transition from the band to the Mott insulator occurs upon increasing the Coulomb repulsion at low but finite temperature. Close to the insulator-insulator transition the increase of temperature in the correlated band insulator with a split central peak and pronounced Hubbard bands leads to a crossover into a high-temperature Mott insulator phase with broad Hubbard bands.

The correlation-driven reduction of the energy gap is rare among the known materials. Nevertheless, this mechanism provides a natural explanation of the uncommon gap overestimation in band-structure calculations of systems like FeSi [123]. Tracing the difference between spin and charge gaps in the correlated band insulator to its physical origin remains a task for future work.

Note added: Recently, a study of correlated semiconductors revealed that a shrinking of the charge gap induced by dynamical correlations is also observed in FeSb₂, a material which is interesting for thermoelectric applications due to its large Seebeck coefficient [124].

Chapter 5

Frustration-Induced Superconductivity in a Non-Fermi Liquid

In this Chapter we present results for the plaquette CDMFT approximation to the two-dimensional Hubbard model in the presence of frustrating next-nearest neighbor hopping. The frustration opens up a possibility for unconventional superconductivity to emerge at half-filling in the weak-coupling regime, where the Coulomb repulsion is below its critical value for the Mott transition in the paramagnetic phase. At the same time, non-local electronic correlations can lead to a non-Fermi liquid normal state even at weak coupling. Indeed we will show in the following that superconductivity emerges from a non-Fermi liquid state in the weakly coupled half-filled system.

At strong coupling the occurrence of superconductivity and the pseudogap phase at finite doping was proposed to be related to stripe correlations [26], quantum criticality associated with an ordered state [125], hidden order [126], or a “quantum-critical point without an ordered state” [127], which was suggested to mark the crossover from a non-Fermi liquid to a Fermi liquid at zero temperature. In contrast, at weak coupling and half-filling stripe correlations are not expected to play a role. Following arguments based on functional renormalization group calculations [128, 129, 130], the partial vanishing of the Fermi surface and the concomitant observation of weak-coupling pseudogap behavior is possibly favored by the occurrence of hot spots near

the $(\pi, 0)$ and $(0, \pi)$ points, i.e., points at which the Fermi surface and the umklapp surface (the line connecting the $(\pi, 0)$ and $(0, \pi)$ points) intersect. In any case the emergence of superconductivity from a non-Fermi liquid state at weak coupling triggers the intriguing question how both the superconducting and the non-Fermi liquid states are related to their strong-coupling counterparts.

5.1 Abstract

We explore superconducting and normal-state properties of the two-dimensional U - t - t' Hubbard model on a square lattice using cellular dynamical mean-field theory on a plaquette. For non-zero values of the next-nearest neighbor hopping t' a d -wave superconducting state emerges upon cooling from a non-Fermi liquid state with an enhanced self-energy for the lowest Matsubara frequency at the $(\pi, 0)$ point. At the lowest accessible temperature, $T = 0.01t$, we observe at least two critical U values: A lower critical U for the transition from the superconducting state at weak coupling to a non-Fermi liquid metallic state, and the critical U of the Mott transition. Our findings open a different route for anomalous metallic properties in the vicinity of an unconventional superconducting phase, in addition to the scenario of doping into a Mott insulator.

5.2 Introduction

The remarkable properties of the hole-doped cuprates, with an apparent non-Fermi liquid normal state, the enigmatic pseudogap phase, and unconventional superconductivity emerging from a state in which well-defined quasiparticles are absent near the $(\pi, 0)$ point of the Brillouin zone, have triggered enormous research activity. It was proposed that the pseudogap is related to a quantum-critical point associated with an ordered state [125], or located at the transition from a non-Fermi liquid (NFL) to a

Fermi-liquid (FL) ground state without necessitating the existence of order [127]. In this context the two-dimensional Hubbard model at strong coupling and finite doping has been studied as a generic minimal model of interacting fermions relevant to the cuprates [30, 131, 132, 133].

The possible existence of a superconducting ground state in the half-filled Hubbard model has received comparatively little attention. At half-filling and for only nearest-neighbor hopping the system is an antiferromagnetic insulator at zero temperature [134]. However, the suppression of antiferromagnetic correlations by a frustrating next-nearest neighbor hopping leads to conditions where insulating behavior is suppressed [74] and unconventional superconductivity may be possible. The competition or coexistence of antiferromagnetic and superconducting orders at zero temperature were studied by a renormalized mean-field method [75] and by cellular dynamical mean-field theory [67]. For the case of weak coupling it was shown that a sufficiently strong next-nearest neighbor hopping may indeed render a superconducting ground state possible.

The phenomenon of a weak-coupling pseudogap and concomitant deviations from Fermi-liquid behavior of the self-energy, most prominently in proximity to so-called hot spots, were reported in Refs. [129, 130] by means of the functional renormalization group. It was shown that in certain directions in momentum space the imaginary part of the self-energy may develop a pronounced peak at low frequencies, indicating a breakdown of the quasiparticle concept for the corresponding momenta. Similarly a single-site DMFT study provided evidence that the existence of van-Hove singularities in the non-interacting density of states can lead to a self-energy with non-Fermi liquid features at low temperatures, even if non-local correlations are not taken into account [135]. In the two-dimensional Hubbard model, however, non-local correlation effects lead to a momentum-space differentiation with consequences such as Fermi-arc formation [57] and a pseudogap phenomenon related to short-ranged spin fluctuations

[41, 72, 70].

Here we extend the preceding studies and investigate both the normal and anomalous self-energies at finite temperatures, focusing on the weak-coupling regime of the Hubbard model at half-filling. To this end we use a plaquette dynamical-mean field approximation, in which dynamical correlations within a 2×2 cluster are treated exactly and longer-range correlations are treated on a mean-field level. Including a next-nearest neighbor hopping, which frustrates antiferromagnetism, we identify an extended regime of weak interaction strength where d -wave superconductivity (dSC) emerges from a NFL state with a partially depleted Fermi surface near $(\pi, 0)$. Thus an interesting analogy between the frustrated half-filled weakly coupled system and the hole-doped strongly coupled system is revealed.

5.3 Model and Methods

We study the two-dimensional one-band U - t - t' Hubbard model (see Fig. 5.1) with the Hamiltonian

$$H = \sum_{\mathbf{k}, \sigma} \epsilon_{\mathbf{k}} c_{\mathbf{k}, \sigma}^{\dagger} c_{\mathbf{k}, \sigma} + U \sum_i n_{i, \uparrow} n_{i, \downarrow}, \quad (5.1)$$

where $c_{\mathbf{k}, \sigma}^{\dagger}$ ($c_{\mathbf{k}, \sigma}$) creates (annihilates) an electron in a Bloch state with lattice momentum \mathbf{k} , $n_{i, \sigma}$ is the local density operator for site i and spin $\sigma = \uparrow, \downarrow$, $U > 0$ is the local Coulomb repulsion strength and the electronic dispersion is given by

$$\epsilon_{\mathbf{k}} = -2t (\cos k_x + \cos k_y) - 4t' \cos k_x \cos k_y. \quad (5.2)$$

Throughout this work we use energy units such that $t = 1$. Since we study the half-filled system we are free to choose either positive or negative sign of the relative next-nearest neighbor hopping amplitude t'/t , since for $n = 1$ the dispersion has the symmetry $\epsilon_{(k_x + \pi, k_y + \pi)}(t') = -\epsilon_{\mathbf{k}}(-t')$.

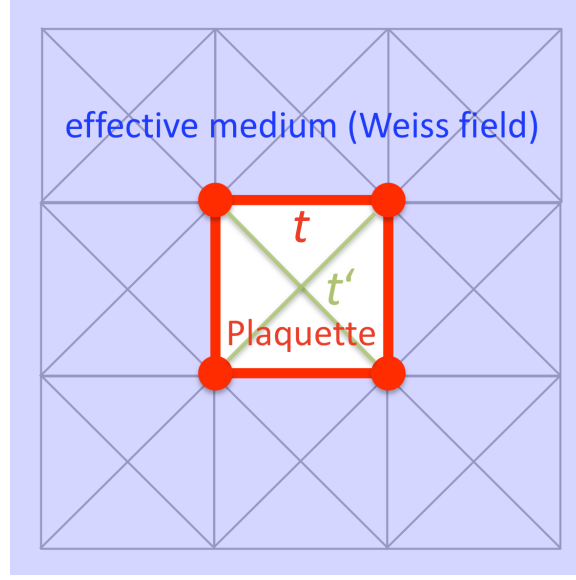


Figure 5.1: U - t - t' Hubbard model on the two-dimensional square lattice with nearest neighbor hopping t and next-nearest neighbor hopping t' . Within plaquette CDMFT a plaquette impurity is singled out, and the rest of the lattice is replaced by an effective medium which is determined self-consistently.

We use the cellular dynamical mean-field theory (CDMFT) for a 2×2 (plaquette) cluster geometry (see Fig. 5.1). The CDMFT equations [136, 41] read

$$\mathbf{G}(i\omega_n) = \sum_{\tilde{\mathbf{k}}} \left((i\omega_n + \mu)\mathbf{1} - \boldsymbol{\Sigma}(i\omega_n) - \mathbf{t}(\tilde{\mathbf{k}}) \right)^{-1}, \quad (5.3)$$

$$\mathcal{G}_0^{-1}(i\omega_n) = \mathbf{G}^{-1}(i\omega_n) - \boldsymbol{\Sigma}(i\omega_n). \quad (5.4)$$

Here the hopping matrix $\mathbf{t}(\tilde{\mathbf{k}})$ is defined via its matrix elements (i and j labeling cluster sites)

$$t_{ij}(\tilde{\mathbf{k}}) = N_c^{-1} \sum_{\mathbf{K}} e^{i(\mathbf{K} + \tilde{\mathbf{k}})(\mathbf{x}_i - \mathbf{x}_j)} \epsilon_{\mathbf{K} + \tilde{\mathbf{k}}}. \quad (5.5)$$

All the quantities (\mathbf{t} , the coarse-grained cluster Green function \mathbf{G} , the corresponding Weiss field \mathcal{G}_0 and the cluster self-energy $\boldsymbol{\Sigma}$) are $N_c \times N_c$ matrices and we have introduced the $N_c \times N_c$ unit matrix $\mathbf{1}$. The self-consistency cycle is closed by solving the

impurity problem, i.e., by calculating, for a given self-energy and the corresponding Weiss field, a new cluster Green function matrix with elements

$$\mathbf{G}_{ij}(\tau) = -\langle \mathcal{T}_\tau c_i(\tau) c_j^\dagger(0) \rangle_{S_{\text{eff}}}, \quad (5.6)$$

where the effective impurity problem is given by the action

$$S_{\text{eff}} = - \int_0^\beta d\tau \int_0^\beta d\tau' \sum_{ij\sigma} c_{i\sigma}^\dagger(\tau) (\mathcal{G}_0(\tau - \tau')^{-1})_{ij} c_{j\sigma}(\tau') + U \int_0^\beta d\tau \sum_i n_{i\uparrow}(\tau) n_{i\downarrow}(\tau). \quad (5.7)$$

The CDMFT formalism is generalized to superconducting states by introducing the concept of Nambu spinors

$$\Psi_{\mathbf{k}}^\dagger = (c_{\mathbf{k}\uparrow}^\dagger, c_{-\mathbf{k}\downarrow}), \quad \Psi_{\mathbf{k}} = (\Psi_{\mathbf{k}}^\dagger)^\dagger. \quad (5.8)$$

The corresponding 2×2 Nambu Green function matrix in momentum space reads

$$\begin{aligned} G(\mathbf{k}, \tau) &= \begin{pmatrix} -\langle \mathcal{T}_\tau c_{\mathbf{k}\uparrow}(\tau) c_{\mathbf{k}\uparrow}^\dagger \rangle & -\langle \mathcal{T}_\tau c_{\mathbf{k}\uparrow}(\tau) c_{-\mathbf{k}\downarrow} \rangle \\ -\langle \mathcal{T}_\tau c_{-\mathbf{k}\downarrow}^\dagger(\tau) c_{\mathbf{k}\uparrow}^\dagger \rangle & -\langle \mathcal{T}_\tau c_{-\mathbf{k}\downarrow}^\dagger(\tau) c_{-\mathbf{k}\downarrow} \rangle \end{pmatrix} \\ &= \begin{pmatrix} G_\uparrow(\mathbf{k}, \tau) & F(\mathbf{k}, \tau) \\ F^*(\mathbf{k}, \beta - \tau) & G_\downarrow(-\mathbf{k}, \beta - \tau) \end{pmatrix}. \end{aligned} \quad (5.9)$$

For the example of the plaquette CDMFT the cluster Green function matrix is diagonal in cluster momentum space [137]. The corresponding cluster momenta are $(0, 0)$, $(\pi, 0)$, $(0, \pi)$ and (π, π) , and the relevant anomalous Green functions for a d -wave order parameter are $F((\pi, 0), \tau) = -F((0, \pi), \tau)$, while the anomalous Green functions vanish at $(0, 0)$ and (π, π) due to the $d_{x^2-y^2}$ symmetry. If convergence in the superconducting state is reached, the order parameter is given by

$$\Delta_{\mathbf{k}} = F(\mathbf{k}, \tau = 0^+). \quad (5.10)$$

The cluster impurity problem is solved by the continuous-time quantum Monte Carlo algorithm based on the expansion of the effective action in the impurity-bath hybridization [85], generalized to include superconducting states [96]. We mention that

the plaquette geometry generally tends to overestimate the superconducting order parameter for d -wave pairing within the CDMFT framework. As shown by Maier *et al.* within the dynamical cluster approximation for the unfrustrated doped two-dimensional Hubbard model [30] a quantitative estimate of the critical temperature may be achieved by a systematic cluster-size scaling analysis. Here we restrict our study to the plaquette and rather investigate the overall phase diagram than focus on the critical temperature for a specific parameter set. Also we do not aim at investigating possible coexistence of superconducting and antiferromagnetic phases [29] but study paramagnetic solutions at finite temperature, where superconductivity is nevertheless expected to be influenced by short-ranged antiferromagnetic correlations [50] even in the absence of magnetic long-range order.

5.4 Results and Discussion

We focus on the half-filled system and present the main results of our study in the phase diagram shown in Fig. 5.2. At half-filling the two-dimensional Hubbard model is known to exhibit a transition from a metal to a Mott insulator (the Mott transition) [48] upon an increase in the local Coulomb repulsion U , with a critical interaction strength which increases slightly when a next-nearest neighbor hopping t' is introduced [138]. For the results shown in Fig. 5.2 the temperature $T = t/100$ is chosen to be well below the critical temperature of the end point of the Mott transition, and the data points shown for the Mott insulating phase indicate the insulating solutions above the critical interaction strength of the discontinuous Mott transition. Upon introducing a finite next-nearest neighbor hopping t' the system develops a d -wave superconducting (dSC) instability at weak coupling in a range of U values which increases upon an increase in t' . Thus we observe a frustration-induced superconducting phase in the weakly coupled Hubbard model at half-filling. Remarkably,

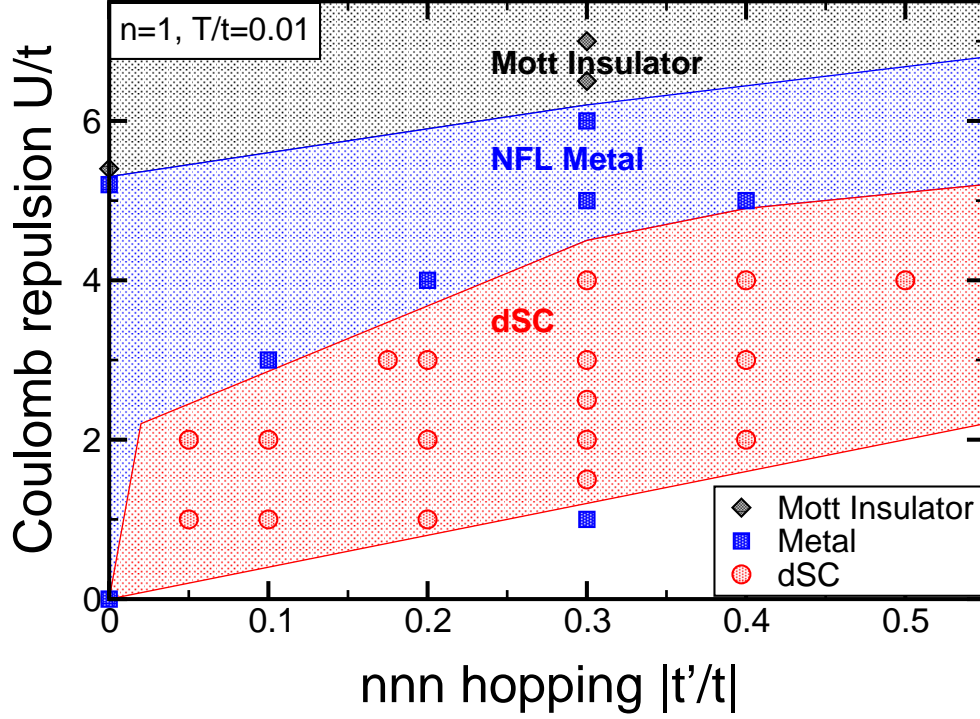


Figure 5.2: Phase diagram of the plaquette CDMFT approximation to the two-dimensional U - t - t' Hubbard model at half-filling and temperature $T = t/100$. d -wave superconductivity (dSC) is observed in a range of values of the local Coulomb interaction strength U which depends on the frustrating next-nearest neighbor hopping t' . Although the calculations are performed in the paramagnetic state, we observe that short-ranged antiferromagnetic correlations still suppress superconducting order for weak frustration, i.e., near $t' = 0$. The shaded regions and the corresponding phase boundaries are a guide to the eye.

the dSC phase turns out to emerge from a non-Fermi liquid (NFL) state upon cooling from higher temperatures, as will be detailed below. It is also an interesting observation that superconductivity is suppressed if the Coulomb repulsion becomes too strong, yet below the transition to the Mott insulator. In fact, within Hartree theory for the U - t - t' Hubbard model, it is found that on the square lattice the critical interaction strength for the onset of antiferromagnetism increases in a similar fashion as the phase boundary between the dSC and (NFL) metallic phases indicated in Fig. 5.2 [139]. This suggests that superconductivity is suppressed if short-ranged antiferromagnetic correlations, which are fully taken into account by the CDMFT method, become too strong.

For a non-zero $|t'/t| = 0.3$ we show in Fig. 5.3 the observed sequence of phases at $T = t/100$ as the interaction strength U is increased from zero to a value above the critical U for the Mott transition. The Mott transition is traced by studying, for example, the double occupancy, which continuously decreases upon an increase in U in the metallic phase and drops discontinuously at the first-order Mott transition. The dSC phase is studied by checking for an instability towards the establishment of a solution with a finite d -wave order parameter $\Delta = \frac{1}{2}|\Delta_{(\pi,0)} - \Delta_{(0,\pi)}|$ corresponding to $\Delta_{\mathbf{k}} = \Delta(\cos k_x - \cos k_y)$.

At weak coupling below $U/t = 1$ only a normal-conducting metallic state is observed, but the system might become superconducting upon further cooling, with a critical temperature which is exponentially small in the interaction strength. Whether this is in fact the case or whether there is a small window of U values in which the system does not become superconducting even at lower temperatures, however, was not resolved. For values of U/t between 1 and 5 we obtain a dSC solution at the given temperature. At larger U there is a transition to a non-Fermi liquid metallic phase (see below), and then undergoes the Mott transition at even larger U .

Also shown in Fig. 5.3 is the absolute value of the imaginary part of the self-

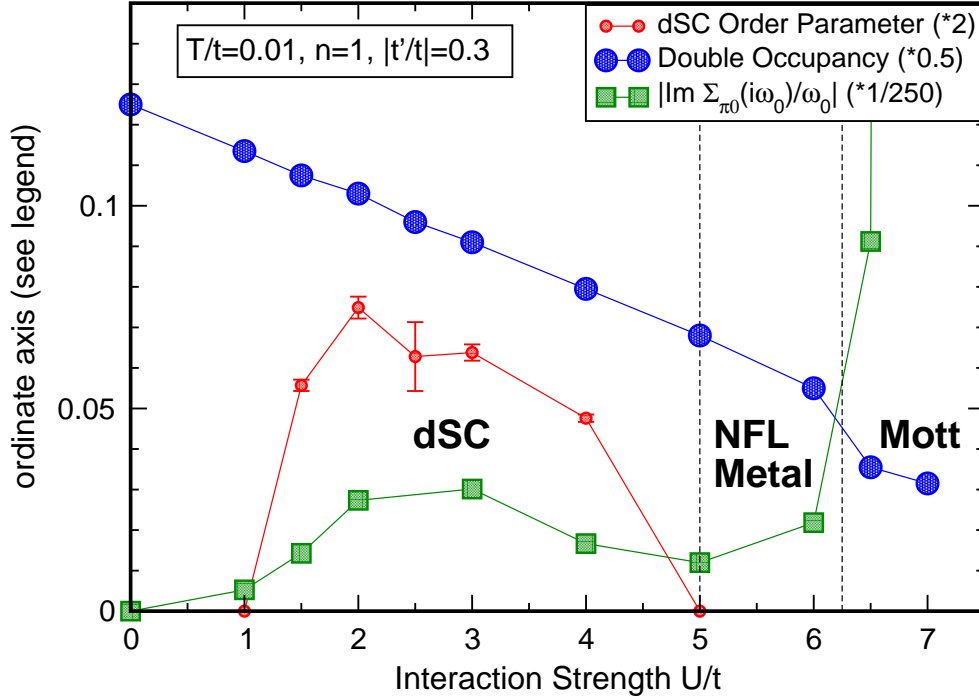


Figure 5.3: Sequence of phases (boundaries indicated by vertical dashed lines) upon increasing U/t for finite next-nearest neighbor hopping $|t'/t| = 0.3$ at half-filling and low temperature $T/t = 0.01$. At moderate U/t a d -wave superconducting (dSC) phase is obtained, as indicated by the finite dSC order parameter. The underlying metallic phase, obtained if dSC is suppressed, has non-trivial normal-state properties with a non-monotonic behavior as a function of U/t , as seen from the imaginary part of the self-energy at $(\pi, 0)$. Around $U/t = 5$ a transition to the metallic phase takes place. Also shown is the double occupancy, which decreases almost linearly in the metallic and superconducting phases, but shows a jump at the discontinuous transition to the Mott insulator above $U/t = 6$. In fact, at $T/t = 0.01$ a finite region in U/t is found where metallic and insulating solutions to the CDMFT equations exist. Here we show only the insulating solutions in the coexistence region. All quantities are rescaled as indicated in the legend to match the scale.

energy at the lowest Matsubara frequency $\omega_0 = \pi T$ divided by ω_0 for the accessible momentum closest to the Fermi surface, $\mathbf{k} = (\pi, 0)$, in the normal-conducting state. As expected the self-energy becomes very large in the Mott insulator. More surprisingly it shows a non-monotonic behavior at lower values of U , where it first increases before decreasing again towards $U = 0$. Interestingly the non-monotonicity of the self-energy in the normal-conducting phase is accompanied by a similar non-monotonic behavior of the dSC order parameter, immediately triggering the question whether there exists a relationship between non-Fermi liquid behavior and the establishment of superconductivity.

We now turn to the discussion of the properties of the normal-conducting state from which the dSC state emerges. In Ref. [127] a detailed study of $|\text{Im}\Sigma(\mathbf{k}, i\omega_0)/\omega_0|$ at the lowest Matsubara frequency $\omega_0 = \pi T$ for \mathbf{k} points near the Fermi surface in the $(0, 0)$ - $(\pi, 0)$ direction provided evidence for a crossover from non-Fermi liquid behavior near half-filling to a Fermi liquid upon doping in the more strongly coupled but unfrustrated system. With the momentum resolution given by the plaquette we can study the behavior of $|\text{Im}\Sigma((\pi, 0), i\omega_0)/\omega_0|$, which is not exactly on the Fermi surface for non-zero next-nearest neighbor hopping but still provides information about the existence of well-defined quasiparticles in the $(0, 0)$ - $(\pi, 0)$ direction and, if they exist, the quasiparticle weight $Z_{\mathbf{k}} = (1 - \partial \text{Re}\Sigma(\mathbf{k}, \omega)/\partial \omega|_{\omega \rightarrow 0})^{-1} \approx (1 - \text{Im}\Sigma(\mathbf{k}, i\omega_0)/\omega_0)^{-1}$, where the latter approximate equality is a good approximation in a Fermi liquid at low temperature. It is important to mention that $Z_{\mathbf{k}}$ is only well-defined (and takes values between 0 and 1) if the slope of $\text{Re}\Sigma(\mathbf{k}, \omega)$ as a function of ω at $\omega = 0$ is indeed negative. This corresponds to a self-energy with a continuous negative slope of $\text{Im}\Sigma(\mathbf{k}, z)$ for imaginary z at $z = 0$. If, for example, $\text{Im}\Sigma(\mathbf{k}, z)$ develops a sharp peak for certain \mathbf{k} values and at $z = 0$ such that both the slope of the real part along the real-frequency axis and the slope of the imaginary part on the imaginary-frequency axis become positive for very small frequencies, the $Z_{\mathbf{k}}$ factor is not a well-defined

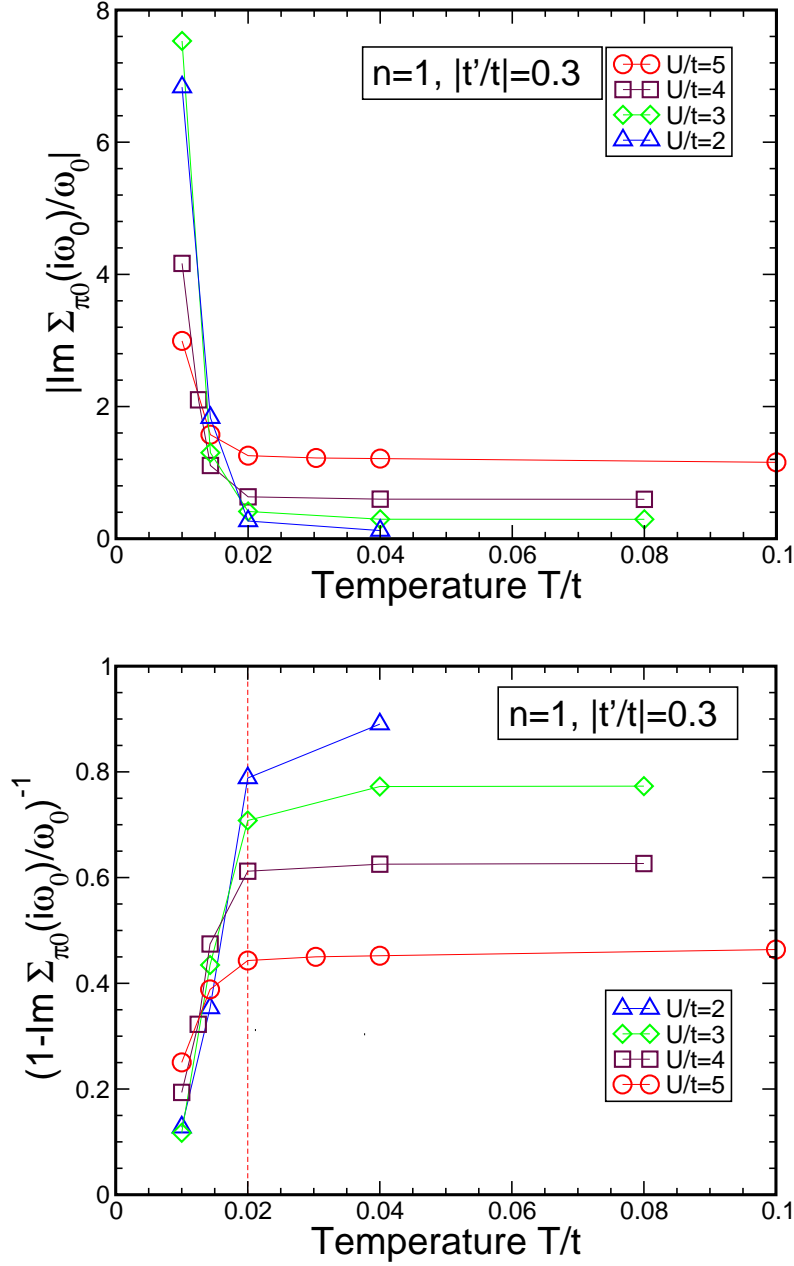


Figure 5.4: Upper diagram: Temperature dependence of $|\text{Im } \Sigma((\pi, 0), i\omega_0)/\omega_0|$ as a function of temperature for selected values of the interaction strength U at $|t'/t| = 0.3$ and for half-filling. Lower diagram: Temperature dependence of $(1 - \text{Im } \Sigma((\pi, 0), i\omega_0)/\omega_0)^{-1}$ for the same parameters. In a Fermi liquid this quantity converges to the quasiparticle weight $Z_{\mathbf{k}}$ ($\mathbf{k} = (\pi, 0)$) in the zero-temperature limit. The vertical dashed line indicates the temperature below which the Fermi-liquid description breaks down (also see Fig. 5.5).

quantity and Fermi-liquid theory breaks down.

In the upper diagram of Fig. 5.4 the T dependence of $|\text{Im}\Sigma((\pi, 0), i\omega_0)/\omega_0|$ is shown for the same parameter values as in Fig. 5.3 and for selected values of the interaction strength. While at high temperatures $|\text{Im}\Sigma((\pi, 0), i\omega_0)/\omega_0|$ shows only a weak T dependence, it increases upon cooling for temperatures below $T/t \approx 0.02$, which is above the superconducting critical temperatures observed for all U values. In fact, at high temperatures the self-energy is larger for larger U , as expected, but at lower temperatures there is a non-monotonic behavior of the self-energy at $(\pi, 0)$ as a function of U , as also seen in Fig. 5.3. In the lower diagram of Fig. 5.4 the $Z_{\mathbf{k}}$ factor for $\mathbf{k} = (\pi, 0)$, as calculated from $(1 - \text{Im}\Sigma(\mathbf{k}, i\omega_0)/\omega_0)^{-1}$, is shown as a function of temperature. A strong suppression of the “quasiparticle weight” $(1 - \text{Im}\Sigma(\mathbf{k}, i\omega_0)/\omega_0)^{-1}$ at $\mathbf{k} = (\pi, 0)$ upon cooling is observed, but we stress that the concept of the quasiparticle weight itself breaks down for the lowest temperatures below $T/t = 0.02$, indicated by the dashed vertical line in the lower diagram of Fig. 5.4, as we will now discuss in detail.

In order to demonstrate the deviation of the self-energy at $(\pi, 0)$ from Fermi-liquid behavior for the relevant interaction strength values $U/t = 3$ and 4 , where the system becomes superconducting slightly above $T/t = 0.01$, we extract the slope of the imaginary part of the self-energy from its values at the two lowest Matsubara frequencies. The results are shown in Fig. 5.5. While the slope is negative at high temperatures it changes sign below $T/t = 0.02$ for both $U/t = 3$ and $U/t = 4$, indicating a non-Fermi liquid (NFL) behavior at low temperatures. Intriguingly, since the d -wave superconducting phase appears at even lower temperatures than the deviation from Fermi-liquid behavior, superconductivity thus emerges from an unconventional metallic phase with a non-Fermi liquid self-energy at the $(\pi, 0)$ point.

To summarize our findings for the half-filled system, there are at least two critical values of the interaction strength at low temperatures, namely a lower one (slightly

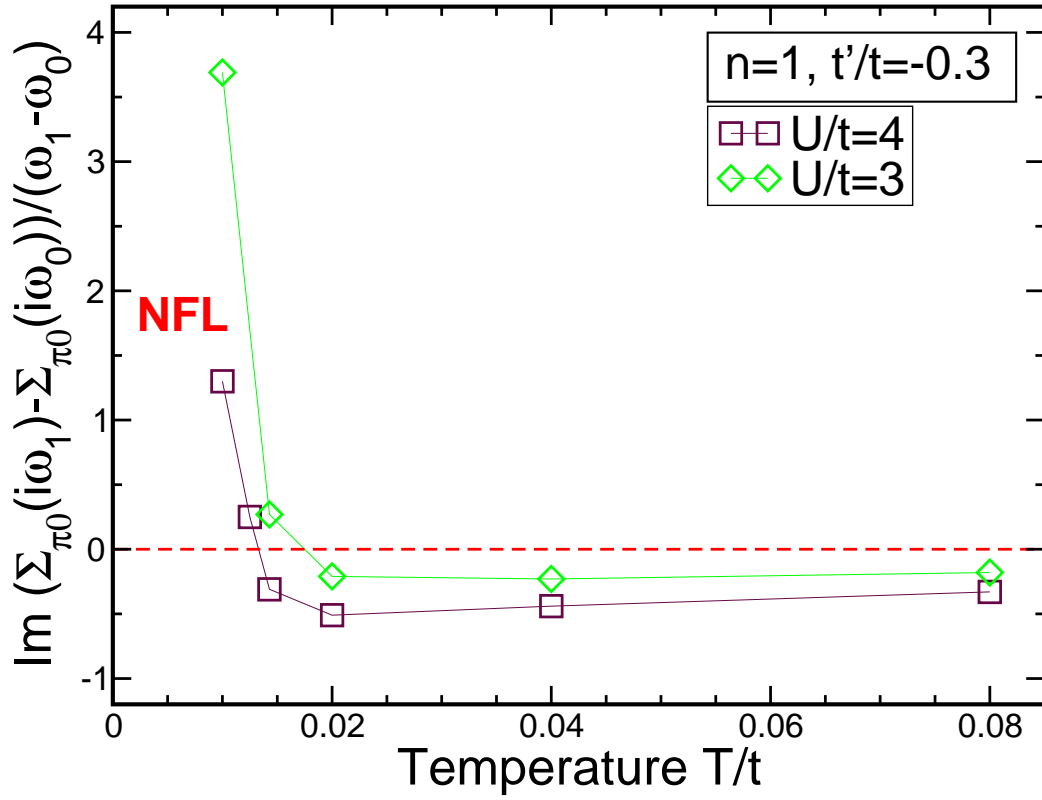


Figure 5.5: Slope of the real part of the self-energy, estimated from the slope of $\text{Im}\Sigma$ at $(\pi, 0)$ on the Matsubara axis, at selected values of the interaction strength in the regime in which the system has a superconducting instability as a function of temperature for $t'/t = -0.3$ and half-filling. Below $T/t = 0.02$ a sign change in the slope is observed, signaling a breakdown of the Fermi-liquid picture in the region around $(\pi, 0)$ in the Brillouin zone.

below $U/t = 5$ for $T/t = 0.01$ and $|t'/t| = 0.3$) for the transition from a d -wave superconducting phase, which emerges from an unconventional metallic phase upon cooling, to a metallic phase with non-Fermi liquid properties around $(\pi, 0)$, and an upper critical interaction strength for the well-known first-order Mott transition (slightly above $U/t = 6$ for the selected parameter values). The non-Fermi liquid phase is characterized by a sign change in the slope of the real part of the self-energy at low frequencies (and low temperatures) around the $(\pi, 0)$ point, which indicates that the concept of low-energy quasiparticles breaks down in the $(\pi, 0)$ region of the Brillouin zone. At the same time, a pseudogap is expected to appear in the \mathbf{k} -resolved spectral function

$$A(\mathbf{k}, \omega) = -\frac{1}{\pi} \frac{\text{Im } \Sigma(\mathbf{k}, \omega)}{(\omega - \epsilon_{\mathbf{k}} - \text{Re } \Sigma(\mathbf{k}, \omega))^2 + (\text{Im } \Sigma(\mathbf{k}, \omega))^2} \quad (5.11)$$

near the $(\pi, 0)$ point in the frequency regime where the imaginary part of the self-energy is enhanced. Therefore the physics of the frustrated two-dimensional Hubbard model at weak coupling and half-filling indeed bears some resemblance with the physics in the strong coupling regime at finite doping [140], where a superconducting phase emerges from a pseudogap phase close to half-filling below optimal doping. At weak coupling, however, the enhancement of the imaginary part of the self-energy is restricted to a narrow frequency region. This observation is in agreement with results from functional renormalization group calculations [129, 130], where similar features in the self-energy at weak coupling and finite t' were identified as the origin of a pseudogap in the spectral function. However, while the weak-coupling pseudogap is restricted to a very narrow frequency range, the strong-coupling pseudogap is more pronounced and develops into a full gap in the Mott insulator at half-filling. In fact, a momentum-selective metal-insulator transition was obtained as a function of hole doping within an eight-site dynamical cluster approximation [138]. For eight-site clusters the momentum resolution allows access to the $(\pi/2, \pi/2)$ point (the nodal direction) in addition to the $(\pi, 0)$ point (antinodal direction), and finite-size effects

leading to an overestimation of correlations are less pronounced. It was shown that a two-stage transition takes place. For large hole doping the system is a Fermi liquid. Upon approaching half-filling a pseudogap first appears in the momentum sector containing the antinodal region, while the states in the nodal region remain gapless until half-filling. Therefore the NFL-FL crossover was identified as the doping level where the antinodal region becomes gapped.

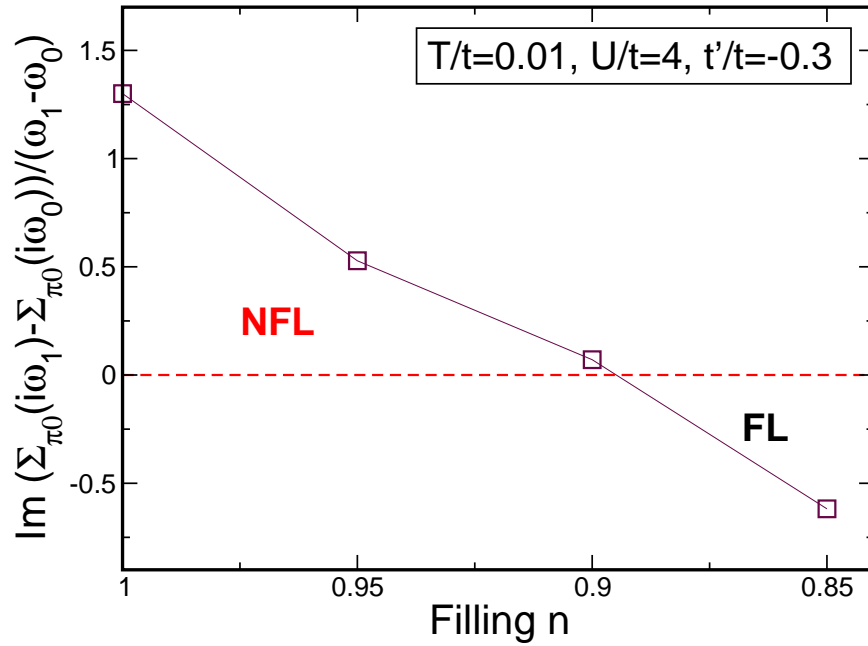


Figure 5.6: Slope of the real part of the self-energy, estimated from the slope of $\text{Im}\Sigma$ on the Matsubara axis, as a function of filling upon hole-doping for $U/t = 4$, $t'/t = -0.3$ and $T/t = 0.01$. Around 10 percent hole doping a crossover from a non-Fermi liquid with positive slope to a Fermi liquid with negative slope takes place.

To make contact with strong-coupling results we follow the $U/t = 4$ solution at $t'/t = -0.3$ and $T/t = 0.01$ as a function of hole doping. In Fig. 5.6 the slope of $\text{Im}\Sigma((\pi, 0), z)$, for z on the imaginary-frequency axis, extracted from the lowest two Matsubara frequencies is shown. Indeed, starting from a positive slope at half-filling

indicating NFL behavior the slope continuously decreases and changes sign around 10 percent hole doping, where thus an NFL-FL crossover takes place.

In Fig. 5.7 we visualize the results obtained in this work for the weak-coupling scenario and present a generalized view by including results for the strongly coupled system away from half-filling [138, 127, 140]. A non-zero next-nearest neighbor hopping frustrates the weak-coupling antiferromagnetic instability [139] and thus opens up a window of interaction strengths where superconductivity may exist even at half-filling. A NFL phase, possibly due to short-ranged antiferromagnetic correlations, is found to exist around half-filling, and it is this NFL phase from which the dSC phase emerges upon cooling, even at weak coupling. The Fermi-liquid metal is recovered upon doping. Similarly there is a dSC phase at strong coupling, which also emerges from a NFL phase in the underdoped region. Although the strong-coupling pseudogap appears at much larger energy (and consequently temperature) scales it is an interesting question how the NFL phases at weak and strong coupling are related. Moreover, in both cases dSC appears as an instability in a strange metallic phase with a partially depleted Fermi surface and the absence of quasiparticles in certain \mathbf{k} directions, which seems to contradict the well-known BCS picture [61], in which well-defined quasiparticles are paired. However, in the ordered phase the anomalous expectation value $\langle c_{\mathbf{k}\uparrow}^\dagger c_{-\mathbf{k}\downarrow}^\dagger \rangle \neq 0$ is a well-defined quantity anyway. Thus the ordered state is in fact less unusual than the underlying normal-conducting state, a fact which is also reminiscent of the pseudogap phase in the cuprates [64].

5.5 Conclusion

To summarize, a d -wave superconducting (dSC) phase is observed in the plaquette CDMFT approximation to the weakly coupled frustrated two-dimensional Hubbard model at half-filling. Remarkably, superconductivity emerges upon cooling from a

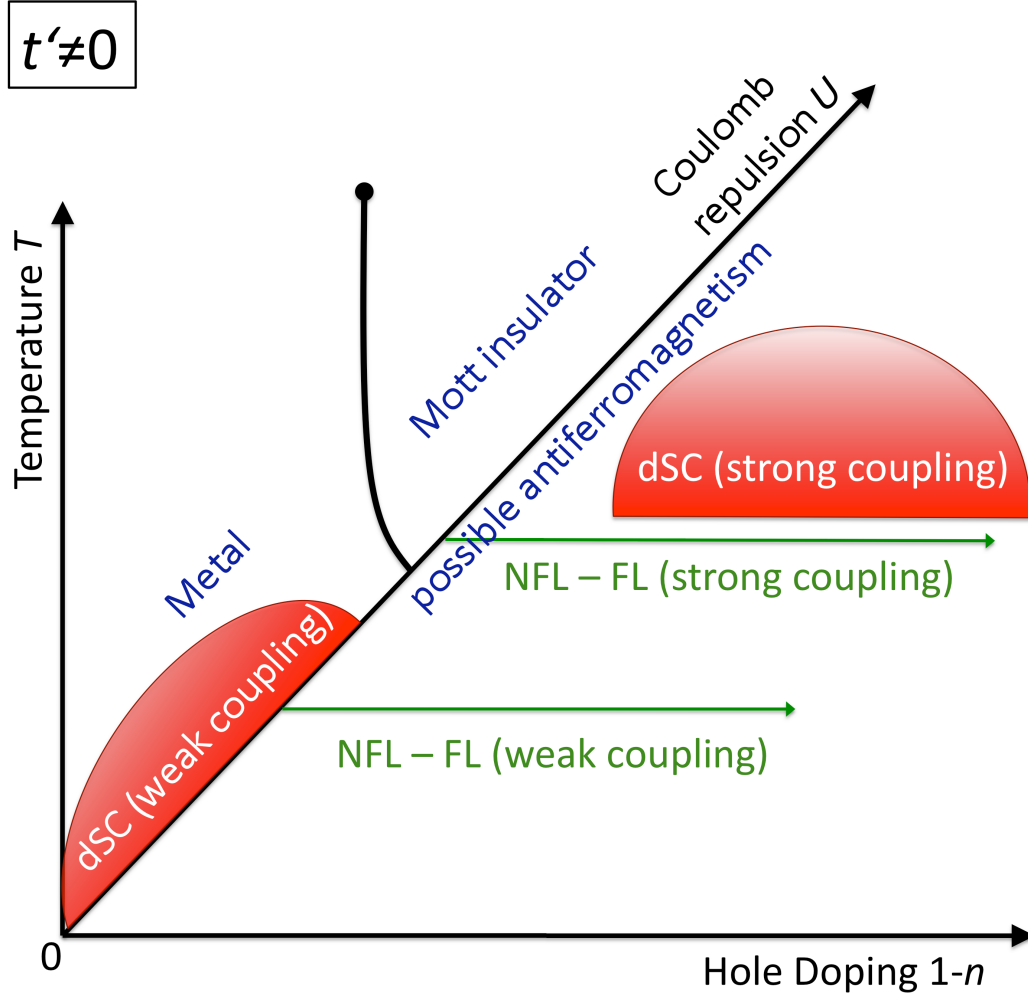


Figure 5.7: Sketch of phases in the two-dimensional frustrated Hubbard model in the space of temperature T , doping $1 - n$ and Coulomb repulsion U . Results are shown for d -wave superconductivity (dSC) and the non-Fermi liquid (NFL) to Fermi-liquid (FL) transitions upon doping at weak and strong coupling in the presence of frustration, $t' \neq 0$, where a finite weak-coupling window for dSC opens in which antiferromagnetism is suppressed [139]. The sketch is based upon results obtained in this work and, e.g., in Refs. [138, 127, 140]. Note that away from half-filling, and in particular at strong coupling, a tendency towards phase separation is observed [140, 131]. It is an interesting open question whether and how the dSC phases and the transitions from NFL to FL physics at weak and strong coupling are related.

non-Fermi liquid (NFL) metal with a narrow peak in the imaginary part of the self-energy around the $(\pi, 0)$ point, in an interesting analogy with the strong coupling pseudogap and superconductivity phenomena away from half-filling. This unusual behavior of the self-energy indicates that, even at relatively weak coupling, non-local correlations in combination with low dimensionality may violate the quasiparticle concept in certain directions in momentum space. Such preconditions lead to enhanced damping of quasiparticles, especially at low temperatures and close to the Fermi surface. This is in marked contrast to Fermi-liquid theory, where quasiparticles are long-lived and in fact have an infinite lifetime on the Fermi surface at zero temperature. Naturally, the observed NFL effects at weak coupling are expected to be particularly strong in the proximity of van-Hove singularities in the non-interacting density of states, since enhanced phase space for low-energy scattering processes is present in the respective momentum space regions. The precise nature of the scattering processes leading to NFL behavior, however, remains to be explored. In contrast, at strong coupling it was shown that the opening of a pseudogap was not related to van-Hove features in the density of states [138]. We also note that the plaquette geometry used in our study typically overestimates correlation effects. Therefore the observed non-Fermi liquid features are expected to be weaker for larger clusters. Away from half-filling a crossover from a NFL to the more conventional Fermi-liquid metallic phase upon doping is observed at weak coupling. It is an intriguing open question how the dSC and NFL phases at weak coupling and half-filling are connected to their counterparts at strong coupling and finite doping.

Chapter 6

Charge and Spin Criticality at the Mott Transition in a Two-Dimensional Organic Conductor

6.1 Abstract

We study the behavior of the charge and spin degrees of freedom at the critical end point of the bandwidth-controlled Mott transition in a two-dimensional Hubbard model with anisotropic next-nearest neighbor hopping which is relevant to layered organic conductors. Using cluster dynamical mean-field theory on a plaquette and a continuous-time quantum Monte Carlo impurity solver, we obtain critical exponents for the single-particle density of states at the Fermi energy (charge criticality) and the nuclear spin-lattice relaxation rate divided by temperature (spin criticality). Both charge and spin degrees of freedom are observed to show critical behavior with a divergent slope at the critical end point, and the extracted critical exponents are remarkably consistent with experimental data.

6.2 Introduction

The Mott metal-insulator transition is a paradigmatic example of a correlation-induced phase transition, and the single-band Hubbard model is the generic theoret-

ical model in which it occurs. Its model parameters are the local Coulomb repulsion U , the bare bandwidth W and the average electronic density per lattice site (filling) n . One distinguishes the bandwidth-controlled Mott transition, where at a fixed filling the Mott-insulating system is driven metallic by increasing W/U , typically through chemical or hydrostatic pressure, and the filling-controlled Mott transition, which takes place when at large enough U/W the half-filled system is doped with electrons or holes. In many cases the paramagnetic Mott transition is hidden by an ordered phase, e.g., antiferromagnetism. However, in sufficiently frustrated systems and at high enough temperatures the bandwidth-controlled transition from a paramagnetic metal to a paramagnetic Mott insulator can be observed in experiments.

A prominent example for the observation of the bandwidth-controlled Mott transition is the quasi-two-dimensional κ -(ET)₂Cu[N(CN)₂]Cl (abbreviated as κ -Cl), which belongs to a whole class of layered organic charge transfer salts (see Fig. 6.1) [142, 58, 141]. Since these materials are both low-dimensional and frustrated, such that magnetic order is suppressed at elevated temperatures, one can follow the first-order Mott transition to its second-order critical end point in the absence of long-range order. Of special interest is the critical behavior, or Mott criticality, at the critical point. Experimentally the criticality is probed by the behavior of observables (e.g., the conductivity σ) as a function of external parameters (temperature T , pressure P) in the vicinity of the critical point. One observes scaling of the deviation $\Delta\sigma(t_{\text{red}}, p_{\text{red}}) = \sigma(t_{\text{red}}, p_{\text{red}} = 0) - \sigma_c$ with the reduced parameters $t_{\text{red}} = (T - T_c)/T_c$ and $p_{\text{red}} = (P - P_c)/P_c$, where the index c denotes the respective values at the critical point. Criticality is then classified by the exponents (β, γ, δ) defined via

$$\begin{aligned} \Delta\sigma(t_{\text{red}}, p_{\text{red}} = 0) &\propto |t_{\text{red}}|^\beta, \\ \left. \frac{\partial\sigma(t_{\text{red}}, p_{\text{red}})}{\partial p_{\text{red}}} \right|_{p_{\text{red}}=0} &\propto |t_{\text{red}}|^{-\gamma}, \\ \Delta\sigma(t_{\text{red}} = 0, p_{\text{red}}) &\propto |p_{\text{red}}|^{1/\delta}, \end{aligned} \tag{6.1}$$

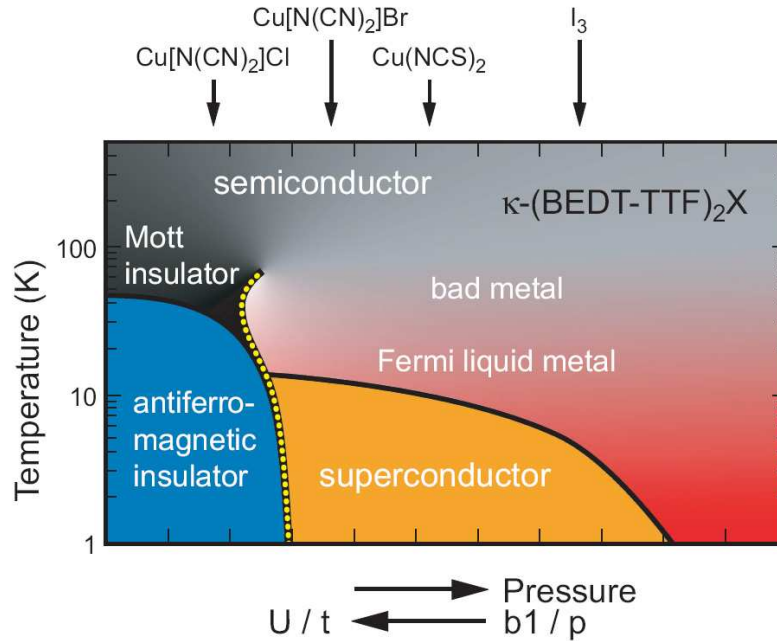


Figure 6.1: Schematic phase diagram of the family of two-dimensional organic conductors, with an insulating phase ordered antiferromagnetically at low pressure (small t/U) and a superconducting phase at higher pressure (large t/U). The critical end point of the Mott transition is located above the ordering temperatures of both superconductivity and antiferromagnetism. Note that κ -Cl is an insulator at ambient pressure. Hence the paramagnetic Mott transition can be studied in this material by applying hydrostatic pressure. It is, from the point of view of this thesis, unclear how the label “Fermi-liquid metal” is determined experimentally and whether it is justified (see Chapter 5). From Ref. [141].

which obey the scaling law $\gamma = \delta (\beta - 1)$.

It is suggestive to propose that the Mott transition is in the Ising universality class [143, 144, 145, 146], based on the argument that the double occupancy may be interpreted as an “order parameter”. Since the double occupancy is a scalar field, Ising universality would apply in this case. However, while conductivity measurements for the three-dimensional $(V_{1-x}Cr_x)_2O_3$ indeed confirm critical behavior compatible with 3D Ising universality [147], the situation seems to be less clear-cut for the two-

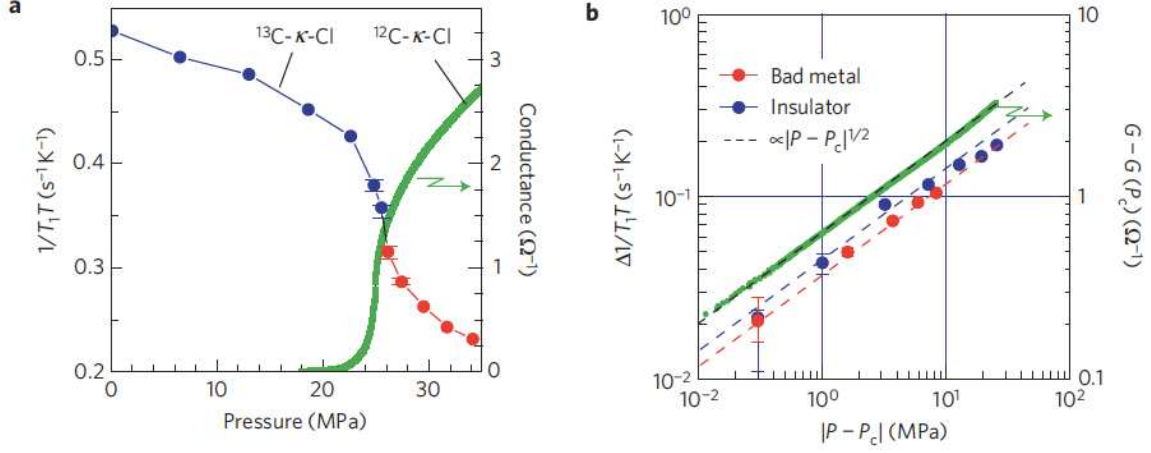


Figure 6.2: Nuclear spin-lattice relaxation rate divided by temperature, $1/T_1 T$, and conductance at the critical end point of the Mott transition in $\kappa\text{-Cl}$. From Ref. [59].

dimensional $\kappa\text{-Cl}$.

For quasi-two-dimensional systems the critical exponents of the 2D Ising model are $\beta = 1/8$, $\gamma = 7/4$, and $\delta = 15$ [148]. Conductivity measurements under pressure performed on $\kappa\text{-Cl}$ challenge this prediction, with the observed exponents $\beta \approx 1$, $\gamma \approx 1$, and $\delta \approx 2$. While it is argued by Imada *et al.* [149,53] that the observed deviation from Ising universality is a manifestation of unconventional quantum criticality due to momentum-space differentiation near the topological Mott transition specific to a two-dimensional system, a different scenario was proposed by Papanikolaou *et al.* [146] who pointed out that the conductivity can have a different critical behavior than the order parameter of the transition. The authors argued that when the coupling of the conductivity to the energy density of the Ising model dominates, one may obtain an extended regime around the critical point with modified critical exponents, $\beta = 1$, $\gamma = 7/8$, and $\delta = 15/8$, in fair agreement with the exponents observed in $\kappa\text{-Cl}$. Thermal expansion measurements on a related material [150] were explained by a scaling theory for the two-dimensional Ising universality class, thus supporting the

latter point of view [151].

Recently a new flavor was added to the picture by a study of the Mott criticality of the spin degree of freedom. Kagawa *et al.* performed extensive NMR experiments under pressure and found that the critical enhancement of the conductivity when going through the critical end point is accompanied by a critical suppression of spin fluctuations, as evidenced by a decrease of the nuclear spin-lattice relaxation rate divided by temperature, $1/T_1T$ (see Fig. 6.2) [59]. Interestingly the critical exponents δ of charge (conductivity) and spin ($1/T_1T$) are found to be equal ($\delta \approx 2$) within experimental accuracy.

6.3 Model and Methods

We aim at a microscopic description of the Mott criticality in organic conductors by studying the two-dimensional one-band Hubbard model on an anisotropic triangular lattice with the Hamiltonian

$$H = \sum_{\mathbf{k}, \sigma} \epsilon_{\mathbf{k}} c_{\mathbf{k}, \sigma}^\dagger c_{\mathbf{k}, \sigma} + U \sum_i n_{i, \uparrow} n_{i, \downarrow}, \quad (6.2)$$

where $c_{\mathbf{k}, \sigma}^\dagger$ ($c_{\mathbf{k}, \sigma}$) creates (annihilates) an electron in a Bloch state with lattice momentum \mathbf{k} , $n_{i, \sigma}$ is the local density operator for site i and spin $\sigma = \uparrow, \downarrow$, $U > 0$ is the local Coulomb repulsion strength and the electronic dispersion is given by

$$\epsilon_{\mathbf{k}} = -2t (\cos k_x + \cos k_y) - 2t_{\text{diag}} \cos(k_x + k_y). \quad (6.3)$$

According to Ref. [152] we choose for the relevant κ -Cl material a diagonal hopping $t_{\text{diag}} = 0.44t$ and fix the filling at $n = 1$. Therefore the variable parameters are the onsite Coulomb repulsion U and the temperature T . To solve the problem we choose the cluster dynamical mean-field theory (CDMFT) [136, 41] on a plaquette (see Fig. 6.3), where the full lattice model is mapped to a 2×2 cluster impurity

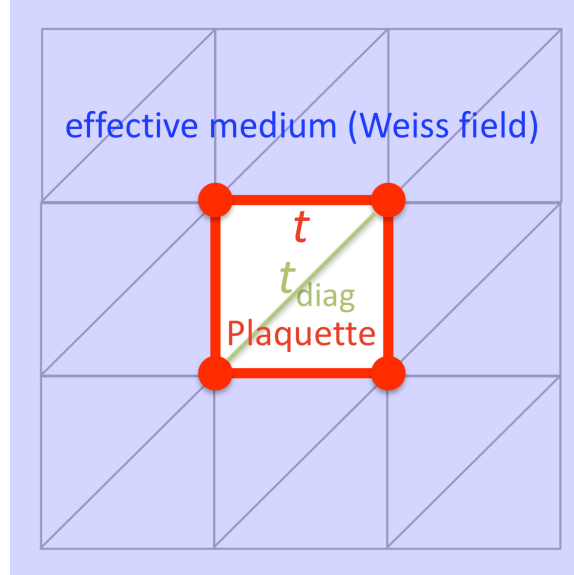


Figure 6.3: U - t - t_{diag} Hubbard model on the two-dimensional square lattice with nearest neighbor hopping t and anisotropic next-nearest neighbor hopping t_{diag} . Within plaquette CDMFT a plaquette impurity is singled out, and the rest of the lattice is replaced by an effective medium which is determined self-consistently.

model embedded in a self-consistently determined dynamical mean field. The cluster impurity problem is solved using a continuous-time Quantum Monte Carlo method based on the hybridization expansion [85]. In its single-site version DMFT is by now a well-established, reliable and powerful method to study phase transitions in strongly correlated materials, most notably the Mott transition in infinite dimensions. The generalization to clusters is necessary in order to capture also non-local dynamical correlation effects, which are of crucial importance in low-dimensional systems. In particular CDMFT has been used to study the phase diagram of two-dimensional organic conductors [153, 154].

The charge criticality is extracted from an estimate of the interacting density of states at the Fermi level via the imaginary-time Green function, $A(\omega = 0) \approx \beta G(\beta/2)$ ($\beta = 1/T$), which has proven an approximate but reliable way of obtaining detailed

information on the finite-temperature Mott transition [138]. The spin criticality is more difficult to study in theory. First of all, an approximate relation needs to be assumed, namely the one between the local spin susceptibility $\chi(\omega)$ and the spin-lattice relaxation rate $1/T_1$, $1/T_1 T \approx \lim_{\omega \rightarrow 0} \text{Im}\chi(\omega)/\omega$, where a form factor is omitted. Secondly, the spin susceptibility on the real-frequency axis needs to be calculated from the spin-spin correlation function on the imaginary-time domain, i.e., by an analytical continuation procedure, for which we employ the Maximum Entropy Method [39].

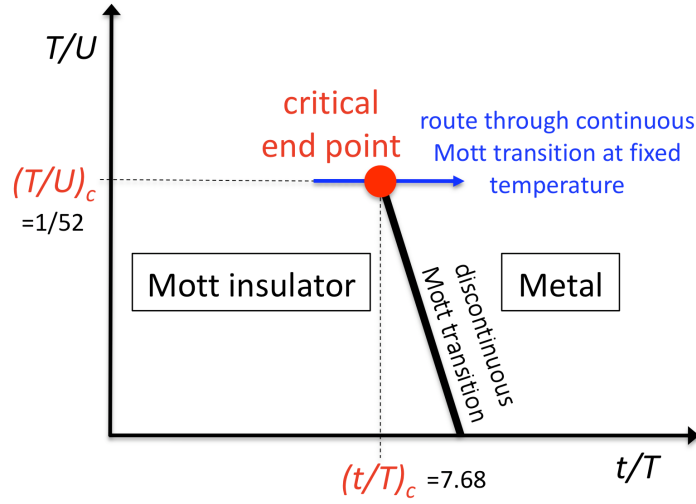


Figure 6.4: Route through the continuous Mott transition at fixed temperature. We assume that the pressure-controlled transition in Ref. [59] corresponds approximately to the bandwidth-controlled transition in theory. Therefore the hopping amplitude t (bandwidth $W \propto t$) is varied (blue arrow) while the local Coulomb repulsion U , the relative anisotropic diagonal hopping t_{diag}/t and the temperature T are kept fixed in our calculations. The indicated values of $(T/U)_c$ and $(t/T)_c$ are the critical values found for $t_{\text{diag}}/t = 0.44$ as used in this study.

Before presenting our results we note here that a theoretical description of the Mott criticality using these methods involves an important approximation. The single-band Hubbard model is used as an effective low-energy model of $\kappa\text{-Cl}$ [152],

and in particular the pressure-controlled Mott transition in the experiment is identified with the bandwidth-controlled Mott transition in theory. The latter assumption means that when in the experiment the temperature is kept fixed and pressure is applied, in our theory we keep the temperature T , Coulomb repulsion U and also the ratio t_{diag}/t fixed and change the size of the hopping matrix element t , assuming that in a given range of pressure near the critical end point of the Mott transition a linear increase in pressure amounts to a linear increase in t (see Fig. 6.4).

6.4 Results and Discussion

We now turn to the discussion of the critical behavior near the critical end point of the Mott transition. Using the discontinuity of the double occupancy as a function of U below the critical temperature T_c and its continuous decrease upon increasing U above T_c as a guide to identify the critical end point, we find $(U/T)_c = 52$. Fixing $U/T = (U/T)_c$ we study the critical exponent δ of the critical observable σ as a function of the variable t/T (see Eq. (6.1) and Fig. 6.4), where increasing t/T is assumed to amount to increasing pressure as discussed above. Here σ is chosen to be $G(\beta/2)$ (charge criticality) and $\lim_{\omega \rightarrow 0} \text{Im}\chi(\omega)/\omega$ (spin criticality). The analytic continuation of the spin susceptibility data on the insulating side of the transition turns out to be difficult due to the formation of local moments. Therefore the spin-spin correlation function on the imaginary-time axis becomes rather flat in the Mott insulator, which corresponds to a sharp peak in $\text{Im}\chi(\omega)/\omega$ at $\omega = 0$. Hence we restrict ourselves to the behavior of the spin criticality on the metallic side of the transition.

The results are shown in Fig. 6.5. Both charge and spin degrees of freedom show critical behavior with a maximal (infinite) slope at the continuous transition, which is identified at $(t/T)_c = 7.68$, independently for charge and spin. We first discuss the qualitative resemblance of the theoretical results and the experimental data. The

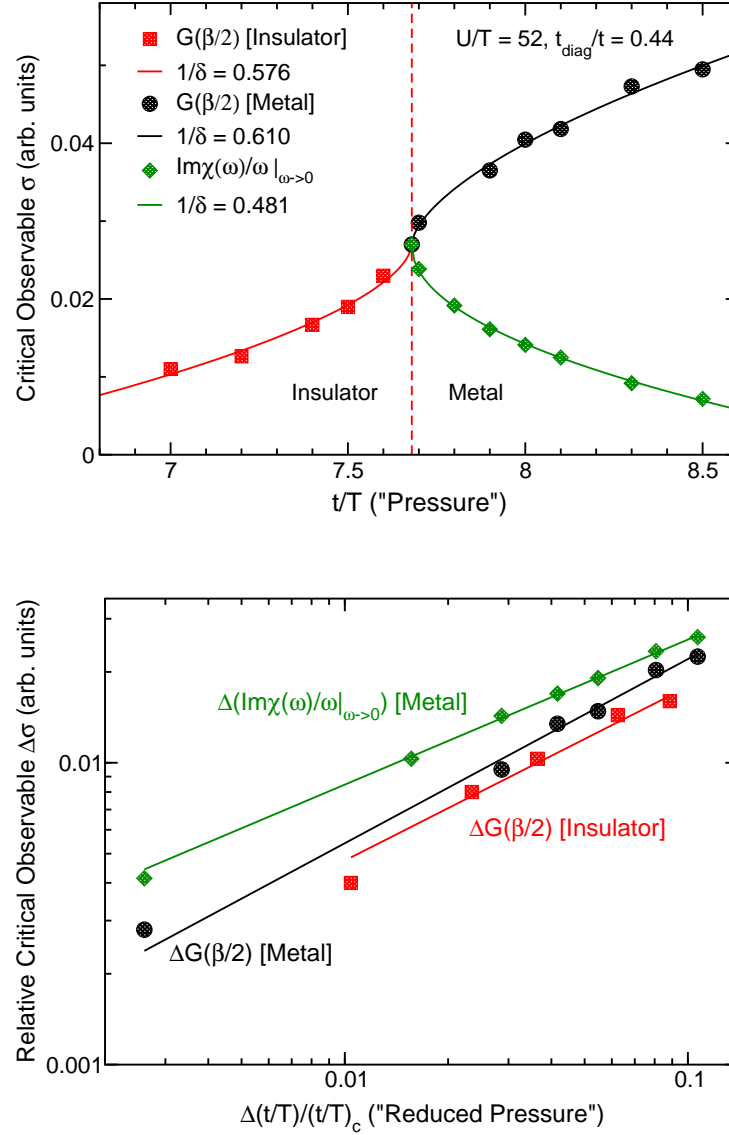


Figure 6.5: Critical behavior at the continuous bandwidth-controlled Mott transition (vertical dashed line, $(T/t)_c = 7.68$). Upper diagram: Evolution of critical observables $G(\beta/2)$ and $\lim_{\omega \rightarrow 0} \text{Im} \chi(\omega)/\omega$ (rescaled to match the value of $G(\beta/2)$ at the critical point) upon increasing t/T . The solid curves are fits to the critical scaling behavior according to Eq. (6.1). Lower diagram: Double-logarithmic plot of the same data as in the upper diagram, measured from the critical end point of the Mott transition. Solid lines show the critical scaling (same fits as in upper diagram).

increase of $G(\beta/2)$ indicates that the low-energy spectral weight increases upon going from the insulator to the metal. In fact, this behavior reflects the filling of the charge gap in the Mott insulator with low-energy states and the development of the Fermi surface at the insulator-metal transition. Thus the charge degrees of freedom, which are localized in the insulator, become delocalized in the metal, as expected. Similarly, the measured conductance (Fig. 6.2) increases in the metal. In contrast, the spin susceptibility shows the opposite behavior. It is suppressed in the metal and enhanced in the insulator, as seen both in Fig. 6.5 and the measured $1/T_1T$ from NMR (Fig. 6.2). The enhancement of spin excitations in the insulator is traced to the predominant occupation of the plaquette with a four-electron singlet state with zero total momentum and zero total spin $S = 0$ (see Fig. 6.6). The second-most probable states (not shown) are three triplet states with spin $S = 1$. Since the singlet state has such a high occupation probability in the insulator, spin flip ($\Delta S = 1$) excitations to the triplet states are more likely, which leads to the large susceptibility in the insulator.

Even a quantitative comparison with the cited experiments is possible, as can be seen in the lower diagram of Fig. 6.5. Indeed the double-logarithmic plot of the observables relative to their values at the critical point as a function of the reduced variable is in good agreement with the scaling relation, Eq. (6.1). From linear fits to the double-logarithmic plot we extract the critical exponents. For the charge criticality exponents $1/\delta = 0.576$ (on the insulating side of the transition) and $1/\delta = 0.610$ (metallic side) are found. The observation of critical behavior with an infinite slope of the density of states at the Fermi energy, extracted from $G(\beta/2)$, at the transition is in agreement with the behavior of the measured conductivity, and also the critical exponents ($1/\delta \approx 0.5$ for the conductivity [58]) are in fair agreement. A quantitative comparison, however, is of course difficult, since the explicit relation of the exponents for the density of states and for the conductivity is unclear. For the

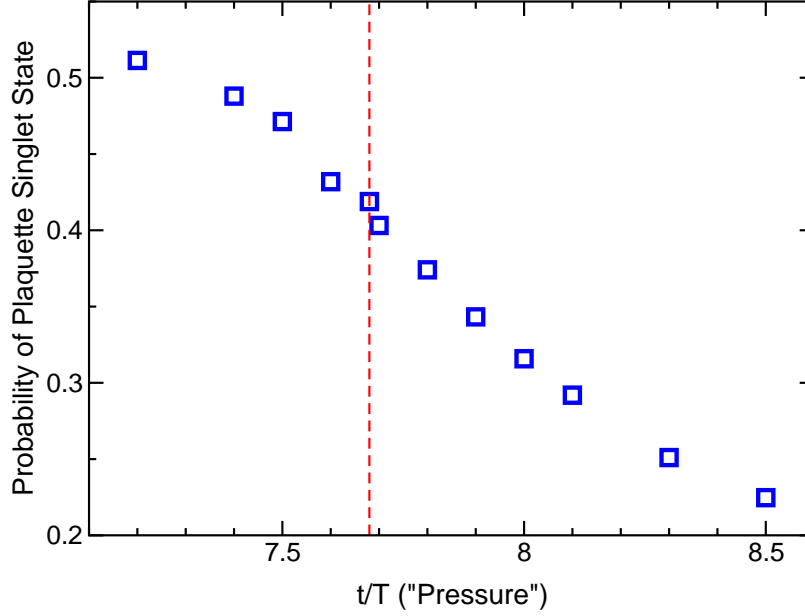


Figure 6.6: Probability of the plaquette singlet state as a function of t/T for the same parameters as in Fig. 6.5, as extracted from the sector occupation statistics measured in CTQMC [137, 48, 50]. The plaquette is predominantly occupied by this singlet state in the insulator (left side of the vertical dashed line). With increasing pressure the probability of the singlet state decreases, leading to a suppression of the spin susceptibility in the metal.

spin criticality, however, even quantitative agreement with experiment is found, with an exponent 0.481 very close to the experimentally determined $1/\delta \approx 0.5$ [59].

6.5 Summary

To summarize, we have studied the critical behavior of charge and spin at the Mott transition in the two-dimensional anisotropic Hubbard model relevant to the organic charge transfer salt κ -Cl using plaquette cluster DMFT. The charge criticality was obtained using an estimate of the density of states at the Fermi energy directly from imaginary-time QMC data, while the spin criticality was extracted from an analytic

continuation of the spin-spin correlation function to obtain a direct estimate of the NMR data $1/T_1T$. In qualitative agreement with experimental observations, the density of states is enhanced when passing through the critical end point of the Mott transition from the insulator to the metal, with an infinite slope at the transition. Interestingly, the critical exponents for the theoretically evaluated density of states and for the measured conductivity are quite close to each other.¹ Even more remarkably, we find quantitative agreement with the experiment for the spin criticality. The spin susceptibility is suppressed upon an increase in bandwidth, and we find a critical exponent $1/\delta \approx 0.5$ for $1/T_1T$. Our results do not resolve the issue of whether a quantum-critical scenario with unconventional exponents [149,53] or a classical scenario with modified exponents [146] is the appropriate framework for the description of the Mott critical end point in two-dimensional quantum systems. However, we have shown that results consistent with experiments (and with both theoretical scenarios) can be obtained from a single-band Hubbard model in the plaquette dynamical mean field approximation solved with a continuous-time quantum Monte Carlo method, and in particular under the assumption that a linear change in pressure close to the transition can be modeled by a linear change in bandwidth.

¹Note that there is a linear relation between the density of states at the Fermi level and the dc conductivity for a metal within the relaxation-time approximation in Boltzmann theory. However, whether a similar relation holds in the correlated system close to the Mott transition and especially in the Mott insulator is far from clear.

Chapter 7

DC Conductivity of Disordered Graphene

7.1 Abstract

Two of the hallmark features of graphene are its linear quasiparticle dispersion and the finite minimum conductivity [155]. In non-suspended graphene (NSG) the minimum conductivity σ_{\min} , i.e., the minimal value of the dc conductivity σ_{dc} with respect to density variations, is weakly dependent on temperature T but varies considerably from sample to sample [155, 156]. In order to push graphene's transport properties to the ballistic limit of Dirac fermions without scattering, realizations of suspended graphene (SG) sheets have been prepared, allowing for unprecedented electron mobilities [157, 158, 159] and showing a stronger increase σ_{\min} upon increasing T [160, 161]. At finite densities σ_{dc} decreases with T below a crossover temperature, and the resistivity increases linearly with T at high densities. Here we show that the observed range of σ_{\min} values is compatible with disorder potentials on the order of meV. Moreover, the temperature dependence of the resistivity at high densities and the density dependence of the respective slopes are consistently explained by a temperature-dependent disorder strength Γ , which consists of a constant Γ_0 and a contribution $\alpha_1 T$. This finding suggests that at least two contributions to scattering in graphene are important for its transport properties, and that one of the contributions is due to scattering of electrons from thermally induced excitations.

7.2 Introduction

Free electrons on the half-filled honeycomb lattice constitute a perfect conductor with a non-zero Drude weight at finite temperature and a finite dc conductivity of $\sigma_0 = \pi e^2/2h$ at zero temperature [162, 163, 164, 165]. This is a direct consequence of the linear quasiparticle dispersion near the Dirac points (points of zero energy in the Brillouin zone), where the conduction and valence bands (defined as the eigenvalues of the tight-binding Hamiltonian with positive and negative energy, respectively¹) touch each other. At finite temperatures the optical conductivity is also of order σ_0 for visible frequencies (Fig. 7.1). This theoretical result neglecting disorder effects is indeed observed with excellent accuracy in optical absorption experiments on charge-neutral graphene [166].

Existing graphene samples [167, 168] are not pristine, however. Scanning-tunneling microscopy images of NSG samples show inhomogeneous patterns [169] whose origin was traced to the presence of impurities at the substrate-graphene interface [170]. It was proposed that impurities nucleate electron- or hole-rich puddles [171], which would obscure the intrinsic Dirac fermion physics of pristine graphene. In suspended graphene (SG) scattering can occur due to microscopic corrugations of the otherwise unstable two-dimensional crystal, so-called ripples, which were observed by transmission electron microscopy [172] and theoretically analyzed as one possible source for electron scattering [173, 174] or charge inhomogeneity [175].

The dc conductivity σ_{dc} of graphene is minimal at the charge neutrality point, which corresponds to a honeycomb lattice model at half-filling, i.e., with one electron

¹Note that the terminology of valence and conduction bands is conveniently borrowed from semiconductor physics, even though the “bands” defined in this way are not differentiable at the Dirac points. The conduction and valence bands are nevertheless uniquely defined as the $+$ and $-$ solutions ($\pm \sqrt{\epsilon_{\mathbf{k}}^2}$) of the eigenvalue equation for the 2×2 tight-binding Hamiltonian for each \mathbf{k} . In fact, a different classification with two partially filled bands would be arbitrary since all the filled states (at $T = 0$) in momentum space are continuously connected, and they would have to be split up into two subsets in an arbitrary way.

per lattice site. Upon applying a gate voltage σ_{dc} increases [161], hence the name “minimum conductivity”. Disorder-induced charge-density modulations imply a spatially varying chemical potential and thereby conceal clean Dirac fermion physics. Also the dc transport measurement process itself may introduce a bias, e.g., due to charge transfer at metal contacts [176].

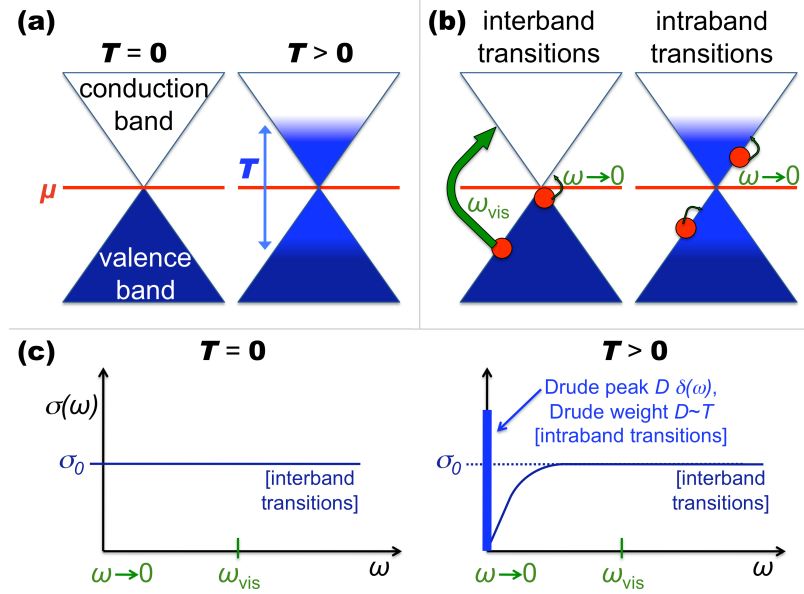


Figure 7.1: Transport at the charge neutrality point in pristine graphene. (a) At $T = 0$ the valence band (states below the chemical potential μ), sketched here for a single Dirac cone, is completely filled (indicated by the dark blue shading) and the conduction band is empty. At $T > 0$ some particles are thermally excited to the conduction band due to the Fermi-Dirac distribution (lighter blue shading). (b) Contributions to the conductivity: Only interband transitions are allowed at $T = 0$ due to Fermi blocking. Intraband transitions become important for dc transport at finite temperature. (c) Dynamical conductivity of pristine graphene within the Dirac-cone approximation at $T = 0$ and $T > 0$. At $T = 0$ interband transitions lead to a universal finite conductivity of $\sigma_0 = \pi e^2/2h$. For $T > 0$ a Drude peak emerges due to intraband transitions, with a Drude weight $D \propto T$. For visual frequencies ω_{vis} the optical conductivity still is of order σ_0 .

Theoretical work on transport in graphene comprises studies of charged-impurity scattering, as reviewed in Ref. [177], alternative sources of disorder [178], and also the

crossover between low- and high-density regimes [179]. More recent studies focused on ballistic [180] or diffusive transport [181]. Unresolved problems remain in particular in the low-density regime, which is relevant for the minimum conductivity problem.

Several theoretical approaches predicted a minimum conductivity of $4e^2/\pi h$ [182, 183, 184, 185, 186] in the absence of disorder. In fact, this limiting value at zero temperature is found if the dc limit first and the zero-disorder limit afterwards [162, 164]. Experiments on both NSG and SG samples [155, 161, 160] show non-universal values of the minimum conductivity. However, a trend is observed that the T dependence of the minimum conductivity is enhanced in clean SG samples as opposed to dirty SG samples [161] or NSG samples [161, 160]. In fact, the minimum conductivity increases upon an increase in temperature, i.e., it behaves as in a semiconductor. In contrast, at sufficiently large finite gate voltages a metallic T dependence of the conductivity is observed, with a linearly increasing resistivity as a function of T and a slope that decreases upon an increase in gate voltage [161].

Here we present a theory of the dc conductivity based on the Kubo formula. Disorder effects are included by a random chemical potential, which is treated within the coherent-potential approximation (CPA) [187, 188]. The associated disorder energy scale Γ may itself depend on temperature. We specifically investigate the case of a Lorentzian disorder distribution of width Γ (“Lloyd model”), for which the Kubo formula can be evaluated exactly within CPA. At half-filling σ_{dc} depends only on the type of disorder distribution and the dimensionless ratio T/Γ within the CPA for the Lloyd model. At high temperatures $T/\Gamma \gg 1$ the minimum conductivity increases linearly with T/Γ . For a temperature-dependent $\Gamma = \Gamma_0 + \alpha_1 T$ the minimum conductivity thus saturates at high temperatures. With this simple ansatz and a choice of typical meV energy scales for Γ the T dependence of σ_{dc} changes from semiconducting at half-filling to metallic at sufficiently large band filling, with an intermediate density regime where a crossover from metallic to semiconducting behavior is observed in

the relevant temperature range between 0 and 200 K. Moreover, the experimentally observed behavior with a linearly increasing resistivity at high temperatures in the metallic regime is reproduced by our ansatz, even including the decreasing slope upon increasing the density.

7.3 Model and Method

An infinite sheet of pristine graphene is modeled by a tight-binding Hamiltonian with an effective next-neighbor hopping on a honeycomb lattice without impurity scattering and electron-electron interactions. The longitudinal dc conductivity follows from the Kubo formula

$$\sigma_{\text{dc}} = \frac{2\pi e^2}{\hbar^2} \int_{-\infty}^{\infty} d\nu \int_{-\infty}^{\infty} d\epsilon \tilde{\rho}(\epsilon) [A_{\epsilon}(\nu) + A_{-\epsilon}(\nu)] A_{\epsilon}(\nu) \frac{-df_x}{dx} \Big|_{x=\nu-\mu}, \quad (7.1)$$

where $f_x = (1 + \exp(x/T))$ is the Fermi-Dirac distribution function ($k_B = 1$), μ is the chemical potential ($\mu = 0$ at half-filling), $\tilde{\rho}(\epsilon) = L^{-1} \sum_{\mathbf{k}} (\partial \epsilon_{\mathbf{k}} / \partial k_x)^2 \delta(\epsilon - \epsilon_{\mathbf{k}})$, L is the number of unit cells of the lattice, the integration variables ϵ and ν are energies and $A_{\epsilon}(\nu) = \delta(\epsilon - \nu)$. We use the Dirac cone approximation $\tilde{\rho}(\epsilon) = \hbar|\epsilon|/2\pi$ for $|\epsilon| < \epsilon_{\text{max}}$, where ϵ_{max} is a cutoff energy on the order of the half-bandwidth of graphene. Indeed the Dirac cone approximation for $\tilde{\rho}(\epsilon)$ gives the exact result for σ_{dc} and is a good approximation even for visual frequencies [163], where the full band structure leads to only weak quadratic corrections to the frequency dependence of the conductivity.

The term in Eq. (7.1) which involves $A_{\epsilon}(\nu)^2$ in the integrand leads to the usual intraband conductivity as in single-band models. It gives rise to a Drude-like contribution, hence an infinite dc conductivity in a perfect conductor. Also in the presence of electron-electron interactions this expression for the intraband conductivity remains correct if the self-energy $\Sigma(\nu)$ is local and $A_{\epsilon}(\nu) = -\text{Im}(\epsilon - \nu - \Sigma(\nu))^{-1}/\pi$ [189, 190].

The second term in Eq. (7.1), involving $A_{\epsilon}(\nu)A_{-\epsilon}(\nu)$, appears for a particle-hole

symmetric two-band system. It describes excitations of a particle at energy ϵ and a hole at $-\epsilon$ and accounts for interband transitions. This contribution gives rise to the visual transparency of graphene in the dc limit of the optical conductivity, $\sigma_0 = \pi e^2/2h$ (see Fig. 7.2c) [166]. A detailed derivation of the Kubo formula for the longitudinal conductivity of clean graphene and a discussion of intraband and interband excitations in this case are given in Appendix B.

The presence of disorder complicates the situation considerably. First of all discrete translational invariance is broken, rendering microscopic theoretical approaches much more difficult than in the homogeneous case. Secondly, the precise type of disorder is usually unknown. One standard approach is the Anderson tight-binding model [191] with local potential impurities,

$$H = H_0 + \sum_i V_i n_i, \quad (7.2)$$

where H_0 is the tight-binding Hamiltonian for the clean system, n_i is the local density operator on site i of the lattice and V_i is a random variable drawn from some distribution function $P(V_i)$. Here we do not aim at a full microscopic description of disorder, e.g., in the spirit of a self-consistent diagrammatic treatment of impurity scattering effects [192]; in any case it is known that weak localization is suppressed by long-range scattering in graphene [193, 194, 195]. Instead we apply the coherent-potential approximation (CPA) [187, 188], which is a mean-field approach to determine an effective random medium described by a local self-energy $\Sigma(\omega)$, which is determined by a self-consistent solution of the CPA equations

$$\begin{aligned} \bar{G}(\omega) &= G_0(\omega - \Sigma(\omega)), \\ \bar{G}(\omega) &= \tilde{D}[\mathcal{G}^{-1}(\omega)] = \int dV \frac{P(V)}{\mathcal{G}^{-1}(\omega) - V}, \\ \mathcal{G}^{-1}(\omega) &= \bar{G}^{-1}(\omega) + \Sigma(\omega), \end{aligned} \quad (7.3)$$

where $G_0(z) = \int d\omega \rho_{\text{DOS}}(\omega)/(z - \omega)$ is the local Green function of the clean system

described by H_0 , $\mathcal{G}(\omega)$ is a dynamical Weiss field and $\tilde{D}[z]$ is the Hilbert transform with respect to the disorder distribution P as defined above.

Within CPA the Kubo formula, Eq. (7.1), provides an the exact equation for the conductivity [196] if one uses $A_\epsilon(\nu) = -\text{Im}(\epsilon - \nu - \Sigma(\nu))^{-1}/\pi$. Moreover, the CPA equations (7.3) can be solved, at least numerically, for an arbitrary disorder distribution. In order to keep the subsequent analysis as simple and transparent as possible, we focus on the specific case of a Lorentzian disorder distribution of width Γ ,

$$P(x) = \frac{1}{\pi} \frac{\Gamma}{\Gamma^2 + x^2}. \quad (7.4)$$

This is the so-called Lloyd model, for which the CPA equations are exactly solvable using $\tilde{D}[z] = (z + i\Gamma)^{-1}$, which yields $\Sigma(\nu) = -i\Gamma$. Hence we obtain for the Lloyd model

$$A_\epsilon(\nu) = \frac{1}{\pi} \frac{\Gamma}{\Gamma^2 + (\epsilon - \nu)^2} \quad (7.5)$$

as the input quantity for Eq. (7.1). $A_\epsilon(\nu)$ can be written in the form $a((\epsilon - \nu)/\Gamma)/\Gamma$, from which it follows that the dc conductivity is only a function of the ratio T/Γ for $\mu = 0$ (minimum conductivity, $\sigma_{\min} = \sigma_{\text{dc}}(\mu = 0)$) and of μ/Γ for $T = 0$ (but only if $\mu \ll \epsilon_{\max}$, which is, however, fulfilled in the cited experiments).

The scaling behavior of σ_{\min} can be traced to two reasons: (a) the cutoff energy ϵ_{\max} can be replaced by infinity in the ϵ -integral in Eq. (7.1) and thus does not appear as an additional energy scale, and (b) for dimensional reasons the dc conductivity is universal in the sense that it does not depend on the hopping matrix element t of the underlying two-dimensional tight-binding Hamiltonian and, consequently, not on the Fermi velocity v_F . Both reasons are directly related to the linearity of the quasiparticle-energy dispersion in graphene up to energies much larger than the relevant temperatures.²

²For calculations at finite density the universality in this sense is not given any more, since the density dependence of the chemical potential contains the hopping matrix element t .

In experiments the gate voltage controls the electronic density per area, n , measured from half-filling. For given temperature T , disorder strength Γ and chemical potential μ the density is given by

$$n = \int_{-\infty}^{\infty} d\omega \rho_{\text{DOS}}(\omega) (f_{\omega-\mu} - f_{\omega}), \quad (7.6)$$

where

$$\rho_{\text{DOS}}(\omega) = \frac{4}{\sqrt{3}\pi t^2 A_u} \int_{-\epsilon_{\text{max}}}^{\epsilon_{\text{max}}} d\epsilon |A_{\epsilon}(\omega)| \quad (7.7)$$

is the density of states (for both spins) for the disordered system, $t = 2.7$ eV the hopping matrix element of the tight-binding model, $A_u = 3\sqrt{3}a_0^2/2$ the size of the unit cell and $a_0 = 1.42 \times 10^{-10}$ m the interatomic distance on the honeycomb lattice.

7.4 Results

We now turn to the discussion of the results for the dc conductivity obtained from the CPA approximation to the Lloyd model. We first keep the disorder strength Γ fixed (temperature-independent) and discuss basic properties of the minimum conductivity and the conductivity at finite chemical potential and zero temperature. We show the density dependence of the conductivity for a typical disorder strength (on the order of meV) and for typical temperatures in the range from 0 K to 200 K. Especially we consider the temperature dependence of the resistivity (inverse of the conductivity) at fixed densities and show that, at high densities, a temperature-independent Γ is insufficient to explain the linear T dependence of the resistivity observed in experiments. Adding a linear T -dependent contribution to Γ , which should be viewed as a phenomenological parameter, the experimental observation can be matched by our ansatz. Moreover, the observed density dependence of the slope in the T -linear regime of the resistivity comes out naturally without any additional assumptions. For a selected T -dependent $\Gamma = \Gamma_0 + \alpha_1 T$ the minimum conductivity is observed to increase upon an increase in temperature but with a decreasing slope and a saturation

at high temperatures, also in similarity to experiments. Finally, the T dependence of the conductivity is shown, where a density-dependent crossover from metallic behavior ($d\sigma_{\text{dc}}/dT < 0$) at low T to semiconducting behavior ($d\sigma_{\text{dc}}/dT > 0$) at high T is observed.

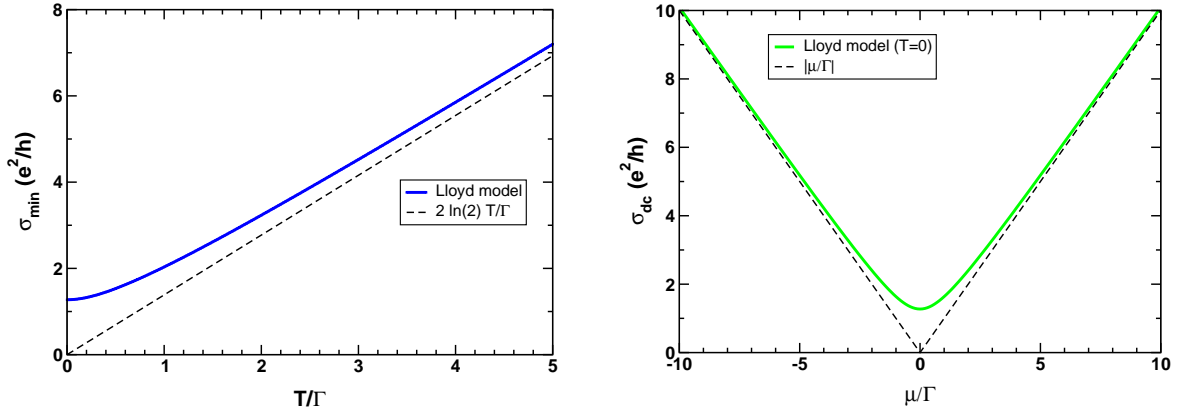


Figure 7.2: DC conductivity for the Lloyd model in CPA. Left diagram: Minimum conductivity ($\mu = 0$) as a function of T/Γ . Right diagram: DC conductivity at $T = 0$ as a function of μ/Γ .

The minimum conductivity σ_{\min} as a function of T/Γ for the Lloyd model with disorder strength Γ is shown in the left diagram in Fig. 7.2. For $T/\Gamma \rightarrow 0$, σ_{\min} tends to the limiting value $4e^2/\pi h$. On the other hand σ_{\min} increases linearly with T/Γ for $T/\Gamma \gg 1$,

$$\sigma_{\min} = \frac{e^2}{h} \left(2 \ln(2) \frac{T}{\Gamma} + \mathcal{O}\left(\frac{\Gamma}{T}\right) \right). \quad (7.8)$$

In order to provide a better understanding of the physical processes involved we discuss the relevant contributions to σ_{\min} . First of all we note that the clean case at zero temperature, where the limits $\Gamma \rightarrow 0$ and $T \rightarrow 0$ are both taken before the dc limit, is not recovered by our theory for σ_{dc} . Recall that at zero temperature intraband excitations are blocked since the valence band is completely filled and the conduction band is completely empty. Thus only interband excitations occur, leading to $\text{Re } \sigma(\omega \rightarrow 0) = \sigma_0$ [163] (see Fig. 7.1 and Appendix B). Our theory, on the other

hand, is rather tailored to describe dc measurements, for which the dc limit must be taken first, and which are in addition always performed at finite T .

At finite temperature thermally excited particles in the conduction band render intraband particle-hole excitations possible, leading to a non-zero Drude weight (Fig. 7.2 c) and thus an infinite σ_{dc} (for $\Gamma \rightarrow 0$, thus $T/\Gamma \rightarrow \infty$), while interband low-energy excitations are blocked by thermally occupied states in the conduction band. Upon an increase in the disorder strength Γ the minimum conductivity decreases, and for $T/\Gamma \rightarrow 0$ both intraband and interband excitations contribute equally to $\sigma_{\text{min}} = \sigma_{\text{dis}}$ (disordered limit). Viewed as a function of temperature for fixed Γ the minimum conductivity is semiconducting, i.e., $d\sigma_{\text{dc}}/dT > 0$.

At finite chemical potential the interband excitations become less important, and the behavior is determined mostly by intraband excitations. The situation thus resembles more and more the case of a single partially filled band for higher densities, where metallic behavior sets in for sufficiently low temperatures and finite densities, i.e., $d\sigma_{\text{dc}}/dT < 0$.

The dc conductivity at $T = 0$ as a function of μ/Γ is shown in the right diagram in Fig. 7.2. It tends to the limiting value $4e^2/\pi h$ for $\mu/\Gamma \rightarrow 0$ and increases linearly for $|\mu/\Gamma| \gg 1$ but well below $\epsilon_{\text{max}}/\Gamma$, which is the case for all the densities achieved in experiments. This linear dependence upon the chemical potential for large $|\mu/\Gamma|$ is analytically extracted from the Kubo formula, taking into account intraband excitations only,

$$\sigma_{\text{dc}}(\mu, T = 0) \approx \frac{2e^2}{\pi h} \int_{-\infty}^{\infty} d\epsilon |\epsilon| \frac{\Gamma^2}{(\Gamma^2 + (\epsilon - \mu)^2)^2} \approx \left| \frac{\mu}{\Gamma} \right| \frac{e^2}{h}. \quad (7.9)$$

In the cited experimental literature the conductivity data is shown for fixed densities instead of fixed chemical potential [161, 160]. For a fixed value of the disorder strength, $\Gamma = 1$ meV, we therefore show in Fig. 7.3 the dc conductivity and its inverse, the resistivity ρ , as a function of density for selected temperatures. Since the

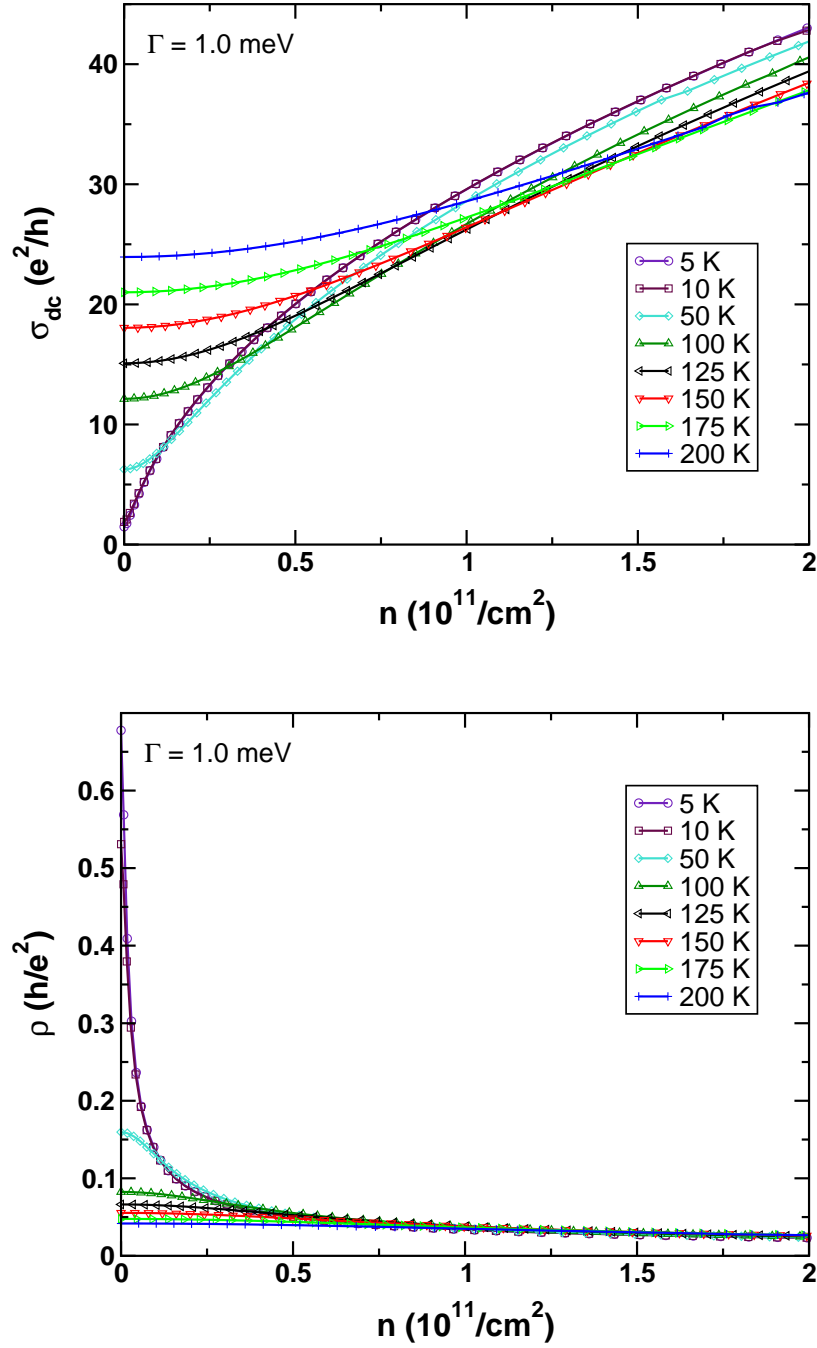


Figure 7.3: Upper diagram: Conductivity as a function of density for the indicated temperatures for temperature-independent Γ . Lower diagram: Same data as in the upper diagram, but resistivity instead of conductivity ($\rho = \sigma_{\text{dc}}^{-1}$).

density depends quadratically on the chemical potential for $\mu/\Gamma \gg 1$ and σ_{dc} depends linearly on $|\mu/\Gamma|$ in this limit and at zero temperature, the low-temperature conductivity increases like \sqrt{n} at high densities. In fact a sublinear density dependence of the conductivity is reported also in Ref. [160].

In Ref. [161] a linear increase of the resistivity as a function of temperature at elevated temperatures was observed for high densities. For a temperature-independent Γ , $\sigma_{\text{dc}} = |\mu/\Gamma| e^2/h$ for large $|\mu/\Gamma|$, and the temperature dependence of the chemical potential for a fixed density is $\mu = \mu(T = 0) + \mathcal{O}(T^2)$ (like for the standard Fermi gas). Hence, for a fixed density $\sigma_{\text{dc}}(T) = \sigma_{\text{dc}}(T = 0) + \mathcal{O}(T^2)$ and thus $\rho = \rho(T = 0) + \mathcal{O}(T^2)$. Following this argument a linear dependence of ρ on temperature requires a temperature-dependent Γ within our ansatz. In fact, a linearly increasing resistivity at high densities naturally occurs for a T -dependent Γ with $\Gamma = \Gamma_0 + \alpha_1 T$,

$$\rho \approx \frac{\Gamma}{\mu} \frac{h}{e^2} = \frac{\Gamma_0}{\mu} \frac{h}{e^2} + \frac{\alpha_1 T}{\mu} \frac{h}{e^2}. \quad (7.10)$$

Note that μ depends not only explicitly on temperature, but also implicitly via the T -dependent Γ . For very large fillings, however, this implicit T dependence is negligible. In fact also the explicit T dependence is very weak since it scales like the ratio of temperature to Fermi energy, which is very small for the relevant temperatures.

The density dependence of the resistivity for the selected T -dependent disorder strength is shown in the upper diagram of Fig. 7.4. For moderate temperatures, below 200 K, the linearity of the resistivity is presented in the lower diagram of Fig. 7.4. In fact from Eq. (7.10) one can also see that the slope in the linear regime is proportional to α_1/μ , and since $\mu \propto \sqrt{n}$ the slope decreases like $1/\sqrt{n}$. For very large temperatures (well above 200 K for sufficiently large densities, but below 200 K for moderate densities) there is a deviation from the linear behavior, and the resistivity decreases again since also interband excitations contribute.

The anticipated crossover from metallic behavior at finite densities and low tem-

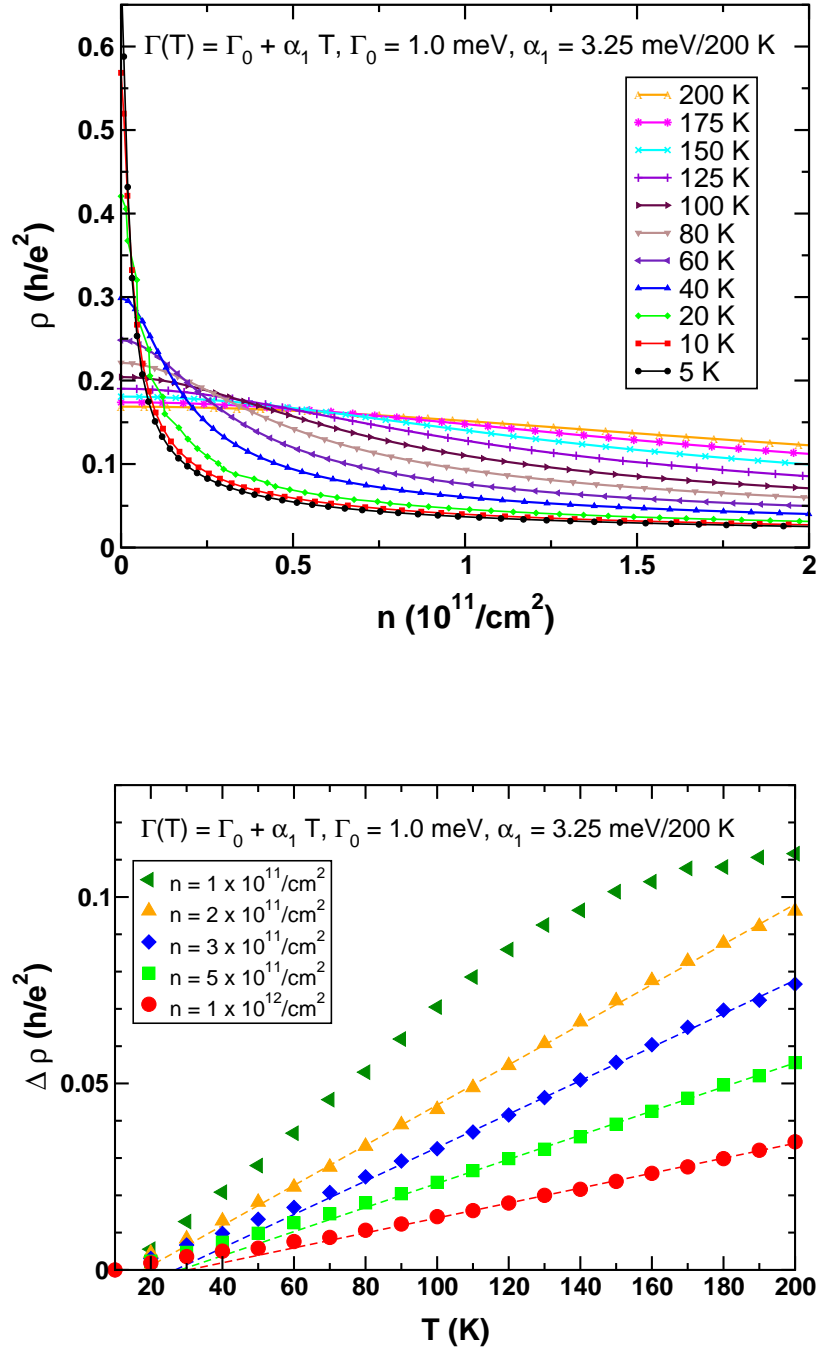


Figure 7.4: Upper diagram: Resistivity as a function of density for the indicated temperatures. Lower diagram: Resistivity difference with respect to values at 10 K as a function of temperature for the indicated densities. The dashed lines are linear fits for the data points between 100 K and 200 K.

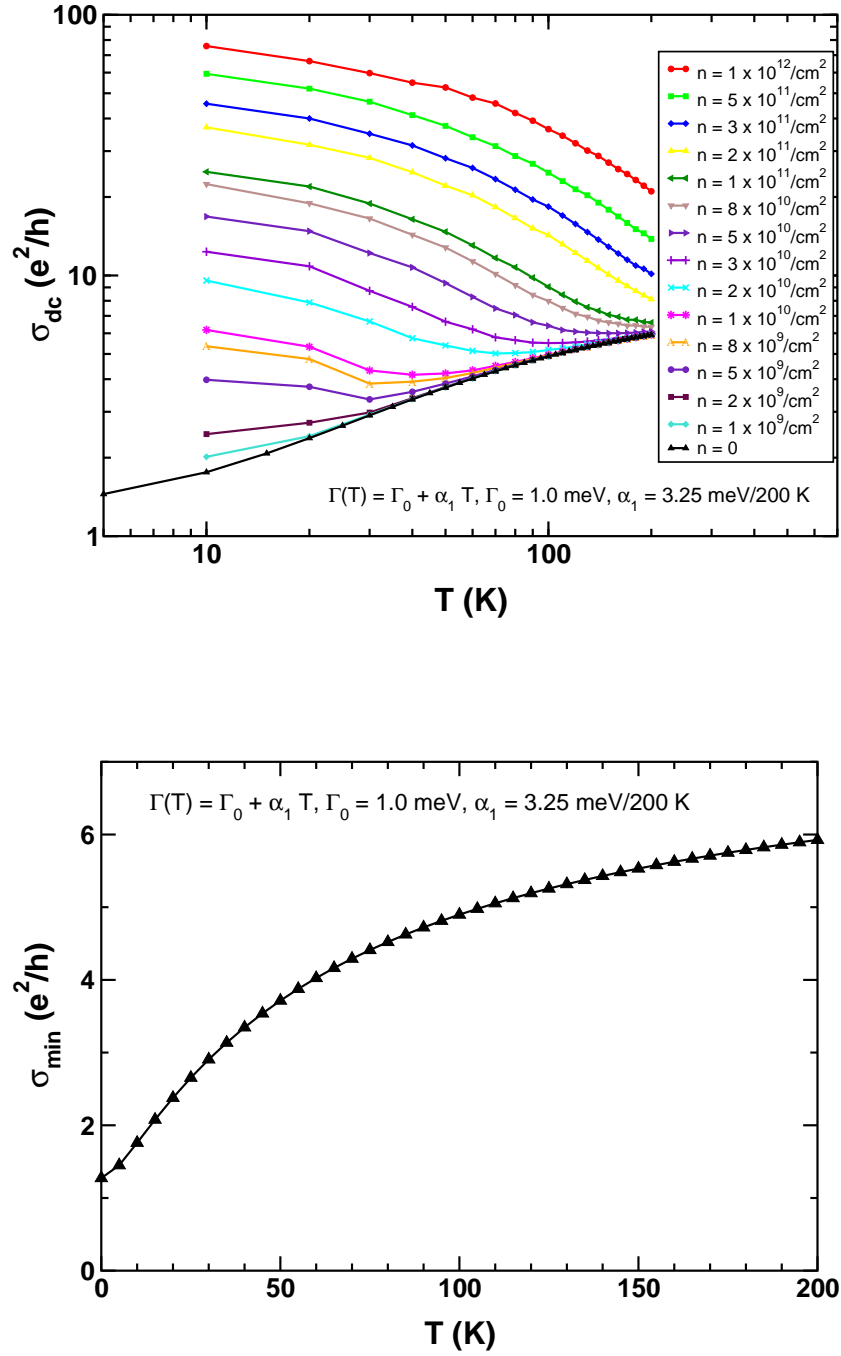


Figure 7.5: Upper diagram: Conductivity as a function of temperature for the indicated densities and T dependence of Γ . Lower diagram: Temperature dependence of the minimum conductivity.

peratures to semiconducting behavior at elevated temperatures is shown in the upper diagram of Fig. 7.5. The crossover temperature is zero at zero density, since the minimum conductivity increases with temperature for all temperatures, and increases upon an increase in the density. In fact, for the selected temperature dependence of Γ the behavior is always metallic below 200 K for densities larger than $8 \times 10^{10}/\text{cm}^2$. The temperature dependence of the minimum conductivity for the same T -dependent Γ is shown in the lower diagram of Fig. 7.5. Here a sublinear T dependence of σ_{\min} is observed for elevated temperatures. Indeed, the curvature of σ_{dc} changes sign at an intermediate temperature depending on the relative sizes of Γ_0 and α_1 . An increasing σ_{\min} as a function of temperature with a sublinear behavior at elevated T yet below 200 K is also observed in experiments [161, 160].

7.5 Summary and Discussion

To summarize, we have presented a phenomenological theory of the temperature dependence of the dc conductivity of graphene at zero and finite particle densities including potential disorder in a coherent-potential approximation (CPA). To be specific we have chosen a Lorentzian disorder distribution (“Lloyd model”), which has the advantage that the CPA equations are exactly solvable in this case.³ Our approach recovers well-established limits in the clean case and at the same time enables a better understanding of the remarkable transport properties of graphene. Especially an enhanced T dependence of the minimum conductivity in cleaner SG samples is explained, and we find $\sigma_{\min} \propto T/\Gamma$ for $T/\Gamma \gg 1$. As a consequence we expect a very steep increase of σ_{\min} with temperature in even cleaner samples [159]. Moreover we have shown that the observed linearly increasing resistivity as a function of temperature at high densities and the density dependence of the slope are explained

³The method is not restricted to the Lloyd model, however, and it may be interesting to compare our results with results for other disorder distributions.

by a temperature-dependent $\Gamma = \Gamma_0 + \alpha_1 T$. This phenomenologically determined T dependence of Γ suggests the existence of at least two sources for scattering in suspended graphene. The constant Γ_0 points to static disorder due to impurities, whereas the T -linear part $\alpha_1 T$ suggests scattering off a thermally excited perturbation. One obvious possibility is a ripple-related mechanism, since ripples are thermally excited in suspended graphene. In fact, even the linear T dependence of the scattering rate could be explained within the ripple scenario [174].

In this work we have investigated the role of disorder, as described by an Anderson impurity model with a phenomenological disorder strength, as a source for scattering in graphene. As pointed out in Ref. [176], it is essential to understand which additional extrinsic effects mask intrinsic properties of graphene, especially the sensitive Dirac fermion physics at the neutrality point. Possible extrinsic perturbations are the influence of metal contacts via contact resistance, spurious chemical doping into the contact regions, or macroscopic charge inhomogeneity on length scales reaching the sample size. Such effects need to be added to the picture in order to gain a full understanding of the unusual transport properties of graphene especially at the charge-neutrality point. Also improved techniques for the doping of graphene using organic molecules [197] may help to unveil its intrinsic transport properties. Further theoretical and experimental activity should clarify these aspects so that graphene can fulfill its promise as a basis of future electronic devices.

Chapter 8

Outlook

Electronic correlations are at the heart of many fascinating phenomena and keep challenging our theoretical understanding. New or improved methods to qualitatively and even quantitatively capture correlation effects help us understand the intriguing effects in many materials. Dynamical-mean field methods, as applied in this Thesis, are tailored to investigate correlated electron systems.

As an example, the difference between the electron- and hole-doped cuprates was only recently traced to the difference in the strength of electronic correlations using LDA+DMFT [198]. It turned out that the electron-doped materials are less strongly correlated, and that their parent compounds are Slater insulators, which owe their insulating behavior to the opening of a gap due to long-range magnetic order, rather than Mott insulators, in which correlations are strong enough to open a gap even in the absence of magnetic order. Simultaneously, the synthesis of an “ambipolar” cuprate material allowed for a direct comparison between electron and hole doping in the same compound. Here the asymmetry in transport measurements was indeed related to a difference in the nature of the antiferromagnetic ground states on the electron- and hole doped sides [199].

Investigations of new materials are therefore guided by basic questions that can be answered by correlated electron theorists: What is the band structure? How strong

are correlations? What is the symmetry of the superconducting order parameter? Which magnetic ordering patterns occur? How conventional or unconventional is the normal-conducting state? The latter question is related to the observation of pseudogap behavior and the notion of a “strange metal” [200] in the cuprates. As shown in this Thesis unconventional metallic phases can be observed in a wide parameter regime in low-dimensional correlated systems.

Not only theoretical investigations but possibly also studies of ultracold atomic or molecular Fermi gases, that can be viewed as experimental realizations¹ of theoretical models, may provide insight into these questions. Only recently pseudogap behavior above the superfluid transition temperature was claimed to be observed in experiments on cold atoms [202].

Of special interest are superconducting materials that come in families, like the cuprates or the ferropnictides [203]. It has been appreciated that unconventional superconductivity is likely caused by an electronic pairing mechanism [204], and that the pairing symmetry is sensitive not only to the momentum dependence of the pairing interaction, but also to the band structure and especially to the topology as well as the orbital composition of the Fermi surface. Especially since the discovery of superconductivity in the ferropnictides, which are multiband systems with disconnected Fermi surface sheets made up of a variety of orbitals, it is natural to ask what influence a more complicated band structure has on the superconducting and magnetic properties.

Moreover, insights about multiband systems gained from the recent interest in the pnictides may in turn help to learn more about the seemingly well-studied cuprates. For example, a two-orbital model for the cuprates including the $\text{Cu-}d_{z^2}$ orbitals in

¹The interpretation of ultracold gases in terms of many-body models like the Hubbard model is not straightforward. It is in fact difficult to extract the relevant parameters and to construct an appropriate Hamiltonian with the correct interactions. A major advantage of cold gases is that the model parameters can be tuned more easily than in a solid. For a review see Ref. [201].

addition to the $d_{x^2-y^2}$ orbitals explains why the single-layer Hg compound has a considerably different superconducting critical temperature than the La compound [205]. Here the influence of orbital contributions to the Fermi surface, rather than the mere shape of the Fermi surface, was identified as an important factor, and that strong admixtures of d_{z^2} orbital content to the mainly $d_{x^2-y^2}$ -derived band crossing the Fermi surface were found to be counteracting superconductivity in the La compound.

The theoretical study of multiband systems is of course more complicated than the study of the simpler one-band Hubbard model. For low-dimensional multiband systems it is desirable to combine band structure calculations with cluster DMFT to treat multiband and non-local correlation effects, and to capture unconventional pairing symmetries in a multiband model.

To illustrate how new states of matter may arise in multiband models, pairing in a two-band model is studied within BCS theory [204]. In a simple setup the coupled gap equations are derived for pairing interactions $V_{\mathbf{k}'\mathbf{k}}^{ij}$ (for the notation see Section 3.5.1) between Cooper pairs in bands i and j , each of which is made up of electrons in the same band.² The coupled gap equations read

$$\Delta_1(\mathbf{k}) = - \sum_{\mathbf{k}'} \left(V_{\mathbf{k}'\mathbf{k}}^{11} \frac{\Delta_1(\mathbf{k}')}{2E_1(\mathbf{k}')} \tanh \frac{\beta E_1(\mathbf{k}')}{2} + V_{\mathbf{k}'\mathbf{k}}^{21} \frac{\Delta_2(\mathbf{k}')}{2E_2(\mathbf{k}')} \tanh \frac{\beta E_2(\mathbf{k}')}{2} \right), \quad (8.1)$$

$$\Delta_2(\mathbf{k}) = - \sum_{\mathbf{k}'} \left(V_{\mathbf{k}'\mathbf{k}}^{22} \frac{\Delta_2(\mathbf{k}')}{2E_2(\mathbf{k}')} \tanh \frac{\beta E_2(\mathbf{k}')}{2} + V_{\mathbf{k}'\mathbf{k}}^{12} \frac{\Delta_1(\mathbf{k}')}{2E_1(\mathbf{k}')} \tanh \frac{\beta E_1(\mathbf{k}')}{2} \right), \quad (8.2)$$

with order parameters $\Delta_i(\mathbf{k})$ and dispersions $E_i(\mathbf{k}) = \sqrt{\epsilon_i(\mathbf{k})^2 + \Delta_i(\mathbf{k})^2}$ for band $i = 1, 2$.

Fascinating new order parameter symmetries may indeed be stabilized by a more complicated topology of the Fermi surface with disconnected sheets. As an example, a time-reversal symmetry breaking $s+id$ -wave pairing state [206] is possible in a system with Fermi surface pockets around the $(0,0)$ and (π,π) points. We have conducted

²In principle, also interband pairing is possible.

first mean-field studies which show that transitions from d -wave via $s+id$ to extended s -wave behavior can be investigated even in a simple two-band model with two square lattice sheets coupled by a hybridization V . Within the BCS approach, a non-local attractive pairing interaction (see Eq. (3.55)) indeed favors various order parameter symmetries depending on the topology of the Fermi surface, which is controlled by the interlayer hybridization. Further research in this direction, including realistic band structures and methods going beyond BCS theory, is a challenging and fascinating goal for the future.

In addition to the development of more refined and efficient numerical methods, a thorough understanding of emergent phenomena also demands progress regarding analytical techniques. The formulation of a mean-field theory of unconventional superconductivity in the repulsive Hubbard model still is an open problem, for example. As shown in this Thesis, even the two-dimensional one-band Hubbard model at half-filling is still not completely understood. In fact, while renormalized mean-field treatments have been undertaken [75], a simple Hartree-Fock like decoupling for non-local superconducting states has not been achieved yet. In particular for weak interactions such a decoupling would be helpful to understand the observed superconducting and non-Fermi liquid states (see Chapter 5) more intuitively. So far a mean-field decoupling based on a transformation to bond operators has been performed for the Heisenberg and t - J models [207, 208]. For the Hubbard model, however, such an approach is much more difficult to accomplish due to the larger Hilbert space. Also the bond operator method has the disadvantage that it is naturally built for models with spontaneous or explicit bond-centered order, as in spin Peierls systems. Perhaps a conveniently chosen set of unitary transformations, similar to the Schrieffer-Wolff transformation, may allow for a mean-field decoupling with superconducting pair fields in the repulsive Hubbard model.

Finally the theoretical modeling of interfaces and heterostructures of correlated

materials requires the adaption of dynamical mean-field methods to inhomogeneous systems, an approach which is referred to as real-space dynamical mean-field theory (R-DMFT) [209, 25]. R-DMFT has already been used to study the penetration of a metal into a Mott insulator via the Kondo effect [210] or the emergence of a metallic state at the interface between a band insulator and a Mott insulator [211]. Certainly the combination of the variety of possible quantum states, collective phenomena and ordering patterns, which already appear in correlated bulk materials, with new effects specific to interfaces [212] poses grand challenges, but also offers great opportunities [213]. It is therefore highly desirable to understand correlation effects in inhomogeneous model systems and to go beyond studies of simplified models to incorporate the complex characteristics of real materials.

Appendix A

Analytic Continuation of QMC Data

Solutions to the DMFT equations in this thesis were obtained using the CTQMC impurity solver (see Chapter 3). In some parts of this work local correlation functions, namely the single-particle Green function

$$G(\tau) = -\langle \mathcal{T}_\tau c(\tau) c^\dagger(0) \rangle_{S_{\text{eff}}} \quad (\text{A.1})$$

and the spin-spin correlation function

$$\chi(\tau) = \langle S_z(\tau) S_z(0) \rangle_{S_{\text{eff}}}, \quad (\text{A.2})$$

were analytically continued to the real-frequency axis. The analytical continuation, which is a difficult and in principle ill-conditioned problem, yields estimates of the spectral function

$$A(\omega) = -\frac{1}{\pi} \text{Im} G(\omega + i0^+) \quad (\text{A.3})$$

and the imaginary part of the spin susceptibility

$$\text{Im} \chi(\omega) = \text{Im} \chi(i\omega_n \rightarrow \omega + i0^+). \quad (\text{A.4})$$

These quantities were used to extract the charge and spin gaps in Chapter 4 and the nuclear spin-lattice relaxation rate in Chapter 6.

To this end a maximum entropy (MaxEnt) method, as described in Refs. [39, 51], was employed. The basic problem of analytic continuation consists in inverting the

relation (given here for G)

$$G(\tau) = \int_{-\infty}^{\infty} \frac{\exp(-\tau\omega)}{1 + \exp(-\beta\omega)} A(\omega), \quad (\text{A.5})$$

with the fermionic kernel

$$K(\tau, \omega) = \frac{\exp(-\tau\omega)}{1 + \exp(-\beta\omega)}. \quad (\text{A.6})$$

The QMC data for $G(\tau)$ are given as N_d measurements at Λ points on a τ grid, i.e., $G_l \equiv G(l\Delta\tau)$ with $0 \leq l < \Lambda$. For simplicity we assume that the measurements are independent both in imaginary time (no autocorrelation between adjacent time slices) and in computer time (no autocorrelation between subsequent measurements), the latter of which is assured by binning a large number of subsequent measurements and performing the maximum entropy method for the binned variables. If we further assume that the statistical errors are distributed according to a Gaussian distribution, the probability for the measured values $\bar{G} \equiv \{\bar{G}_l\}$, $\bar{G}_l = \sum_{i=1}^{N_d} G_l^{(i)}$, to be observed given the “true” spectrum A is

$$P(\bar{G}|A) \propto e^{-\frac{1}{2}\chi^2[\bar{G}, A]}, \quad \chi^2[\bar{G}, A] = \sum_{l=0}^{\Lambda-1} \frac{\bar{G}_l - G_l}{\sigma_l^2}, \quad (\text{A.7})$$

where $\sigma_l^2 \approx \sum_{i=1}^{N_d} (\bar{G}_l - G_l^{(i)})^2 / (N_d(N_d - 1))$ is estimated from the data.

In order to find the most probable spectrum given the measured G one makes use of Bayes’ theorem,

$$P(A|\bar{G}) = P(\bar{G}|A)P(A)/P(\bar{G}). \quad (\text{A.8})$$

The two unknown quantities are $P(\bar{G})$, which is constant for given data and independent of A , and $P(A)$, the probability of a spectrum A in the absence of any data. In order to estimate $P(A)$ one makes an entropic ansatz,

$$P(A) = e^{\alpha S[A(\omega), m(\omega)]}, \quad (\text{A.9})$$

where α is a Lagrange parameter, m is a default model (which may contain prior knowledge about the spectrum) and S is a generalized Shannon-Jaynes entropy,

$$S[A, m] = \int_{-\infty}^{\infty} d\omega \left(A(\omega) - m(\omega) - A(\omega) \ln(A(\omega)/m(\omega)) \right). \quad (\text{A.10})$$

The entropy has a maximum value of 0 when $A = m$, and it is the more negative the more the spectrum A differs from the default model m . The posterior probability $P(A|\bar{G}, m, \alpha)$ is then given by

$$P(A|\bar{G}, m, \alpha) \propto e^{\alpha S[A(\omega), m(\omega)] - \frac{1}{2} \chi^2[\bar{G}, A]}. \quad (\text{A.11})$$

Numerically one may use different algorithms to obtain the most probable spectrum. A simple MaxEnt program searches for the spectrum A with maximum probability for given α and searches for the best value of α to find a balance between a good match of data and a high entropy, e.g., the value with the highest probability $P(A|\bar{G}, m, \alpha)$ (classic MaxEnt) or chosen such that $\chi^2 = \Lambda$ (historic MaxEnt).

In practice the MaxEnt procedure should be repeated for different default models (e.g., Gaussian and flat default models) and for different subsets of data (if one has enough measurements). Also one may increase the measured error bars σ_l by hand and check how robust the features in A really are. The Green function is typically measured on 1000 time slices in CTQMC in order to simplify the Fourier transformation needed during the DMFT self-consistency cycle. For the MaxEnt procedure data points may be skipped in order to avoid numerical problems [51], so that 100-200 time slices are used in MaxEnt. As an example, we show in Fig. A.1 the dependence of the spectrum on the size of the error bars for data obtained in the Mott insulating phase of the κ -Cl model introduced in Chapter 6. Clearly the basic features of the spectrum are robust with respect to the different error bars, such as the energy gap, the lower and upper Hubbard bands and the sharp peak just below zero energy.

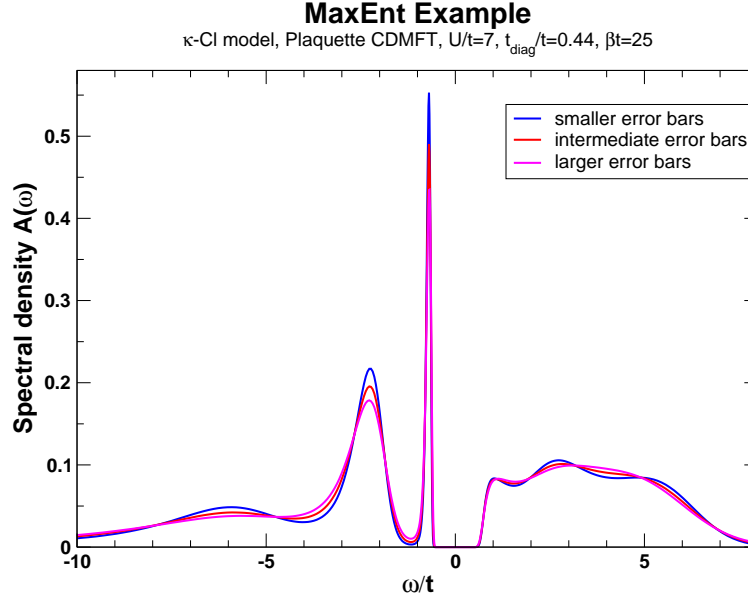


Figure A.1: Example of analytically continued data for the κ -CI model (Chapter 6) with different sizes of error bars.

The analytical continuation of spin-spin correlation functions is analogous to the algorithm for the Green function, albeit with a bosonic instead of the fermionic kernel,

$$\chi(\tau) = \int_0^\infty \frac{\omega(\exp(-\tau\omega) + \exp(-(\beta - \tau)\omega))}{1 - \exp(-\beta\omega)} \frac{\text{Im}\chi(\omega)}{\omega}. \quad (\text{A.12})$$

Here it is more convenient to divide the dynamic susceptibility by ω so that the spectral density $\text{Im}\chi(\omega)/\omega$ is positive definite and the kernel

$$K(\tau, \omega) = \frac{\omega(\exp(-\tau\omega) + \exp(-(\beta - \tau)\omega))}{1 - \exp(-\beta\omega)} \quad (\text{A.13})$$

is non-singular at zero frequency.

In contrast to the Green function the spin-spin correlation function is not determined during each iteration of the self-consistency cycle in DMFT but only in the last iteration after convergence is reached. Typically the spin-spin correlation function is measured on $A = 100$ -200 time slices. The accurate measurement of the spin-spin

correlation function (two-particle correlation functions in general) is more difficult than for the single-particle Green function, and it is therefore necessary to perform longer QMC runs in order to reduce the size of the error bars.

Appendix B

Electrodynamics on the Honeycomb Lattice

Most of the following calculations have been performed by Armin Seibert during his Fortgeschrittenen-Praktikum in our group. They are quoted here with his permission in order to make contact with the results for disordered graphene in Chapter 7. A derivation of the Kubo formula on the honeycomb lattice will be given, and the resulting dynamical conductivity will be discussed focusing on the dc limit.

We consider a tight-binding Hamiltonian,

$$H_0 = -t \sum_m \left(a_m^\dagger b_m + a_{m+\mathbf{v}_1}^\dagger b_m + a_{m+\mathbf{v}_2}^\dagger b_m + \text{h.c.} \right), \quad (\text{B.1})$$

which describes electrons hopping on a honeycomb lattice with the hopping amplitude $t \approx 2.7 \text{ eV}$ [165]. The lattice consists of two triangular sublattices A and B with a lattice constant a , and the interatomic distance is $a_0 = a/\sqrt{3}$, which is set to unity in the following. We introduce the fermionic operators $a_{m+\mathbf{v}_i}^{(\dagger)}$ and $b_m^{(\dagger)}$ which annihilate (create) electrons on the respective sublattices A and B in the m^{th} unit cell, as shown in Fig. B.1. The basis vectors $\mathbf{v}_{1/2}/a_0 = (3/2, \mp\sqrt{3}/2)$ are also shown in Fig. B.1. Here we suppress the spin degree of freedom for simplicity. It merely doubles the number of states and enters the results as a prefactor of 2 in the conductivity.

The Hamiltonian (B.1) is diagonalized by Fourier transformation and subsequent Bogoliubov transformation. In the diagonal representation with the fermionic opera-

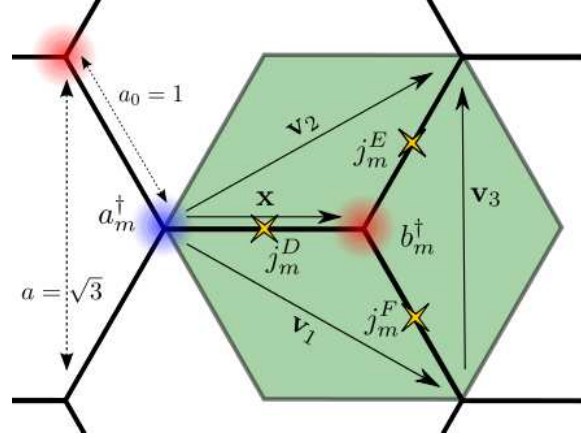


Figure B.1: Unit cell of the honeycomb lattice with basis vectors $\mathbf{v}_{1/2} = (3a_0/2, \mp\sqrt{3}a_0/2)$ of the triangular superlattice and the basis vector $\mathbf{x} = (a_0, 0)$ connecting A and B sublattices. The lattice constant of the triangular superlattice is $a = \sqrt{3}a_0$ and $a_0 = 1$ (unit length). For the case of graphene one has $a_0 = 1.42 \times 10^{-10}$ m. The size of the unit cell is $A_u = 3\sqrt{3}a_0^2/2$. The fermionic operators a^\dagger and b^\dagger create electrons on the sublattices A and B. The current operators $j^{D,E,F}$ describe charge currents flowing along the respective bonds from the B site to the A sites. Figure created by Armin Seibert.

tors $\alpha_{\mathbf{k}}^{(\dagger)}$ and $\beta_{\mathbf{k}}^{(\dagger)}$ the Hamiltonian reads

$$H_0 = - \sum_{\mathbf{k}} \left(\epsilon_{\mathbf{k}} \alpha_{\mathbf{k}}^\dagger \alpha_{\mathbf{k}} - \epsilon_{\mathbf{k}} \beta_{\mathbf{k}}^\dagger \beta_{\mathbf{k}} \right). \quad (\text{B.2})$$

The energy dispersion $\epsilon_{\mathbf{k},\pm} = \pm\epsilon_{\mathbf{k}}$ is given by

$$\begin{aligned} \epsilon_{\mathbf{k}}/t &= \sqrt{3 + 2\cos(\mathbf{k}\mathbf{v}_1) + 2\cos(\mathbf{k}\mathbf{v}_2) + 2\cos(\mathbf{k}\mathbf{v}_3)} \\ &= \left[1 + 4\cos\left(\frac{\sqrt{3}}{2}k_y\right) \left(\cos\left(\frac{\sqrt{3}}{2}k_y\right) + \cos\left(\frac{3}{2}k_x\right) \right) \right]^{1/2}. \end{aligned} \quad (\text{B.3})$$

The dispersion $\epsilon_{\mathbf{k},\pm}$ vanishes linearly at the corners $(0, \pm\frac{4\pi}{3\sqrt{3}})$ and $(\pm\frac{2\pi}{3\sqrt{3}}, \pm\frac{2\pi}{3\sqrt{3}})$ of the hexagonal Brillouin zone, at the so-called Dirac points, and forms two Dirac cones since the linear slope is rotationally invariant near the Dirac points.

In order to derive the Kubo formula for the dynamical conductivity we define the charge and current density operators on the honeycomb lattice. The charge density

operators on the A and B sites of the lattice are given by

$$\rho_m^A \equiv \rho(\mathbf{r}_m) = e a_m^\dagger a_m, \quad \rho_m^B \equiv \rho(\mathbf{r}_m + \mathbf{x}) = e b_m^\dagger b_m. \quad (\text{B.4})$$

Three current density operators have to be defined for the different kinds of bonds (Fig. B.1), namely

$$\begin{aligned} j_m^D &= \frac{-i e t}{\hbar} (a_m^\dagger b_m - b_m^\dagger a_m), \\ j_m^E &= \frac{-i e t}{\hbar} (a_{m+\mathbf{v}_2}^\dagger b_m - b_m^\dagger a_{m+\mathbf{v}_2}), \\ j_m^F &= \frac{-i e t}{\hbar} (a_{m+\mathbf{v}_1}^\dagger b_m - b_m^\dagger a_{m+\mathbf{v}_1}). \end{aligned} \quad (\text{B.5})$$

With this choice of operators the continuity equations for the charge density on the A and B sites, respectively, read

$$\dot{\rho}_m^A = -j_m^D - j_{m-\mathbf{v}_2}^E - j_{m-\mathbf{v}_1}^F, \quad \dot{\rho}_m^B = j_m^D + j_m^E + j_m^F. \quad (\text{B.6})$$

In order to derive the Kubo formula for the longitudinal conductivity in the x direction we need to project the current operators j_m^D , j_m^E and j_m^F on the x axis. The projected current density operator reads

$$j_m^x = j_m^D - \frac{1}{2} j_m^E - \frac{1}{2} j_m^F. \quad (\text{B.7})$$

In the next step we couple the system to an external electromagnetic potential Φ such that the corresponding electric field $\mathbf{E}(\mathbf{r}) = -\nabla\Phi(\mathbf{r})$ points along the x direction. After Fourier transformation to \mathbf{q} -space and including a frequency dependence the electric field is thus given by $\mathbf{E}(\mathbf{q}, \omega) = E^x(\mathbf{q}, \omega) \mathbf{e}_x$, where \mathbf{e}_x is a unit vector of length $a_0 = 1$ pointing in x direction. Within linear response theory the current density induced by the electric field is then given by

$$\langle j_{\mathbf{q}}^x(\omega) \rangle = \frac{\langle K^x \rangle + \Lambda_{xx}(\mathbf{q}, \omega)}{i(\omega + i0^+)} E^x(\mathbf{q}, \omega). \quad (\text{B.8})$$

Here $E^x(\mathbf{q}, \omega)$ is the electric field in x direction, and the prefactor

$$\sigma_{xx}(\mathbf{q}, \omega) = \frac{\langle K^x \rangle + \Lambda_{xx}(\mathbf{q}, \omega)}{i(\omega + i0^+)} \quad (\text{B.9})$$

is identified as the \mathbf{q} -dependent dynamical conductivity. Here

$$K^x = \frac{-2te^2}{A_u N \hbar^2} \sum_m (a_m^\dagger b_m + \frac{1}{4}(a_{m+\mathbf{v}_1}^\dagger b_m + a_{m+\mathbf{v}_2}^\dagger b_m) + \text{h.c.}) \quad (\text{B.10})$$

denotes the kinetic energy density operator in x direction and

$$\Lambda_{xx}(\mathbf{q}, \omega) = \frac{2i}{A_u N \hbar} \int_0^\infty dt \langle [j_{x,\mathbf{q}}(t), j_{x,-\mathbf{q}}(0)] \rangle e^{i(\omega + i0^+)t} \quad (\text{B.11})$$

is the current-current correlation function, with N the number of unit cells and $A_u = 3\sqrt{3}a_0^2/2$ the area of the unit cell. The prefactor of 2 in (B.10) and (B.11) accounts for the spin degree of freedom, which was omitted in the Hamiltonian (B.1).

The dynamical conductivity is measured in the long-wavelength limit $\mathbf{q} \rightarrow 0$, $\sigma_{xx}(\omega) = (\langle K^x \rangle + \Lambda_{xx}(\omega)) / (i(\omega + i0^+))$, where

$$\begin{aligned} \Lambda_{xx}(\omega) = \frac{i\text{Re}^2 t^2}{A_u N \hbar^2} \sum_{\mathbf{k}} \left(\delta(\hbar\omega - 2\epsilon_{\mathbf{k}}) - \delta(\hbar\omega + 2\epsilon_{\mathbf{k}}) + \right. \\ \left. + \frac{1}{\hbar\omega + 2\epsilon_{\mathbf{k}}} - \frac{1}{\hbar\omega - 2\epsilon_{\mathbf{k}}} \right) J_{\mathbf{k}}^{x2} g(\epsilon_{\mathbf{k}}) \end{aligned} \quad (\text{B.12})$$

at temperature T and chemical potential μ , and $g(\epsilon) = \tanh[(\epsilon - \mu)/(2k_B T)] + \tanh[(\epsilon + \mu)/(2k_B T)]$. The real part of $\sigma_{xx}(\omega)$ thus has the well-known form expected for a tight-binding model without electron-electron or impurity scattering [214],

$$\text{Re } \sigma_{xx}(\omega) \equiv D \delta(\omega) + \sigma^{\text{reg}}(|\omega|), \quad (\text{B.13})$$

where we have introduced the Drude weight

$$D = \frac{2\pi e^2 t}{A_u N \hbar^2} \sum_{\mathbf{k}} g(\epsilon_{\mathbf{k}}) \left(\xi_{\mathbf{k}}^x - \frac{t J_{\mathbf{k}}^{x2}}{\epsilon_{\mathbf{k}}} \right), \quad (\text{B.14})$$

the regular part (for $\omega > 0$)

$$\sigma^{\text{reg}}(\omega) = \frac{\pi e^2 t^2}{A_u N \hbar^2 \omega} g\left(\frac{\hbar \omega}{2}\right) \sum_{\mathbf{k}} \delta\left(\frac{\hbar \omega}{2} - \epsilon_{\mathbf{k}}\right) J_{\mathbf{k}}^x{}^2, \quad (\text{B.15})$$

and the vertex functions

$$J_{\mathbf{k}}^x = \frac{t}{\epsilon_{\mathbf{k}}} \left(1 + \cos\left(\frac{\sqrt{3}}{2} k_x\right) \cos\left(\frac{1}{2} k_y\right) - 2 \cos^2\left(\frac{1}{2} k_y\right) \right), \quad (\text{B.16})$$

$$\xi_{\mathbf{k}}^x = \frac{t}{\epsilon_{\mathbf{k}}} \left(1 + \frac{5}{2} \cos\left(\frac{\sqrt{3}}{2} k_x\right) \cos\left(\frac{1}{2} k_y\right) + \cos^2\left(\frac{1}{2} k_y\right) \right) \quad (\text{B.17})$$

Interestingly the limits $T \rightarrow 0$ and $\omega \rightarrow 0$ do not commute, because the factor $g(\frac{\hbar \omega}{2})$ in B.15 is nonzero if the limit $T \rightarrow 0$ is taken first but zero if $\omega \rightarrow 0$ is taken first. For the thermodynamic limit we replace the \mathbf{k} -summation by an integral over the Brillouin zone, $\frac{1}{N} \sum_{\mathbf{k}} \rightarrow \int \frac{d^2 k}{F_{\text{BZ}}}$, where $F_{\text{BZ}} = 8\pi^2/(3\sqrt{3})$ is the area of the Brillouin zone. The resulting dynamical conductivity is shown in Fig. B.2.

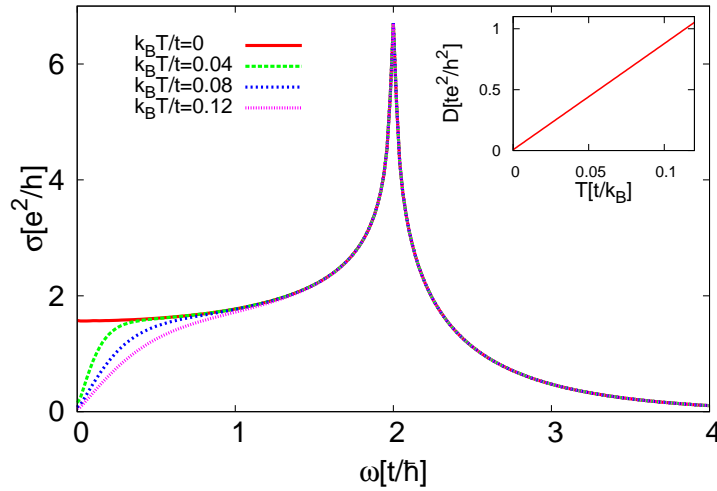


Figure B.2: Regular part of the dynamical conductivity on the honeycomb lattice at the indicated temperatures. At zero temperature the dc limit is $\pi e^2/2h$, whereas it vanishes at finite temperatures. Inset: Temperature dependence of the Drude weight. It vanishes at zero temperature and increases linearly upon an increase in T . Thus the dc conductivity of clean graphene is $\pi e^2/2h$ at $T = 0$, and it is infinite at finite T . Figure created by Armin Seibert.

The dc conductivity of clean graphene at zero temperature, where the Drude weight vanishes, is $\sigma_{\text{dc}} \equiv \sigma^{\text{reg}}(\omega \rightarrow 0)$. In order to compare our result with previous theoretical calculations [163], we calculate the zero-frequency limit of the dynamical conductivity at $T = 0$ analytically from (B.15). This is achieved by expanding the \mathbf{k} -dependent functions $J_{\mathbf{k}}^x$ and $\epsilon_{\mathbf{k}}$ around the Dirac points and performing the integration over the expanded integrand.

Near the Dirac points the dispersion is linearized,

$$\epsilon_{\mathbf{k}_D + \mathbf{p}} \approx \frac{\sqrt{3}}{2} p, \quad (\text{B.18})$$

where \mathbf{k}_D is one of the two Dirac points mentioned below (B.3). The vertex function $J_{\mathbf{k}}^{x2}$ (B.16) is also expanded near the Dirac points,

$$J_{\mathbf{k}_D + \mathbf{p}}^{x2} \approx \frac{4}{3p^2} \frac{27}{16} p_y^2. \quad (\text{B.19})$$

This leads to

$$\sigma^{\text{reg}}(\omega \rightarrow 0) = \frac{6\pi^2 e^2}{h A_u F_{\text{BZ}}} \int_0^{2\pi} d\phi \sin^2 \phi, \quad (\text{B.20})$$

where we have introduced polar coordinates and include a factor of 2 to account for the valley degree of freedom, i.e., the fact that both Dirac points give the same contribution to the conductivity. The zero-frequency limit of the regular part of the conductivity at zero temperature and half-filling is thus given by

$$\sigma_{\text{dc}} \equiv \sigma^{\text{reg}}(\omega \rightarrow 0) = \frac{\pi}{2} \frac{e^2}{h}. \quad (\text{B.21})$$

Note that the dc conductivity has the form $\sigma_{\text{dc}} = g_{\text{dof}}(\pi/8)e^2/h$, with $g_{\text{dof}} = 4$ the number of degrees of freedom (spin and valley degeneracy). Indeed the numerical prefactor $\pi/8$ is universal for non-interacting two-dimensional systems with a linear energy dispersion at low excitation energies. For bosons at the superfluid-insulator transition [215, 216] the same prefactor $\pi/8$ is found within the Gaussian approximation. Similarly for a Heisenberg antiferromagnet with rotationally invariant exchange

Classification	Drude weight D	Localiz. length $\sim \int_0^\infty d\omega \frac{\text{Re } \sigma(\omega)}{\omega}$	$\text{Im } \sigma(\omega),$ $\omega \rightarrow 0^+$	$\text{Re } \epsilon(0^+)$	$\text{Im } \epsilon(0^+)$
Insulator	Zero	Finite	$\sim \omega$	Finite	Zero
Non-Ideal Conductor	Zero	Infinite	$\sim \omega$	Finite	Infinite
Ideal Conductor	Finite	Infinite	$\sim D/\omega$	Infinite	Infinite

Table B.1: Classification of insulators, non-ideal and ideal conductors at $T = 0$ in terms of response functions.

coupling the dc spin conductivity is obtained as $\sigma_s = \pi/8 \times (g\mu_B)^2/h$ within linear spin-wave theory [217].

We also point out that the electrodynamics of non-interacting electrons on the disorder-free honeycomb lattice classifies the system as a non-ideal conductor even though there are no impurities. Consider the local (momentum-integrated) dielectric response function

$$\epsilon(\omega) = 1 + 4\pi i \frac{\sigma(\omega)}{\omega}, \quad (\text{B.22})$$

$$\text{Re } \epsilon(\omega) = 1 - 4\pi \frac{\text{Im } \sigma(\omega)}{\omega}, \quad (\text{B.23})$$

$$\text{Im } \epsilon(\omega) = 4\pi \frac{\text{Re } \sigma(\omega)}{\omega}. \quad (\text{B.24})$$

According to Ref. [218] a generalized scheme for the classification of insulators, non-ideal conductors and conductors is shown in Table B.1. On the honeycomb lattice the Drude weight vanishes at $T = 0$ (see inset in Fig. B.2). At the same time the localization length diverges, since the integral over $\text{Re } \sigma(\omega)/\omega$ diverges due to the finite zero-frequency limit of $\text{Re } \sigma$. Thus the vanishing Drude weight indicates the absence of perfect conduction, yet the quasiparticles are delocalized. Similarly, the dielectric response function shows insulating behavior with a finite real part at zero frequency, but also conducting behavior with a diverging instead of zero imaginary

part. Hence the linear energy dispersion and the two-dimensionality indeed render the system an “in-between” — neither an insulator with a full gap nor a metal.

We now turn to the connection of the above derivation with the calculations presented for disordered graphene in Chapter 7. Starting from the representation of the longitudinal conductivity as a convolution of Green functions [51],

$$\sigma(i\nu) = \frac{2e^2}{\nu\pi\hbar^2} \int_{-\infty}^{\infty} d\epsilon \tilde{\rho}(\epsilon) T \sum_n [G_{\epsilon}(i\omega_n + i\nu) + G_{-\epsilon}(i\omega_n + i\nu)] G_{\epsilon}(i\omega_n), \quad (\text{B.25})$$

which is valid for non-interacting electrons described by a tight-binding model or for interacting electrons if vertex corrections may be neglected. Here we have already assumed the band structure of graphene, with the valence and conduction bands as introduced in Chapter 7 and $\tilde{\rho}(\epsilon) = \sum_{\mathbf{k}} (\partial\epsilon_{\mathbf{k}}/\partial k_x)^2 \delta(\epsilon - \epsilon_{\mathbf{k}}) \approx \hbar|\epsilon|/2\pi$ for $|\epsilon| < \epsilon_{\max}$ in the Dirac cone approximation, where ϵ_{\max} is a cutoff energy on the order of the half-bandwidth of graphene. Analytical continuation of Eq. (B.25) leads to

$$\text{Re } \sigma(\omega) = \frac{2\pi e^2}{\hbar^2} \int_{-\infty}^{\infty} d\epsilon \tilde{\rho}(\epsilon) \int_{-\infty}^{\infty} d\nu [A_{\epsilon}(\nu + \omega) + A_{-\epsilon}(\nu + \omega)] A_{\epsilon}(\nu) \frac{f_{\nu-\mu} - f_{\omega+\nu-\mu}}{\omega}. \quad (\text{B.26})$$

where $f_x = (1 + \exp(x/T))$ is the Fermi-Dirac distribution function ($k_B = 1$) and μ is the chemical potential. In the dc limit ($\omega \rightarrow 0$), one directly obtains Eq. (7.1),

$$\sigma_{\text{dc}} = \frac{2\pi e^2}{\hbar^2} \int_{-\infty}^{\infty} d\nu \int_{-\infty}^{\infty} d\epsilon \tilde{\rho}(\epsilon) [A_{\epsilon}(\nu) + A_{-\epsilon}(\nu)] A_{\epsilon}(\nu) \frac{-df_x}{dx} \Big|_{x=\nu-\mu}. \quad (\text{B.27})$$

We now show the equivalence of Eq. (B.13) and Eq. (B.26), considering the intraband ($A_{\epsilon}(\nu + \omega)A_{\epsilon}(\nu)$) and interband ($A_{-\epsilon}(\nu + \omega)A_{\epsilon}(\nu)$) contributions separately.

The intraband contribution for clean graphene ($A_\epsilon(\nu) = \delta(\epsilon - \nu)$) is given by

$$\begin{aligned} \text{Re } \sigma_{\text{intra}}(\omega) &= \frac{2\pi e^2}{\hbar^2} \int_{-\infty}^{\infty} d\epsilon \tilde{\rho}(\epsilon) \int_{-\infty}^{\infty} d\nu \delta(\epsilon - \nu - \omega) \delta(\epsilon - \nu) \frac{f_{\nu-\mu} - f_{\omega+\nu-\mu}}{\omega} \\ &= \frac{2\pi e^2}{\hbar^2} \int_{-\infty}^{\infty} d\epsilon \tilde{\rho}(\epsilon) \frac{-df(\epsilon - \mu)}{d\epsilon} \delta(\omega), \end{aligned} \quad (\text{B.28})$$

which is of the form $D\delta(\omega)$ with the Drude weight D given by a formula equivalent to Eq. (B.14). Within the Dirac cone approximation the linearization of $\tilde{\rho}(\epsilon)$ amounts to linearizing the dispersion according to Eq. (B.18) and approximating the vertex function appearing in Eq. (B.14) according to Eq. (B.19). Similarly, the interband contribution is given by

$$\begin{aligned} \text{Re } \sigma_{\text{inter}}(\omega) &= \frac{2\pi e^2}{\hbar^2} \int_{-\infty}^{\infty} d\epsilon \tilde{\rho}(\epsilon) \int_{-\infty}^{\infty} d\nu \delta(-\epsilon - \nu - \omega) \delta(\epsilon - \nu) \frac{f_{\nu-\mu} - f_{\omega+\nu-\mu}}{\omega} \\ &= \frac{2\pi e^2}{\hbar^2} \int_{-\infty}^{\infty} d\epsilon \tilde{\rho}(\epsilon) \frac{f(\epsilon - \mu) - f(\omega + \epsilon - \mu)}{\omega} \delta(\omega - 2\epsilon), \end{aligned} \quad (\text{B.29})$$

in equivalence to Eq. (B.15) for the regular part of the conductivity. In particular, using $\tilde{\rho}(\epsilon) \approx \hbar|\epsilon|/2\pi$ and taking the dc limit at $T = 0$ one directly obtains $\sigma_{\text{dc}} = \pi e^2/2h$ in accordance with Eq. (B.21).

Obviously the intraband excitations give rise to the Drude-like contribution leading to an infinite dc conductivity in a perfect conductor. The interband excitations appear in a two-band system, like in graphene, and lead to its visual transparency, for example. For the dc transport in disordered graphene, as discussed in Chapter 7, both contributions become important at low temperatures and near half-filling, i.e., at low densities. However, at high temperatures and high densities dc transport is governed by intraband excitations solely. The introduced classification into valence and conduction bands thus provides a useful terminology, even though it may be

uncommon to deal with bands which are not differentiable manifolds, at least at the Dirac points.

Bibliography

- [1] R.O. Jones, O. Gunnarsson, Rev. Mod. Phys. **61**, 689 (1989)
- [2] M.C. Gutzwiller, Phys. Rev. Lett. **10**, 159 (1963)
- [3] J. Hubbard, Proc. R. Soc. A **276**, 238 (1963)
- [4] J. Kanamori, Prog. Theor. Phys. **30**, 257 (1963)
- [5] M. Imada, A. Fujimori, Y. Tokura, Rev. Mod. Phys. **70**, 1039 (1998)
- [6] W. Metzner, D. Vollhardt, Phys. Rev. Lett. **62**, 324 (1989)
- [7] A. Georges, G. Kotliar, Phys. Rev. B **45**, 6479 (1992)
- [8] A. Georges, G. Kotliar, W. Krauth, M.J. Rozenberg, Rev. Mod. Phys. **68**, 13 (1996)
- [9] V.I. Anisimov, A.I. Poteryaev, M.A. Korotin, A.O. Anokhin, G. Kotliar, J. Phys. Condens. Matter **9**, 7359 (1997)
- [10] K. Held, I.A. Nekrasov, G. Keller, V. Eyert, N. Blümer, A.K. McMahan, R.T. Scalettar, T. Pruschke, V.I. Anisimov, D. Vollhardt, Phys. Status Solidi B **243**, 2599 (2006)
- [11] L.D. Landau, Zh. Eksp. Theor. Fiz. **30**, 1058 (1956)
- [12] L.D. Landau, Zh. Eksp. Theor. Fiz. **32**, 59 (1957)

-
- [13] D. Vollhardt, Rev. Mod. Phys. **56**, 99 (1984)
 - [14] G.R. Stewart, Rev. Mod. Phys. **56**, 755 (1984)
 - [15] N.W. Ashcroft, N.D. Mermin, *Solid State Physics* (Brooks Cole, 1976)
 - [16] A.B. Harris, A.V. Lange, Phys. Rev. **157**, 295 (1967)
 - [17] F. Dyson, E.H. Lieb, B. Simon, J. Stat. Phys. **18**, 335 (1978)
 - [18] T. Kennedy, E.H. Lieb, B.S. Shastry, J. Stat. Phys. **53**, 1019 (1988)
 - [19] P.C. Hohenberg, Phys. Rev. **158**, 383 (1967)
 - [20] N.D. Mermin, H. Wagner, Phys. Rev. Lett. **17**, 1133 (1969)
 - [21] S. Chakravarty, B.I. Halperin, D.R. Nelson, Phys. Rev. B **39**, 2344 (1989)
 - [22] E. Manousakis, Rev. Mod. Phys. **63**, 1 (1991)
 - [23] R. Zitzler, *Magnetic Properties of the One-Band Hubbard Model* (PhD Thesis, Universität Augsburg, 2004)
 - [24] M. Eckstein, M. Kollar, M. Potthoff, D. Vollhardt, Phys. Rev. B **75**, 125103 (2007)
 - [25] R.W. Helmes, *Dynamical Mean Field Theory of inhomogeneous correlated systems* (PhD Thesis, Universität zu Köln, 2008)
 - [26] S.R. White, D.J. Scalapino, Phys. Rev. Lett. **81**, 3227 (1998)
 - [27] Y. Nagaoka, Phys. Rev. **147**, 392 (1966)
 - [28] H. Park, K. Haule, C.A. Marianetti, G. Kotliar, Phys. Rev. B **77**, 035107 (2008)
 - [29] A.I. Lichtenstein, M.I. Katsnelson, Phys. Rev. B **62**, R9283 (2000)

-
- [30] T.A. Maier, M. Jarrell, T.C. Schulthess, P.R.C. Kent, J.B. White, Phys. Rev. Lett. **95**, 237001 (2005)
- [31] H. Alloul, T. Ohno, P. Mendels, Phys. Rev. Lett. **63**, 1700 (1989)
- [32] C. Renner, B. Revaz, J.Y. Genoud, K. Kadowaki, O. Fischer, Phys. Rev. Lett. **80**, 149 (1998)
- [33] P.W. Anderson, Science **235**, 1196 (1987)
- [34] Z.Y. Meng, T.C. Lang, S. Wessel, F.F. Assaad, A. Muramatsu, Nature **464**, 847 (2010)
- [35] M. Jarrell, Phys. Rev. Lett. **69**, 168 (1992)
- [36] J. Kuneš, I. Leonov, M. Kollar, K. Byczuk, V.I. Anisimov, D. Vollhardt, Eur. Phys. J. Special Topics **180**, 5 (2010)
- [37] E. Gull, *Continuous-Time Quantum Monte Carlo Algorithms for Fermions* (PhD Thesis, ETH Zürich, 2008)
- [38] V.S. Oudovenko, G. Pálsson, K. Haule, G. Kotliar, S.Y. Savrasov, Phys. Rev. B **73**, 035120 (2006)
- [39] M. Jarrell, J.E. Gubernatis, Phys. Rep. **269**, 133 (1996)
- [40] C.J. Halboth, W. Metzner, Phys. Rev. B **61**, 7364 (2000)
- [41] T.A. Maier, M. Jarrell, T. Pruschke, M.H. Hettler, Rev. Mod. Phys. **77**, 1027 (2005)
- [42] A. Toschi, A.A. Katanin, K. Held, Phys. Rev. B **75**, 045118 (2007)

-
- [43] A.N. Rubtsov, M.I. Katsnelson, A.I. Lichtenstein, Phys. Rev. B **77**, 033101 (2008)
 - [44] A.N. Rubtsov, M.I. Katsnelson, A.I. Lichtenstein, A. Georges, Phys. Rev. B **79**, 045133 (2009)
 - [45] E. Kozik, K.V. Houcke, E. Gull, L. Pollet, N. Prokof'ev, B. Svistunov, M. Troyer, arXiv:0907.0863
 - [46] K. Held, A.A. Katanin, A. Toschi, Prog. Theor. Phys. Suppl. **176**, 117 (2008)
 - [47] R. Bulla, T.A. Costi, T. Pruschke, Rev. Mod. Phys. **80**, 395 (2008)
 - [48] H. Park, K. Haule, G. Kotliar, Phys. Rev. Lett. **101**, 186403 (2008)
 - [49] M. Balzer, B. Kyung, D. Sénéchal, A.M.S. Tremblay, M. Potthoff, Europhys. Lett. **85**, 17002 (2009)
 - [50] E. Gull, P. Werner, X. Wang, M. Troyer, A.J. Millis, Europhys. Lett. **84**, 37009 (2008)
 - [51] N. Blümer, *Mott-Hubbard Metal-Insulator Transition and Optical Conductivity in High Dimensions* (PhD Thesis, Universität Augsburg, 2002)
 - [52] R. Bulla, T.A. Costi, D. Vollhardt, Phys. Rev. B **64**, 045103 (2001)
 - [53] M. Imada, T. Misawa, Y. Yamaji, J. Phys. Condens. Matter **22**, 164206 (2010)
 - [54] I. Dzyaloshinskii, Phys. Rev. B **68**, 085113 (2003)
 - [55] R.M. Konik, T.M. Rice, A.M. Tsvelik, Phys. Rev. Lett. **96**, 086407 (2006)
 - [56] K.Y. Yang, T.M. Rice, F.C. Zhang, Phys. Rev. B **73**, 174501 (2006)
 - [57] T.D. Stanescu, G. Kotliar, Phys. Rev. B **74**, 125110 (2006)

- [58] F. Kagawa, K. Miyagawa, K. Kanoda, *Nature* **436**, 534 (2005)
- [59] F. Kagawa, K. Miyagawa, K. Kanoda, *Nature Phys.* **5**, 880 (2009)
- [60] D.J. Scalapino, *Phys. Rep.* **250**, 329 (1995)
- [61] J. Bardeen, L.N. Cooper, J.R. Schrieffer, *Phys. Rev.* **108**, 1175 (1957)
- [62] J.R. Schrieffer, *Theory of Superconductivity* (Perseus Books; Revised edition, 1999)
- [63] F. Loder, private communication
- [64] D.J. Scalapino, *Numerical Studies of the 2D Hubbard Model (Chapter 13 in the “Handbook of High Temperature Superconductivity”)* (Springer, New York, 2007)
- [65] S. Sorella, G. Martins, R. Becca, C. Gazza, L. Capriotti, A. Parola, E. Dagotto, *Phys. Rev. Lett.* **88**, 117002 (2002)
- [66] C. Dahnken, M. Potthoff, E. Arrigoni, W. Hanke, *Low Temp. Phys.* **32**, 457 (2006)
- [67] S.S. Kancharla, B. Kyung, D. Sénéchal, M. Civelli, M. Capone, G. Kotliar, A.M.S. Tremblay, *Phys. Rev. B* **77**, 184516 (2008)
- [68] M. Aichhorn, E. Arrigoni, M. Potthoff, W. Hanke, *Phys. Rev. B* **74**, 024508 (2006)
- [69] C. Huscroft, M. Jarrell, T.A. Maier, S. Moukouri, A.N. Tahvildarzadeh, *Phys. Rev. Lett.* **86**, 139 (2001)
- [70] A. Macridin, M. Jarrell, T.A. Maier, P.R.C. Kent, E. D’Azevedo, *Phys. Rev. Lett.* **97**, 036401 (2006)

-
- [71] B. Kyung, V. Hankevych, A.M. Dare, A.M.S. Tremblay, Phys. Rev. Lett. **93**, 147004 (2004)
- [72] B. Kyung, S.S. Kancharla, D. Sénéchal, A.M.S. Tremblay, M. Civelli, G. Kotliar, Phys. Rev. B **73**, 165114 (2006)
- [73] D. Duffy, A. Moreo, Phys. Rev. B **52**, 15607 (1995)
- [74] D. Duffy, A. Moreo, Phys. Rev. B **55**, 676 (1997)
- [75] J. Reiss, D. Rohe, W. Metzner, Phys. Rev. B **75**, 075110 (2007)
- [76] H. Yokoyama, M. Ogata, Y. Tanaka, J. Phys. Soc. Jpn. **75**, 114706 (2006)
- [77] N.E. Bickers, D.J. Scalapino, S.R. White, Phys. Rev. Lett. **62**, 961 (1989)
- [78] N.E. Bickers, S.R. White, Phys. Rev. B **43**, 8044 (1990)
- [79] N. Grewe, Z. Phys. B **53**, 271 (1983)
- [80] H. Keiter, G. Czyczoll, J. Magn. Magn. Mater. **31**, 477 (1983)
- [81] H. Keiter, J. Kimball, Int. J. Magn. **1**, 233 (1971)
- [82] Y. Kuramoto, Z. Phys. B: Condens. Matter **53**, 37 (1983)
- [83] J.E. Hirsch, R.M. Fye, Phys. Rev. Lett. **56**, 2521 (1986)
- [84] A.N. Rubtsov, V.V. Savkin, A.I. Lichtenstein, Phys. Rev. B **72**, 035122 (2005)
- [85] P. Werner, A. Comanac, L. de' Medici, M. Troyer, A.J. Millis, Phys. Rev. Lett. **97**, 076405 (2006)
- [86] R. Haydock, V. Heine, M.J. Kelly, J. Phys. C **8**, 2591 (1975)
- [87] K.G. Wilson, Rev. Mod. Phys. **47**, 773 (1975)

- [88] H. Krishnamurthy, J. Wilkins, K.G. Wilson, Phys. Rev. B **21**, 1003 (1980)
- [89] H. Krishnamurthy, J. Wilkins, K.G. Wilson, Phys. Rev. B **21**, 1044 (1980)
- [90] S.R. White, Phys. Rev. Lett. **69**, 2863 (1992)
- [91] E. Gull, A.J. Millis, A.I. Lichtenstein, A.N. Rubtsov, M. Troyer, P. Werner, unpublished
- [92] N. Blümer, arXiv:0801.1222
- [93] E. Gull, P. Werner, A.J. Millis, M. Troyer, Phys. Rev. B **76**, 235123 (2007)
- [94] M. Troyer, B. Ammon, E. Heeb, Lect. Notes Comput. Sci. **1505**, 191 (1998)
- [95] F. Alet, P. Dayal, A. Grzesik, A. Honecker, M. Körner, A. Läuchli, S.R. Manmana, I.P. McCulloch, F. Michel, R.M. Noack, G. Schmid, U. Schollwöck, F. Stöckli, S. Todo, S. Trebst, M. Troyer, P. Werner, S. Wessel, J. Phys. Soc. Jpn. Suppl. **74**, 30 (2005)
- [96] K. Haule, G. Kotliar, Phys. Rev. B **76**, 104509 (2007)
- [97] M. Sentef, J. Kuneš, P. Werner, A.P. Kampf, Phys. Rev. B **80**, 155116 (2009)
- [98] A.P. Kampf, M. Kollar, J. Kuneš, M. Sentef, D. Vollhardt, arXiv:0910.5126 (accepted for publication in "High Performance Computing in Science and Engineering, Garching 2009" (Springer))
- [99] C.L. Kane, E.J. Mele, Phys. Rev. Lett. **95**, 146802 (2005)
- [100] A.P. Kampf, M. Sekania, G.I. Japaridze, P. Brune, J. Phys. Condens. Matter **15**, 5895 (2003)

-
- [101] S.R. Manmana, V. Meden, R.M. Noack, K. Schönhammer, Phys. Rev. B **70**, 155115 (2004)
 - [102] C.D. Batista, A.A. Aligia, Phys. Rev. Lett. **92**, 246405 (2004)
 - [103] A. Garg, H.R. Krishnamurthy, M. Randeria, Phys. Rev. Lett. **97**, 046403 (2006)
 - [104] S.S. Kancharla, E. Dagotto, Phys. Rev. Lett. **98**, 016402 (2007)
 - [105] N. Paris, K. Bouadim, F. Hebert, G.G. Batrouni, R.T. Scalettar, Phys. Rev. Lett. **98**, 046403 (2007)
 - [106] L. Craco, P. Lombardo, R. Hayn, G.I. Japaridze, E. Müller-Hartmann, Phys. Rev. B **78**, 075121 (2008)
 - [107] K. Byczuk, M. Sekania, W. Hofstetter, A.P. Kampf, Phys. Rev. B **79**, 121103(R) (2009)
 - [108] J. Kuneš, V.I. Anisimov, Phys. Rev. B **78**, 033109 (2008)
 - [109] A. Shitade, H. Katsura, J. Kuneš, X.L. Qi, S.C. Zhang, N. Nagaosa, Phys. Rev. Lett. **102**, 256403 (2009)
 - [110] P. Werner, A.J. Millis, Phys. Rev. Lett. **99**, 126405 (2007)
 - [111] G. Moeller, V. Dobrosavljević, A.E. Ruckenstein, Phys. Rev. B **59**, 6846 (1999)
 - [112] A. Fuhrmann, D. Heilmann, H. Monien, Phys. Rev. B **73**, 245118 (2006)
 - [113] S.S. Kancharla, S. Okamoto, Phys. Rev. B **75**, 193103 (2007)
 - [114] M. Fabrizio, Phys. Rev. B **76**, 165110 (2007)
 - [115] H. Hafermann, M.I. Katsnelson, A.I. Lichtenstein, Europhys. Lett. **85**, 37006 (2009)

-
- [116] E. Müller-Hartmann, Z. Phys. B **74**, 507 (1989)
 - [117] F.D.M. Haldane, Phys. Rev. Lett. **61**, 2015 (1988)
 - [118] M. Jarrell, J.E. Gubernatis, Phys. Rep. **269**, 133 (1996)
 - [119] D. Ruhl, F. Gebhard, J. Stat. Mech. Exp. Theor. p. P03015 (2006)
 - [120] Z. Schlesinger, Z. Fisk, H.T. Zhang, M.B. Maple, Physica B **237-238**, 460 (1997)
 - [121] A. Severing, J.D. Thompson, P.C. Canfield, Z. Fisk, P. Riseborough, Phys. Rev. B **44**, 6832 (1991)
 - [122] B. Bucher, Z. Schlesinger, P.C. Canfield, Z. Fisk, Phys. Rev. Lett. **72**, 522 (1994)
 - [123] D. Menzel, P. Popovich, N.N. Kovaleva, J. Schoenes, K. Doll, A.V. Boris, Phys. Rev. B **79**, 165111 (2009)
 - [124] J.M. Tomczak, K. Haule, T. Miyake, A. Georges, G. Kotliar, arXiv:1006.0564
 - [125] C.M. Varma, Phys. Rev. Lett. **83**, 3538 (1999)
 - [126] S. Chakravarty, R.B. Laughlin, D.K. Morr, C. Nayak, Phys. Rev. B **63**, 094503 (2001)
 - [127] N.S. Vidhyadhiraja, A. Macridin, C. Sen, M. Jarrell, M. Ma, Phys. Rev. Lett. **102**, 206407 (2009)
 - [128] C. Honerkamp, M. Salmhofer, N. Furukawa, T.M. Rice, Phys. Rev. B **63**, 035109 (2001)
 - [129] A.A. Katanin, A.P. Kampf, Phys. Rev. Lett. **93**, 106406 (2004)

-
- [130] D. Rohe, W. Metzner, Phys. Rev. B **71**, 115116 (2005)
 - [131] M. Capone, G. Kotliar, Phys. Rev. B **74**, 054513 (2006)
 - [132] N. Lin, E. Gull, A.J. Millis, arXiv:1004.2999
 - [133] E. Gull, M. Ferrero, O. Parcollet, A. Georges, A.J. Millis, arXiv:1007.2592
 - [134] H.Q. Lin, J.E. Hirsch, Phys. Rev. B **35**, 3359 (1987)
 - [135] S. Schmitt, arXiv:1005.3481
 - [136] G. Kotliar, S.Y. Savrasov, G. Palsson, G. Biroli, Phys. Rev. Lett. **87**, 186401 (2001)
 - [137] K. Haule, Phys. Rev. B **75**, 155113 (2007)
 - [138] E. Gull, O. Parcollet, P. Werner, A.J. Millis, Phys. Rev. B **80**, 245102 (2009)
 - [139] W. Hofstetter, D. Vollhardt, Ann. Phys. **7**, 48 (1998)
 - [140] E. Khatami, K. Mielson, D. Galanakis, A. Macridin, J. Moreno, R.T. Scalettar, M. Jarrell, Phys. Rev. B **81**, 201101(R) (2010)
 - [141] M. Dumm, D. Faltermeier, N. Drichko, M. Dressel, C. Mézière, P. Batail, Phys. Rev. B **79**, 195106 (2009)
 - [142] H. Kino, H. Fukuyama, J. Phys. Soc. Jpn. **65**, 2158 (1996)
 - [143] C. Castellani, C.D. Castro, D. Feinberg, J. Ranninger, Phys. Rev. Lett. **43**, 1957 (1979)
 - [144] G. Kotliar, E. Lange, M.J. Rozenberg, Phys. Rev. Lett. **84**, 5180 (2000)
 - [145] S. Onoda, N. Nagaosa, J. Phys. Soc. Jpn. **72**, 2445 (2003)

-
- [146] S. Papanikolaou, R.M. Fernandes, E. Fradkin, P.W. Phillips, J. Schmalian, R. Sknepnek, Phys. Rev. Lett. **100**, 026408 (2008)
- [147] P. Limelette, A. Georges, D. Jérôme, P. Wzietek, P. Metcalf, J.M. Honig, Science **302**, 89 (2003)
- [148] B.M. McCoy, T.T. Wu, *The Two-Dimensional Ising Model* (Harvard University, Cambridge, 1973)
- [149] M. Imada, Phys. Rev. B **72**, 075113 (2005)
- [150] M. de Souza, A. Brühl, C. Strack, B. Wolf, D. Schweitzer, M. Lang, Phys. Rev. Lett. **99**, 037003 (2007)
- [151] L. Bartosch, M. de Souza, M. Lang, arXiv:1004.4898
- [152] H.C. Kandpal, I. Opahle, Y.Z. Zhang, H.O. Jeschke, R. Valenti, Phys. Rev. Lett. **103**, 067004 (2009)
- [153] B. Kyung, A.M.S. Tremblay, Phys. Rev. Lett. **97**, 046402 (2006)
- [154] T. Ohashi, T. Momoi, H. Tsunetsugu, N. Kawakami, Phys. Rev. Lett. **100**, 076402 (2008)
- [155] A.K. Geim, K.S. Novoselov, Nat. Mater. **6**, 183 (2007)
- [156] Y.W. Tan, Y. Zhang, K. Bolotin, Y. Zhao, S. Adam, E.H. Hwang, S. Das Sarma, H.L. Stormer, P. Kim, Phys. Rev. Lett. **99**, 246803 (2007)
- [157] S.V. Morozov, K.S. Novoselov, M.I. Katsnelson, F. Schedin, D.C. Elias, J.A. Jaszczak, A.K. Geim, Phys. Rev. Lett. **100**, 016602 (2008)
- [158] K.I. Bolotin, K.J. Sikes, Z. Jiang, M. Klima, G. Fudenberg, J. Hone, P. Kim, H. Stormer, Solid State Commun. **146**, 351 (2008)

-
- [159] A.K. Geim, <http://meetings.aps.org/link/BAPS.2010.MAR.J21.4> (2010)
- [160] X. Du, I. Skachko, A. Barker, E.Y. Andrei, *Nature Nanotech.* **3**, 491 (2008)
- [161] K.I. Bolotin, K.J. Sikes, J. Hone, H.L. Stormer, P. Kim, *Phys. Rev. Lett.* **101**, 096802 (2008)
- [162] K. Ziegler, *Phys. Rev. B* **75**, 233407 (2007)
- [163] T. Stauber, N.M.R. Peres, A.K. Geim, *Phys. Rev. B* **78**, 085432 (2008)
- [164] M. Lewkowicz, B. Rosenstein, *Phys. Rev. Lett.* **102**, 106802 (2009)
- [165] A.H. Castro Neto, F. Guinea, N.M.R. Peres, K.S. Novoselov, A.K. Geim, *Rev. Mod. Phys.* **81**, 109 (2009)
- [166] R.R. Nair, P. Blake, A.N.G. and K. S. Novoselov, T.J. Booth, T. Stauber, N.M.R. Peres, A.K. Geim, *Science* **320**, 1308 (2008)
- [167] K.S. Novoselov, A.K. Geim, S.V. Morozov, D. Jiang, M.I. Katsnelson, I.V. Grigorieva, S.V. Dubonos, A.A. Firsov, *Nature* **438**, 197 (2005)
- [168] Y. Zhang, Y. Tan, H. Stormer, P. Kim, *Nature* **438**, 201 (2005)
- [169] J. Martin, N. Akerman, G. Ulbricht, T. Lohmann, J.H. Smet, K. von Klitzing, A. Yacoby, *Nature Phys.* **4**, 144 (2008)
- [170] Y. Zhang, V.W. Brar, C. Girit, A. Zettl, M.F. Crommie, *Nature Phys.* **5**, 722 (2009)
- [171] F. Guinea, M.I. Katsnelson, M.A.H. Vozmediano, *Phys. Rev. B* **77**, 075422 (2008)

-
- [172] J.C. Meyer, A.K. Geim, M.I. Katsnelson, K.S. Novoselov, T.J. Booth, S. Roth, Nat. Lett. **446**, 60 (2007)
- [173] A. Fasolino, J.H. Los, M.I. Katsnelson, Nat. Mat. Lett. **6**, 858 (2007)
- [174] M.I. Katsnelson, A.K. Geim, Phil. Trans. R. Soc. A **366**, 195 (2008)
- [175] L. Brey, J.J. Palacios, Phys. Rev. B **77**, 041403 (2008)
- [176] P. Blake, R. Yang, S.V. Morozov, F. Schedin, L.A. Ponomarenko, A.A. Zhukov, R.R. Nair, I.V. Grigorieva, K.S. Novoselov, A.K. Geim, Solid State Commun. **149**, 1068 (2009)
- [177] S. Adam, E.H. Hwang, E. Rossi, S. Das Sarma, Solid State Commun. **149**, 1072 (2009)
- [178] S. Das Sarma, S. Adam, E.H. Hwang, E. Rossi, arXiv:1003.4731
- [179] S. Adam, P.W. Brouwer, S. Das Sarma, Phys. Rev. B **79**, 201404(R) (2009)
- [180] M. Müller, M. Bräuninger, B. Trauzettel, Phys. Rev. Lett. **103**, 196801 (2009)
- [181] S. Adam, M.D. Stiles, arXiv:0912.1606
- [182] E. Fradkin, Phys. Rev. B **33**, 3257 (1986)
- [183] A.W.W. Ludwig, M.P.A. Fisher, R. Shankar, G. Grinstein, Phys. Rev. B **50**, 7526 (1994)
- [184] M.I. Katsnelson, Eur. Phys. J. B **51**, 157 (2006)
- [185] J. Tworzydło, B. Trauzettel, M. Titov, A. Rycerz, C.W.J. Beenakker, Phys. Rev. Lett. **96**, 246802 (2006)
- [186] N.M.R. Peres, F. Guinea, A.H. Castro Neto, Phys. Rev. B **73**, 125411 (2006)

-
- [187] D.W. Taylor, Phys. Rev. **156**, 1017 (1967)
- [188] P. Soven, Phys. Rev. **156**, 809 (1967)
- [189] T. Pruschke, D.L. Cox, M. Jarrell, Phys. Rev. B **47**, 3553 (1993)
- [190] M.J. Rozenberg, G. Kotliar, H. Kajueter, G.A. Thomas, D.H. Rapkine, J.M. Honig, P. Metcalf, Phys. Rev. Lett. **75**, 105 (1995)
- [191] P.W. Anderson, Phys. Rev. **109**, 1492 (1958)
- [192] D. Vollhardt, P. Wölfle, Phys. Rev. B **22**, 4666 (1980)
- [193] S.V. Morozov, K.S. Novoselov, M.I. Katsnelson, F. Schedin, L.A. Ponomarenko, D. Jiang, A.K. Geim, Phys. Rev. Lett. **97**, 016801 (2006)
- [194] K. Wakabayashi, Y. Takane, M. Sigrist, Phys. Rev. Lett. **99**, 036601 (2007)
- [195] K. Ziegler, Phys. Rev. Lett. **100**, 168801 (2008)
- [196] R.J. Elliott, J.A. Krumhansl, P.L. Leath, Rev. Mod. Phys. **46**, 465 (1974)
- [197] C. Coletti, C. Riedl, D.S. Lee, B. Krauss, L. Patthey, K. von Klitzing, J.H. Smet, U. Starke, Phys. Rev. B **81**, 235401 (2010)
- [198] C. Weber, K. Haule, G. Kotliar, Nature Phys. **advance online publication**, (2010). URL <http://dx.doi.org/10.1038/nphys1706>
- [199] K. Segawa, M. Kofu, S.H. Lee, I. Tsukada, H. Hiraka, M. Fujita, S. Chang, K. Yamada, Y. Ando, Nature Phys. **advance online publication**, (2010). URL <http://dx.doi.org/10.1038/nphys1717>
- [200] P.W. Anderson, Nature Phys. **2**, 626 (2006)
- [201] I. Bloch, J. Dalibard, W. Zwerger, Rev. Mod. Phys. **80**, 885 (2008)

-
- [202] J.P. Gaebler, J.T. Stewart, T.E. Drake, D.S. Jin, A. Perali, P. Pieri, G.C. Strinati, Nature Phys. **advance online publication**, (2010). URL <http://dx.doi.org/10.1038/nphys1709>
- [203] D.J. Scalapino, <http://adsabs.harvard.edu/abs/2010APS..MARD39001S> (2010)
- [204] I. Mazin, J. Schmalian, Physica C: Superconductivity **469**, 614 (2009)
- [205] H. Sakakibara, H. Usui, K. Kuroki, R. Arita, H. Aoki, arXiv:1003.1770
- [206] W.C. Lee, S.C. Zhang, C. Wu, Phys. Rev. Lett. **102**, 217002 (2009)
- [207] S. Sachdev, R.N. Bhatt, Phys. Rev. B **41**, 9323 (1989)
- [208] K. Park, S. Sachdev, Phys. Rev. B **64**, 184510 (2001)
- [209] J.K. Freericks, *Transport in Multilayered Nanostructures: The Dynamical Mean-Field Theory Approach* (Imperial College Press, London, 2006)
- [210] R.W. Helmes, T.A. Costi, A. Rosch, Phys. Rev. Lett. **101**, 066802 (2008)
- [211] S. Okamoto, A.J. Millis, Phys. Rev. B **70**, 241104(R) (2004)
- [212] S. Thiel, G. Hammerl, A. Schmehl, C.W. Schneider, J. Mannhart, Science **313**, 1942 (2006)
- [213] J. Mannhart, D.G. Schlom, Science **327**, 1607 (2010)
- [214] D.J. Scalapino, S.R. White, S.C. Zhang, Phys. Rev. B **47**, 7995 (1993)
- [215] M.P.A. Fisher, P.B. Weichman, G. Grinstein, D.S. Fisher, Phys. Rev. B **40**, 546 (1989)
- [216] A.P. Kampf, G.T. Zimanyi, Phys. Rev. B **47**, 279 (1993)

[217] M. Sentef, M. Kollar, A.P. Kampf, Phys. Rev. B **75**, 214403 (2007)

[218] I. Souza, T. Wilkens, R.M. Martin, Phys. Rev. B **62**, 1666 (2000)

Danksagung

Mein Dank gilt an erster Stelle Prof. Dr. Arno Kampf für seine fortwährende Unterstützung, die Betreuung meiner Arbeit, die regelmäßigen und sehr hilfreichen Diskussionen und das kritische Hinterfragen und Abklopfen meiner Ergebnisse auf ihren physikalischen Kern.

Ebenso danke ich Prof. Dr. Dieter Vollhardt für seine Unterstützung, die kritischen und hilfreichen Anregungen bei meinen Vorträgen und für das motivierende Arbeitsumfeld an seinem Lehrstuhl.

Dank sagen möchte ich an dieser Stelle auch Jan Kuneš, von dem ich vieles über numerische Simulationen mit DMFT gelernt habe. Herzlichen Dank auch an Philipp Werner, ohne dessen Unterstützung in numerischen Fragen und im Verständnis der QMC diese Arbeit nicht möglich gewesen wäre. Ihm danke ich auch für seine Einladungen an die ETH Zürich, für die anregenden Diskussionen bei meinen Besuchen und die fruchtbare Zusammenarbeit. Mein Dank für prompte und unkomplizierte Hilfestellung bei der Numerik gilt ebenso Emanuel Gull, dessen Expertise in Sachen QMC für mich sehr hilfreich war.

Bei meinen Lehrstuhlkollegen bedanke ich mich für die angenehme und kooperative Arbeitsatmosphäre, viele Anregungen und Diskussionen und nicht zuletzt für unsere (manchmal) guten Teamleistungen bei den Fußballturnieren. Ganz besonderer Dank gilt unseren Sekretärinnen Frau Besslich und Frau Seidl für ihre stets prompte Hilfe bei allen organisatorischen Dingen und für freundliche und aufmunternde

Gespräche jenseits des Fachlichen.

Für ihre Anregungen und Kommentare zu dieser Arbeit und das sorgfältige Korrekturlesen danke ich ganz herzlich Wolfgang Krätschmer, Marcus Kollar und Siegfried Graser. Bei Prof. Dr. Thilo Kopp bedanke ich mich für die Übernahme des Zweitgutachtens zu dieser Arbeit. Dank gilt auch der Studienstiftung des deutschen Volkes für die finanzielle Unterstützung durch ein Promotionsstipendium sowie meinem Vertrauensdozenten Prof. Dr. Christoph Becker für seinen freundschaftlichen Rat.

Zuletzt möchte ich den Menschen danken, die mir mit ihrem Vertrauen und ihrer Verbundenheit immer die nötige Kraft zum Weitermachen gegeben haben: meinen Eltern Roswitha und Franz Sentef, meiner Tante Anna Sentef und natürlich ganz besonders meiner Frau Liisa. Ohne ihre moralische Unterstützung wäre diese Arbeit nicht gelungen.

Teilpublikationen

- M. Sentef, J. Kuneš, P. Werner, and A. P. Kampf, *Correlations in a band insulator*, Phys. Rev. B **80**, 155116 (2009).
- A. P. Kampf, M. Kollar, J. Kuneš, M. Sentef, and D. Vollhardt, *Material-Specific Investigations of Correlated Electron Systems*, arXiv:0910.5126 (accepted for publication in “High Performance Computing in Science and Engineering, Garching 2009” (Springer)).

Lebenslauf

Michael Andreas Sentef

Hinter den Gärten 1
86157 Augsburg

Tel.: (+49) 821 44 91 57 49

Mobil: (+49) 173 66 44 751

Email: michael.sentef@physik.uni-augsburg.de

PERSÖNLICHE DATEN

Staatsangehörigkeit: Deutsch

Geburtsdatum: 25.09.1980

Geburtsort: Stuttgart

BERUF

seit 07/2006 Wissenschaftlicher Mitarbeiter,
Lehrstuhl Theoretische Physik III, Universität Augsburg.

10/2006 - 07/2010 Tutorien:
Theoretische Mechanik (WS 06/07),
Statistische Physik (SS 07),
Seminar zur Theoretischen Festkörperphysik (SS 07),
Quantenmechanik für Materialwissenschaften
und Lehramt (WS 09/10),
Elektrodynamik für das Lehramt (SS 10)

STUDIUM UND SCHULBILDUNG

10/2003 - 06/2006 Physik-Hauptstudium (Diplom), Universität Augsburg,
Diplomarbeit: *Linear-Response Theory of Spin Transport*

10/2004 - 07/2006 Tutorien:
Math. Methoden für Physiker (WS 04/05),
Vorkurs Mathematik (WS 05/06),
Math. Methoden I für Materialwissenschaften (WS 05/06),
Math. Methoden II für Materialwissenschaften (SS 06)

10/2001 - 09/2003 Physik-Grundstudium (Vordiplom),
Mathematik-Grundstudium (Vordiplom),
Universität Augsburg

08/2000 - 06/2001 Zivildienst, Sozialstation Wendlingen

09/1991 - 07/2000 Robert-Bosch-Gymnasium Wendlingen

08/1987 - 07/1991 Grundschule, Gartenschule Wendlingen

Stipendien: Promotionsstipendiat der Studienstiftung des deutschen Volkes
Promotionsstipendiat nach dem Bayerischen Eliteförderungsgesetz
Studienstipendiat der Studienstiftung des deutschen Volkes

Augsburg, 26. Juli 2010

Michael Andreas Sentef